Observation of extremely strong neutron scattering

B. R. Meshcherov, A. I. Fomin, and S. M. Chernyavskiĭ
Kurchatov Institute Russian Science Center, 123182 Moscow, Russia

P. Geltenbort
Institut Laue-Langevin, 38042 Grenoble, France

R. I. Zakharchenya
A. F. Ioffe Physicotechnical Institute, Russian Academy of Sciences, 194223 St. Petersburg, Russia

(Submitted 27 January 1998)
Pis'ma Zh. Éksp. Teor. Fiz. **67**, No. 5, 291–295 (10 March 1998)

The spectral dependence of the transmission of a collimated neutron beam by disordered quartz microstructures is measured. The observed mean free paths are very short, down to 200 nm. The results show that scattering with a characteristic value of the parameter $kl \leqslant 10$ is realized near the neutron total external reflection edge. © *1998 American Institute of Physics.* [S0021-3640(98)00105-4]

PACS numbers: 61.12.Ex, 61.43.Er

Despite the fact that the phenomenon of strong (Anderson) localization[1] is of a very general character, i.e., it can be observed in the propagation of both waves and particles of any nature in randomly nonuniform media, many investigations performed in this field initially focused on the problem of electron transport. Nonetheless, interest in studying other systems is continually increasing, first and foremost, because of the possibility of making more direct observations and interpretation of the effects which appear. For example, the diffusion of electromagnetic radiation in disordered structures has been studied intensively during the last ten years.[2–6] As a result, near-localization has been observed in a number of recent experiments with microwaves and visible light,[4–6] but the localized state itself has not been realized. Therefore the search for and study of new systems remains very topical. Specifically, in Ref. 7 a proposal was made to investigate the possibility of localization of ultracold neutrons (UCNs). This experiment, the preliminary results of which are reported in Ref. 8, is from our standpoint a quite convincing demonstration of the realizability of conditions for strong neutron scattering, and it also points to further steps for approaching the mobility threshold of UCNs, if such a threshold exists.

The scattering power of a medium is most often described by the mean free path l and the parameter kl, where k is the neutron wave number. Since the coherent part of the intensity decreases (see, for example, Refs. 3 and 9) as $\exp(-L/l)$ after passage through a layer thickness L consisting of randomly distributed nonabsorbing scatterers, the most direct method of determining the mean free path is to measure the transmission of a collimated beam. According to the estimates presented in Ref. 7, intense neutron scatter-

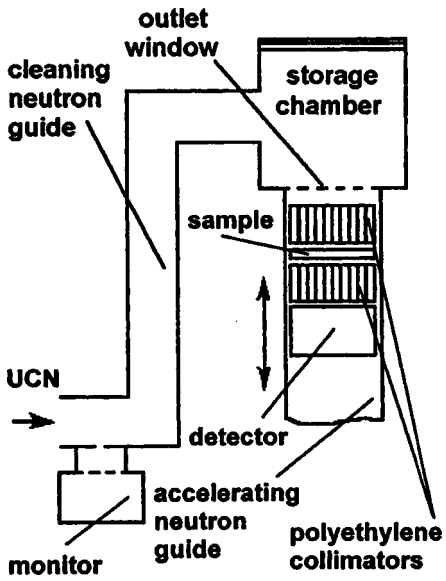

FIG. 1. Diagram of the experimental apparatus.

ing should arise near the threshold of total reflection for the scatterer material. In this energy range the wave number dependence of the material constants becomes very strong,[10] so that monochromatization of a UCN flux is a necessary condition for performing the measurements. Finally, the average size d of the scatterers must be selected taking into account the scale of wavelengths λ in the energy range of interest.[3,7] We investigated the spectral dependence of neutron transmission for samples with $kd/2 \sim 1$ and $d \sim \lambda_c$ (the total reflection edge). The PF2 extractor in the reactor at the Institut Laue-Langevin (Grenoble, France) was used as the UCN source.

The experimental arrangement is displayed in Fig. 1. The UCN flux passes through a stainless steel cleaning neutron guide, which makes two 90° turns and rises by 120 cm. The transmitted neutrons accumulate in a stainless steel chamber with an aluminum exit window, mounted at the bottom of the chamber, and an aluminum foil placed at the top. Thus, a relatively narrow band is cut out of the initially quite wide UCN energy distribution. Specifically, the energy spectrum immediately after the exit window varies from 55 to 70 neV. An accelerating neutron guide with a standard ^{3}He proportional counter, which can move inside guide, is used for measuring the spectral dependences. The sample is placed between two polyethylene collimators, secured on the detector in front of its entrance window. Another proportional counter serves for monitoring the UCN flux inside the cleaning neutron guide. The neutron energy E was scanned from 70 to 300 neV with this gravitational spectrometer.

All samples were fabricated by the sol-gel method.[11,12] Quartz particles with average diameter $d \simeq 30$ nm were formed in the process of hydrolysis of silicon alkoxide in the presence of the main catalyst (ammonia).[13,14] To clean the reaction products, the products were heat-treated for 10 h at 450 C, making it possible to remove organic compounds. To prevent SiO_2 particles from sticking together, which is undesirable, the quartz powder

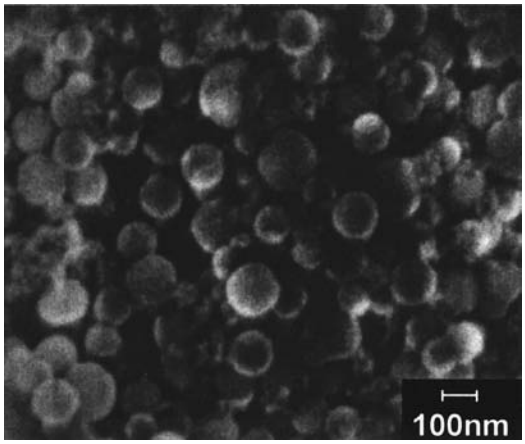

FIG. 2. SEM image of the surface of one of the samples.

was dissolved with distilled water and subjected to ultrasound treatment. Small quantities of the mixture obtained were then placed onto a rapidly rotating substrate. A nonuniform layer of the required thickness was formed by alternating the process of depositing the suspension with drying and sintering. The substrates consisted of standard 100 mm in diameter and 0.5 mm thick single-crystal silicon wafers polished on both sides. The average size of the scatterers comprising the layers prepared was determined by the conditions of the final annealing. It was established that heat treatment at 700 °C does not affect the SiO_2 particles, while raising the temperature to 900 °C changes their shape and size, leading to the formation of almost perfect microspheres with diameter $d \simeq 100$ nm. Thus, two types of samples, differing from one another by the sizes of the scatterers, $d \simeq 30$ nm and $d \simeq 100$ nm, respectively, were prepared. An SEM image of the surface of one of the experimental microstructures is presented in Fig. 2. The volume fraction f of the particles was equal to 0.4–0.5 for samples of the first type and 0.5–0.6 for samples of the second type.

To prevent the substrate from affecting the results the measurements of the transmission of UCNs by a silicon crystal without a SiO_2 layer were performed. The background count rate was virtually time-independent on account of the stable operation of the reactor. To obtain additional experimental confirmation of the fact that scattering has occurred, the transmitted neutron flux was measured with and without a collimator installed between the sample and the detector, and the values obtained were compared with one another. Typical spectral dependences of the transmission $T_c(E)$ for a collimated beam are presented in presented in Fig. 3. At the completion of the experiment the structure of the disordered layers was carefully studied (and thickness measurements were also performed) with an Alpha-step microprofilometer, manufactured by the Tencor Instruments Company, and a JEM-100 electron microscope, manufactured by JEOL. This gave values of the mean free path $l = -L/\ln(T_c)$ and the parameter $kl = (2mE)^{1/2} l/\hbar$, where m is the neutron mass. It was found that $L \leqslant l$ for all available samples in the entire energy range. This means that there is not enough time for a diffusion flux to form and therefore the thickness dependence $T(L)$ does not play such a serious role as for

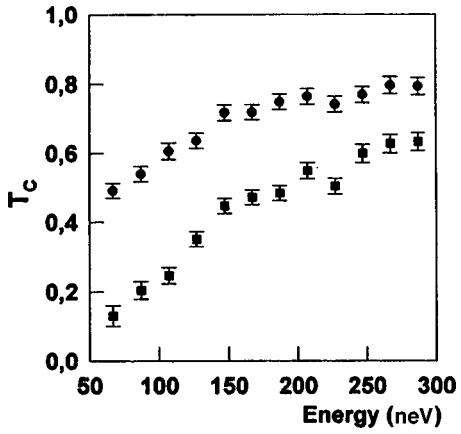

FIG. 3. Transmission of a collimated beam as a function of neutron energy: (□) $d=100$ nm, $L=300$ nm; (●) $d=100$ nm, $L=150$ nm.

larger values of L, for which the variation of the $T(L)$ shows nearness to a localized state.[3–6]

The spectral dependence of l for both types of samples is shown in Fig. 4. In agreement with our expectations, the mean free path decreases rapidly with decreasing neutron energy. The lowest attainable value of l equals 150–200 nm for $d \simeq 100$ nm. Comparing with other experiments, it should be noted that the UCN scattering observed in the present work is extremely strong. Its macroscopic section (l^{-1}), for example, is two to three orders of magnitude greater than the data presented in Refs. 15 and 16. Localization effects begin to affect strongly the character of the diffusion process when $kl \sim 1$, i.e., the value of the parameter kl is, in some sense, a measure of the closeness to the mobility threshold. Since the most intense scattering is observed near the total reflection edge for SiO_2 (approximately 90 neV), it can be conjectured that a random walk of UCNs inside a complicated structure formed by gaps between the quartz particles arises

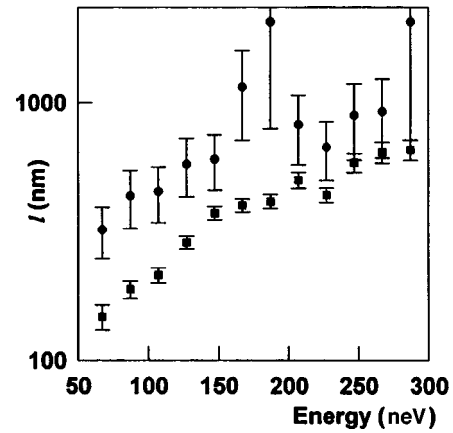

FIG. 4. Spectral dependence of the mean free path: (□) $d=100$ nm; (●) $d=30$ nm.

in this energy range. Using the value of the wave number for neutrons in vacuum, we obtain $\min(kl) \simeq 10$. However, the fact that the size of the scatterers $d \leqslant \lambda$ can appreciably influence the character of the neutron transport. If the value of k for an effective medium (whose density equals the average density of the nonuniform layer) is used, then for $f = 0.5$ we have $\min(kl) \simeq 6$, i.e., of the same order of magnitude. In any case, the value of the parameter kl is too far from the value required to satisfy the standard localization criterion $kl = 1$. Nonetheless, thicker SiO_2 layers with the same structure can apparently be successfully used to investigate weak localization of neutrons.

The results obtained demonstrate a strong dependence of the mean free path on both the neutron energy and the size of the scatterers. It now appears that the most interesting region from the standpoint of new experiments lies between the total reflection edges of the scatterer material and the effective medium. We believe that using materials with a higher potential barrier as well as optimizing the sizes of the nonuniformities will make it possible to approach very close to the mobility edge and, possibly, even obtain a localized state of UCNs.

We are grateful to S. T. Belyaev, L. N. Bondarenko, I. K. Meshkovskiĭ, and V. I. Morozov for helpful discussions and their interest in our investigations. This work was made possible in part by the support of the Russian Fund for Fundamental Research under contract 95-02-05031-a (B. R. M. and S. M. Ch.), Grant N9A000 from the International Science Fund (B. R. M.), and Grant N9A300 from the MNF and the Russian Government (B. R. M.).

[1] P. W. Anderson, Phys. Rev. **109**, 1492 (1958).
[2] S. John, Phys. Rev. Lett. **53**, 2169 (1984).
[3] P. W. Anderson, Philos. Mag. B **52**, 505 (1985).
[4] A. Z. Genack, Phys. Rev. Lett. **58**, 2043 (1987).
[5] J. M. Drake and A. Z. Genack, Phys. Rev. Lett. **63**, 259 (1989).
[6] N. Garcia and A. Z. Genack, Phys. Rev. Lett. **66**, 1850 (1991).
[7] B. R. Meshcherov, Fiz. Tverd. Tela (St. Petersburg) **38**, 1081 (1996) [Phys. Solid State **38**, 598 (1996)].
[8] P. Geltenbort, S. Chernyavsky, A. Fomin *et al.*, ILL Experimental Report 3-14-35, Grenoble, 1996.
[9] A. Ishimaru, *Wave Propagation and Scattering in Random Media*, Academic Press, New York, 1978.
[10] V. F. Sears, Phys. Rep. **82**, 1 (1982).
[11] R. K. Iler, *The Chemistry of Silica*, Wiley, New York, 1955.
[12] L. L. Hench and J. K. West, Chem. Rev. **90**, 33 (1990).
[13] W. Stober, A. Fink, and E. Bohn, J. Colloid Interface Sci. **26**, 62 (1968).
[14] C. M. Bagnall, L. G. Howarth, and P. F. James, J. Non-Cryst. Solids **121**, 56 (1990).
[15] M. Lengsfeld and A. Steyerl, Z. Phys. B **27**, 117 (1977).
[16] A. V. Antonov, A. I. Isakov, S. P. Kuznetsov *et al.*, Fiz. Tverd. Tela (Leningrad) **26**, 1585 (1984) [Sov. Phys. Solid State **24**, 963 (1984)].

Translated by M. E. Alferieff

Possible approach to the halo size determination from fragmentation reactions

G. D. Alkhazov[a)]

St. Petersburg Nuclear Physics Institute, Russian Academy of Sciences, 188350 Gatchina, Leningrad Region, Russia

(Submitted 4 February 1998)
Pis'ma Zh. Éksp. Teor. Fiz. **67**, No. 5, 296–301 (10 March 1998)

It is shown that the distribution of the sum of the observed transverse momenta **q** of the core fragment and of the halo nucleons in the case of ''elastic'' breakup of exotic halo nuclei should have a dip at $\mathbf{q}=0$, the width of which may be a measure of the halo size. © *1998 American Institute of Physics.* [S0021-3640(98)00205-9]

PACS numbers: 21.10.Gv, 25.70.Mn

Exotic neutron- or proton-halo nuclei, discovered recently,[1,2] are new and interesting nuclear objects which are studied extensively nowadays. One of the main characteristics of these nuclei is the size of the halo, which may be several times larger than that of the nuclear core. Different methods have been used to determine the halo size, including measurement of the interaction cross sections,[3] low-energy and intermediate-energy elastic proton scattering,[4,5] pion double charge-exchange reactions,[6] measurement of fragment momentum distributions,[7,8] and some others. Nevertheless, the results obtained are subject to various sources of uncertainty and give somewhat different results. In our opinion, the overall nuclear size may be determined most accurately by the method of intermediate-energy proton elastic scattering.[5] As to determination of the sizes of the halo and of the core by this method, the results obtained depend on the nuclear model used.

Investigations of the structure of exotic nuclei have been carried out in recent years mostly by the method of nuclear fragmentation. The fragmentation of exotic nuclei, which are loosely bound nuclear systems, occurs mainly as ''elastic'' breakup[9] or as a ''stripping'' reaction.[10] The observed momentum distributions of the fragments to some extent reflect the internal nucleon distributions of the nuclei under study. In principle, the widths of these distributions contain information on the halo size. For example, in the fragmentation of ^{11}Li nuclei at 800 MeV/u (Ref. 7) there were two components observed in the transverse momentum distribution of the ^{9}Li fragments. It was supposed that the broad component of this distribution is due to a neutron knock-out from the ^{11}Li core, while the narrow component is due to a knock-out of neutrons from the ^{11}Li halo. The narrow width of the latter component corresponds to a relatively large size of the ^{11}Li halo. Later, a very narrow width in the angular distribution of neutrons from fragmentation of ^{11}Li nuclei at 29 MeV/u was observed.[8] A very big ^{11}Li halo radius (of about 12 fm) was inferred from this experiment. Subsequently it became clear[11] that the narrow component in the neutron angular distribution appears due to decay of the ^{10}Li nucleus

formed after the knock-out of one of the halo neutrons from ^{11}Li, and that the width of this distribution is linked not with the internal neutron halo momentum distribution but with the energy of the intermediate excited state of this decaying ^{10}Li nucleus. The observed fragment momentum distributions may also be distorted significantly by the interaction of the target with the nuclear constituents and by the final-state interaction of the knocked-out nucleon (or fragment) with the rest of the system. For this reason, the information on the halo sizes obtained from the previously performed fragmentation experiments is qualitative rather than quantitative.

In our previous paper[12] we proposed an experiment that would yield accurate information on the neutron halo momentum distribution. The momentum distribution of halo neutrons measured in such an experiment is expected to suffer less distortion from the reaction mechanism than in the previous experiments. Then the width of this distribution could be used for evaluation of the halo size.

Here we discuss another approach for determination of the halo size based on measurement of transverse momentum distributions of fragments arising in the ''elastic'' nuclear breakup of a beam of exotic nuclei interacting with a fragmentation target. The method we propose[13] is essentially different from that which has ordinarily been used in studies of exotic nuclei by fragmentation reactions.

In the following we shall consider the ''elastic'' breakup at intermediate energy, when one may use the Glauber theory for description of the scattering process. By ''elastic'' breakup we mean a process of fragmentation in which the target is left in the ground state, and new particles (primarily pions) are not produced. Note that at small momentum transfers to the target, the ''elastic'' breakup is the dominant mechanism of exotic nucleus fragmentation. We suppose that the exotic nucleus consists of a compact nuclear core, the internal structure of which is described by a wave function ψ_c, plus one or two halo nucleons, the relative motion of which around the core is described by a wave function $\varphi(\mathbf{r})$. We begin the analysis with the case of a one-nucleon halo nucleus. The wave function for such a nucleus may be written as:

$$\Psi_{f,i}=\varphi_{f,i}(\mathbf{r})\,\psi_c\,. \tag{1}$$

Here $\mathbf{r}=\mathbf{r}_n-\mathbf{r}_c$; $\mathbf{r}_n=(A_c/A)\mathbf{r}$ and $\mathbf{r}_c=-(1/A)\mathbf{r}$ are the halo nucleon and the core radius vectors in the nuclear center-of-mass (CM) system; $\mathbf{r}$ is their relative radius vector.

We describe the scattering of the target nucleus on the exotic nucleus as a process of consecutive independent interactions of the target nucleus with the subsystems of the exotic nucleus: its core and the halo nucleon. It is more convenient to do the analysis in the CM system of the halo nucleus. Then, in agreement with Refs. 9 and 14, we can write the following formula for the amplitude of elastic breakup of the exotic nucleus to the core fragment and the halo nucleon:

$$F_{fi}(\mathbf{q})=(ik/2\pi)\int \exp(i\mathbf{q}\cdot\mathbf{b})\langle\varphi_f|\Gamma(\mathbf{b})|\varphi_i\rangle d^2b, \tag{2}$$

$$\Gamma(\mathbf{b})=\Gamma_{tn}(\mathbf{b}-\mathbf{s}_n)+\Gamma_{tc}(\mathbf{b}-\mathbf{s}_c)-\Gamma_{tn}(\mathbf{b}-\mathbf{s}_n)\Gamma_{tc}(\mathbf{b}-\mathbf{s}_c). \tag{3}$$

Here $\mathbf{q}$ is the momentum transfer from the target to the halo nucleus (we consider relatively small momentum transfers, when $\mathbf{q}$ is practically perpendicular to the direction of the beam), k is the magnitude of the wave vector $\mathbf{k}$ of the projectile, $\mathbf{b}$ is the impact

vector ($\mathbf{b}\perp\mathbf{k}$), the brackets $\langle|\ |\rangle$ mean integration over the radius vector $\mathbf{r}$, the vectors $\mathbf{s}_n$ and $\mathbf{s}_c$ are the transverse coordinates of the halo neutron and of the core, $\Gamma(\mathbf{b})$ is the profile function for interaction between the target and the exotic nucleus (for fixed relative positions of the halo nucleon and the core), and $\Gamma_{tn}(\mathbf{b}-\mathbf{s}_n)$ and $\Gamma_{tc}(\mathbf{b}-\mathbf{s}_c)$ are the profile functions for the interaction of the target with the halo nucleon and with the core. These profile functions are connected with the corresponding amplitudes for the elastic scattering of the target on the halo nucleon and on the core by the following relations:

$$\Gamma_{tn}(\mathbf{b})=(1/2\pi ik)\int \exp(-i\mathbf{q}\cdot\mathbf{b})f_{tn}(\mathbf{q})d^2q, \tag{4}$$

$$\Gamma_{tc}(\mathbf{b})=(1/2\pi ik)\int \exp(-i\mathbf{q}\cdot\mathbf{b})f_{tc}(\mathbf{q})d^2q. \tag{5}$$

The amplitudes $f_{tn}(\mathbf{q})$ and $f_{tc}(\mathbf{q})$ may be calculated by the standard way using the Glauber multiple scattering theory, the ground state density distributions of the target and of the core fragment, and the free-scattering nucleon–nucleon amplitudes. The formula for $F_{fi}(\mathbf{q})$ may be rewritten as

$$F_{fi}(\mathbf{q})=F_{tn}(\mathbf{q})+F_{tc}(\mathbf{q})+F_{tnc}(\mathbf{q}), \tag{6}$$

$$F_{tn}(\mathbf{q})=f_{tn}(\mathbf{q})S_{fi}((A_c/A)\mathbf{q}), \tag{7}$$

$$F_{tc}(\mathbf{q})=f_{tc}(\mathbf{q})S_{fi}((-1/A)\mathbf{q}), \tag{8}$$

$$F_{tnc}(\mathbf{q})=-(2\pi ik)^{-1}\int S_{fi}(\mathbf{q}')f_{tn}(\mathbf{q}/A+\mathbf{q}')f_{tc}((A_c/A)\mathbf{q}-\mathbf{q}')d^2q', \tag{9}$$

where A and A_c are the mass numbers of the exotic nucleus and of its core ($A=A_c+1$), and the inelastic form factor $S_{fi}(\mathbf{q})$ is defined by

$$S_{fi}(\mathbf{q})=\langle\varphi_f(\mathbf{r})|\exp(i\mathbf{q}\cdot\mathbf{r})|\varphi_i(\mathbf{r})\rangle=\int \varphi_f^*(\mathbf{r})\exp(i\mathbf{q}\cdot\mathbf{r})\varphi_i(\mathbf{r})d^3r. \tag{10}$$

The calculation of the cross section for elastic breakup becomes very simple if one neglects the final state interaction between the knocked-out nucleon and the core fragment, and uses plane waves for the wave functions $\varphi_f(\mathbf{r})$. Here we shall take into account only the amplitude $F_{tn}(\mathbf{q})$, which, as will be discussed later, gives the main contribution to the total amplitude $F_{fi}(\mathbf{q})$ (except at very small and very large values of $\mathbf{q}$). Then, integrating over the relative momentum between the knocked-out nucleon and the core fragment, for the differential cross section $d\sigma/d^2q$ one obtains:

$$d\sigma/d^2q=k^{-2}|f_{tn}(\mathbf{q})|^2. \tag{11}$$

It is seen that in the approximation used the differential cross section $d\sigma/d^2q$ does not depend on the halo nucleus structure, and that at $\mathbf{q}=0$ it has the maximum value. However, as follows from a more accurate consideration, the dependence of $d\sigma/d^2q$ on $\mathbf{q}$ at small values of $\mathbf{q}$ is basically different from that given by Eq. (11), since $\varphi_f(\mathbf{r})$ is not a plane wave. We do not know the exact behavior of the wave functions $\varphi_f(\mathbf{r})$. Nevertheless, by making use of completeness of the system of the wave functions $\varphi_f(\mathbf{r})$, it is easy to obtain the differential cross section summed up over all final states. Supposing that the halo nucleus has no bound excited states, we obtain:

$$d\sigma/d^2q = k^{-2}\sum_{f\neq i} |F_{fi}(\mathbf{q})|^2 = k^{-2}|f_{tn}(\mathbf{q})|^2[1-(S_n(\mathbf{q}))^2] \tag{12}$$

with $S_n(\mathbf{q}) = S((A_c/A)\mathbf{q})$, where $S_n(\mathbf{q})$ is the halo-nucleon form factor, and $S(\mathbf{q})$ is the form factor corresponding to the wave function $\varphi_i(\mathbf{r})$:

$$S(\mathbf{q}) = \int \exp(i\mathbf{q}\cdot\mathbf{r})|\varphi_i(\mathbf{r})|^2 d^3r. \tag{13}$$

It is seen that the cross section $d\sigma/d^2q$, following from amplitude (7), does not depend on the details of the final-state interaction between the knocked-out nucleon and the core fragment, but depends only on the amplitude $f_{tn}(\mathbf{q})$, which may be calculated rather accurately, and on the form factor $S_n(\mathbf{q})$, characterizing the halo-nucleon spatial distribution under study. Note that $S_n(\mathbf{q}) = 1$ at $\mathbf{q} = 0$, and $|S_n(\mathbf{q})| \ll 1$ at $q \gg R_h^{-1}$. At small values of q

$$S_n(\mathbf{q}) \approx (1 - q^2R_h^2/6), \tag{14}$$

where $R_h = \langle \mathbf{r}^2 \rangle_h^{1/2}$ is the root-mean-square radius of the halo space distribution. Therefore, at small values of $\mathbf{q}$, according to (12) $d\sigma/d^2q$ is proportional to q^2 : $d\sigma/d^2q \sim q^2$ (for $qR_h \ll 1$). At $q = 0$, as a consequence of orthogonality of the wave functions $\varphi_f(\mathbf{r})$ to the ground-state wave function $\varphi_i(\mathbf{r})$, one has $d\sigma/d^2q = 0$. Though obtained here for a wave function of the type (1), this result holds true for any wave functions provided that only a single-nucleon scattering term is considered. Thus the distribution over the transverse momentum $\mathbf{q}$ should have a dip at $\mathbf{q} = 0$, with a width proportional to R_h^{-1}. By analyzing the shape of this distribution, one can determine the value of R_h.

Now let us consider the other terms in Eq. (6). If we take into account only term (8), then a similar anaysis yields

$$d\sigma/d^2q = k^{-2}|f_{tc}(\mathbf{q})|^2[1-(S_n(\mathbf{q}/A_c))^2]. \tag{15}$$

(Note that $S_c(\mathbf{q}) = S(-\mathbf{q}/A) = S_n(\mathbf{q}/A_c)$; for simplicity we limit consideration to an s-state spherical wave function $\varphi_i(\mathbf{r})$.) Thus, here again $d\sigma/d^2q = 0$ at $q = 0$. At the same time, the shape of this distribution is different from that given by Eq. (12), the sensitivity of the shape to the halo size at small values of $\mathbf{q}$ being relatively low. The magnitude of the amplitude $f_{tc}(\mathbf{q})$ at small values of $\mathbf{q}$ exceeds that of the amplitude $f_{tn}(\mathbf{q})$, however the contribution to the fragmentation cross section of the scattering of the target on the core is suppressed by the factor $[1-(S_n(\mathbf{q}/A_c))^2]$. For this reason, the contribution of this term to the total cross section for fragmentation is relatively small. The contribution to the cross section of term (9) is also small. Note that this term is not zero at $q = 0$. Of course, all the three terms contribute to the cross section coherently, so that the amplitudes should be added up, and then the cross section corresponding to the total amplitude can be calculated.

An important channel of fragmentation of exotic nuclei at small momentum transfers for targets with high charge number Z is the Coulomb dissociation. To a first approximation the contribution from the Coulomb dissociation may be taken into account by adding to amplitude (6) the relevant Coulomb term:

$$F_{\text{Coul}}(\mathbf{q}) = f_{\text{Coul}}(\mathbf{q})S_{fi}((-1/A)\mathbf{q}), \tag{16}$$

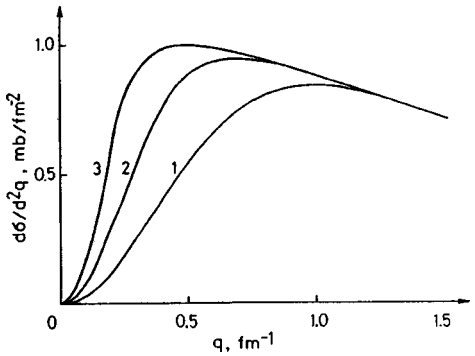

FIG. 1. The expected shape of the fragmentation cross section distribution over the transverse momentum **q**, calculated from Eq. (12) for three values of the halo radius: 3 fm, 5 fm, and 8 fm (curves *1*, *2*, and *3*, respectively).

where $f_{\mathrm{Coul}}(\mathbf{q})$ is the Coulomb amplitude for the scattering of the target on the core. The contribution from the Coulomb dissociation is substantial at very small momentum transfers, and when added to the strong-interaction fragmentation, it may result in filling of the q-distribution dip discussed above. Thus it is evident that to use the proposed method for determination of the halo size, one has to work with low-Z targets.

The analysis of the data is especially simple and much less ambiguous if hydrogen is taken as a target. The shape of $d\sigma/d^2q$ calculated in this case using only amplitude (7) at an energy of around 800 MeV/u for three halo density distributions parametrized by a Gaussian function with root-mean-square radii of 3 fm, 5 fm, and 8 fm, is demonstrated in Fig. 1. It is seen that the size of the halo may be determined easily from the shape of this distribution. The contribution of amplitudes (8) and (9) to the cross section, as we have said, should be small. On account of the contribution of amplitude (9), the minimum in $d\sigma/d^2q$ at $q=0$ will be partially filled. However, the general character of the dependence of $d\sigma/d^2q$ over **q**, with a dip at $q=0$, will remain the same, so that the width of this dip may be used for determination of the halo size. The method discussed may be applied to determine the sizes of neutron as well as proton halos. A similar picture is expected to hold for the distribution of the fragmentation cross section over the transverse momentum **q** in the case of two-neutron halo nuclei as well. In that case the value of the momentum **q** may be determined experimentally from the sum of the transverse momenta of the detected core fragment and halo neutrons.

The method of the halo size determination discussed here is similar in a certain sense to the method of small-angle elastic scattering of intermediate energy protons, which we proposed and used before.[15,5] In both cases the information about the halo size is obtained from scattering with small momentum transfers, and in both cases the shape of the halo form factor is studied. However, in the case of proton elastic scattering there are significant contributions to the cross section at small scattering angles (at small momentum transfers) both from the halo nucleons and from the core, so that a problem of separation of these contributions arises. As to the nuclear fragmentation, the shape of the **q** distribution at small values of q is determined mainly by the **q** dependence of the halo form factor, the contribution from the core scattering being suppressed, as was discussed before. We note also that for disentangling the contributions of scattering from the halo

and from the core in the case of nuclear fragmentation, a correlation between the momentum transfer **q** and the measured fragment momenta could be helpful.

In conclusion, we have shown that the distribution of the sum of the transverse momenta of the fragments should exhibit a dip. The width of this dip depends on the halo size. It would be interesting to check this theoretical prediction experimentally. Note that a minimum at $q=0$ has also been predicted for incoherent scattering from stable nuclei;[16] however, no investigations were carried out that could confirm the existence of this minimum. Provided that this minimum exists, the method discussed above may be used for measuring the sizes of halos in exotic nuclei. In any case, measurement of the distribution of the sum of the observed transverse momenta **q** of the core fragment and of the halo nucleons at small values of q is important for understanding of the mechanism of fragmentation of exotic nuclei.

[a)]e-mail: alk@hep486.pnpi.spb.ru

[1] I. Tanihata, H. Hamagaki, O. Hashimoto *et al.*, Phys. Lett. B **160**, 380 (1985).
[2] I. Tanihata, H. Hamagaki, O. Hashimoto *et al.*, Phys. Rev. Lett. **55**, 2676 (1985).
[3] I. Tanihata, D. Hirata, T. Kobayashi *et al.*, Phys. Lett. B **289**, 261 (1992).
[4] C.-B. Moon, M. Fujimaki, S. Hirenzaki *et al.*, Phys. Lett. B **297**, 39 (1992).
[5] G. D. Alkhazov, M. H. Andronenko, A. V. Dobrovolsky *et al.*, Phys. Rev. Lett. **78**, 2313 (1997).
[6] W. R. Gibbs and A. C. Hayes, Phys. Rev. Lett. **67**, 1395 (1991).
[7] T. Kobayashi, O. Yamakawa, K. Omata *et al.*, Phys. Rev. Lett. **60**, 2599 (1988).
[8] R. Anne, S. E. Arnell, R. Bimbot *et al.*, Phys. Lett. B **250**, 19 (1990).
[9] A. I. Akhiezer and A. G. Sitenko, Phys. Rev. **106**, 1236 (1957).
[10] R. Serber, Phys. Rev. **72**, 1008 (1947).
[11] F. Baranko, E. Vigezzi and R. A. Broglia, Phys. Lett. B **319**, 387 (1993).
[12] G. D. Alkhazov, JETP Lett. **66**, 82 (1997).
[13] G. D. Alkhazov, Preprint PNPI-**2170** NP-27-1997, Gatchina 1997.
[14] A. G. Sitenko, A. D. Polozov, M. V. Evlanov *et al.*, Nucl. Phys. A **442**, 122 (1985).
[15] G. D. Alkhazov and A. A. Lobodenko, JETP Lett. **55**, 379 (1992).
[16] R. Glauber and Matthia, Nucl. Phys. B **21**, 135 (1970).

Published in English in the original Russian journal. Edited by Steve Torstveit.

Measurement of the rate of nuclear capture of negative muons in the isotopes ^{84}Kr and ^{136}Xe

T. N. Mamedov,[a)] V. G. Grebinnik, V. A. Zhukov, V. A. Kuz'min, and A. V. Stoĭkov
Joint Institute of Nuclear Research, 141980 Dubna, Moscow Region, Russia

S. G. Barsov, A. L. Getalov, V. P. Koptev, and G. V. Shcherbakov
St. Petersburg Institute of Nuclear Research, 118350 Gatchina, Leningrad Region, Russia

T. V. Tetereva
Scientific-Research Institute of Nuclear Physics, Moscow State University, 119899 Moscow, Russia

R. A. Éramzhyan
Institute of Nuclear Studies, Russian Academy of Sciences, 117312 Moscow, Russia

(Submitted 28 January 1998)
Pis'ma Zh. Éksp. Teor. Fiz. **67**, No. 5, 302–307 (10 March 1998)

The lifetime of a negative muon in the 1*S* state in the isotopes ^{84}Kr and ^{136}Xe was measured. The values obtained, $\tau(^{84}\mathrm{Kr})=139.2\pm2.9$ ns and $\tau(^{136}\mathrm{Xe})=111.0\pm4.6$ ns, correspond to total nuclear capture rates $\Lambda_c(^{84}\mathrm{Kr})=6.75\pm0.15$ $\mu\mathrm{s}^{-1}$ and $\Lambda_c(^{136}\mathrm{Xe})=8.6\pm0.4$ $\mu\mathrm{s}^{-1}$. Theoretical calculations of the rate of nuclear capture of a negative muon are performed for the Kr isotopes. The experimental results are compared with the theoretical calculations. © *1998 American Institute of Physics.* [S0021-3640(98)00305-3]

PACS numbers: 25.30.Mr, 27.50.+e, 27.60.+j

The study of the capture of negative muons by atomic nuclei yields information about the nature of the weak interaction. An important characteristic of this process is the rate of nuclear capture of muons. The total rate of nuclear capture of muons has now been measured for the overwhelming majority of the elements.[1,2] The theoretical calculations of the nuclear capture rate are based on Primakoff's classic work.[3] The main difficulty in the theoretical calculations is that all possible excited states of the final nucleus in the reaction

$$\mu^- + (Z,A) \rightarrow (Z-1,A)^* + \nu_\mu$$

must be taken into account.

Numerical calculations of the rate of nuclear capture of negative muons in different models of the nucleus have been performed thus far for a limited number of elements, mainly light and medium elements (see, for example, Refs. 1 and 4–7). Satisfactory agreement with experimental data was obtained in a number of cases. The semiempirical

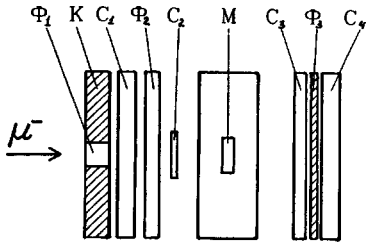

FIG. 1. Experimental arrangement: M — target, Φ_1, Φ_2, Φ_3 — moderators (Φ_1 — polyethylene, Φ_2 — Plexiglas, Φ_3 — brass); K — collimator (brass); C_1, C_2, C_3, C_4 — scintillation counters.

Goulard–Primakoff formula[8] for the rate of capture of a negative muon by a nucleus with mass number A and charge Z is also used to describe the experimental data.

There are still no experimental data on the rate of nuclear capture of negative muons in the isotopes of krypton and xenon. These elements are of special interest because they lie near the extrema of the Goulard–Primakoff theoretical curve. Moreover, krypton and xenon possess six and nine stable isotopes, respectively, making it possible to investigate the isotopic dependence of the rate of nuclear capture of negative muons. Characteristic features in the values of the capture rate can also be expected for isotopes with nonzero nuclear spin (^{83}Kr, ^{129}Xe, ^{131}Xe).

The rate of nuclear capture of negative muons in a natural mixture of Xe isotopes was first measured in Ref. 9. Its value fell in the range of values given by the Goulard–Primakoff formula for the limiting stable Xe isotopes.

In the present letter we report the results of measurements of the rate of capture of negative muons in the isotopes ^{84}Kr and ^{136}Xe.

The experiment was performed with the MYUONIĬ μSR spectrometer[10] using a separated beam of negative muons from the synchrocyclotron at the St. Petersburg Institute of Nuclear Physics (Gatchina) and consisted of measuring the total rate of vanishing of muons from the 1S state of the isotope of interest by detecting the electrons from $\mu^- \rightarrow e^-$ decay.

Figure 1 shows the experimental arrangement. A beam of negative muons with a momentum of 90 MeV/c,[11] slowed down beforehand in the moderators Φ_1 and Φ_2, was stopped in the target M, consisting of a container filled with condensed gas. The momentum spread in the beam was $\delta P/P \approx 10\%$.[11] The beam was collimated by a collimator K with an opening 25 mm in diameter. The background due to the beam electrons was discriminated by setting the thresholds for triggering the signal shapers of the counters C_1 and C_2. The separated muon beam also contained a very small admixture of π^- mesons. However, the π^- mesons were completely absorbed in the materials located in their path up to the counter C_2. Indeed, the quantity of hydrocarbon-containing matter in the beam path in the moderators Φ_1 and Φ_2 and the counter C_1 was $\sim$4.3 g/cm^2. For a momentum of 90 MeV/c the ranges of the muon and π^- meson in this material will equal 5.1 g/cm^2 and 2.9 g/cm^2, respectively.

The signal $C_1C_2\overline{C_3}$ (''start'') from the scintillation counters corresponded to stopping of a muon in the target, while the signal $\overline{C_1}C_3C_4$ (''stop'') determined the moment

a decay electron exited from the target. To eliminate distortions of the spectrum the events in which in a time of 10 μs after the muon stops a second muon or a second electron was recorded ($1\mu-1e$ condition) were discarded. A start signal was generated if before a muon stopped in the target the counter C_1 was not triggered in a time of 10 μs. The waiting time of an electron from $\mu^- \to e^-$ decay was equal to 10 μs. A time-to-digital converter[12] paired with a quartz IV 311 oscillator[13] were used to measure the time interval between the moment when a muon stops in the target and an electron from the decay of the muon is detected. The oscillator frequency was 200 MHz, the encoder had 2048 channels, and the channel width was 5 ns. Time intervals were also measured with a time-to-time converter followed by time-to-digital conversion; the channel width was equal to 1 ns. Codes of events from both encoders were recorded in fast memory, whose contents were then read along a CAMAC bus into a computer. The characteristic count rates were as follows: the coincidence of signals $C_1C_2 \sim 980\ s^{-1}$; the intensity of the start signals $\sim 400\ s^{-1}$; the number of events recorded in the spectrum $\sim 25\ s^{-1}$ (for an encoder with a channel width of 5 ns).

The temporal resolution of the apparatus was determined by detecting transit particles. The start signal was formed by the coincidence C_1C_2, while the stop signal was formed by the coincidence C_3C_4. The transit-particle peak, which corresponded to zero time, had in an encoder with a channel width of 1 ns a total width at half-height of 2.5 ns.

The low-temperature part of the apparatus, including a cryostat with the target and a cooling system, is described in Ref. 9. The entrance and exit windows of the vacuum jacket of the cryostat were closed with 0.15-mm-thick Mylar. The target chamber used in the present work, in contrast to the chamber described in Ref. 9, was made of 99.5% pure AD1 aluminum. The chamber consisted of a 12-mm-high cylinder with an inner diameter of 35 mm and with 2-mm-thick walls. The entrance and exit windows of the chamber were each 0.1 mm thick.

The ^{84}Kr and ^{136}Xe enrichments of the gases employed in the experiment were equal to 92.9% and 94%, respectively. The isotope ^{83}Kr (7%) was the main impurity in krypton, while the isotope ^{134}Xe (5.9%) was the main impurity in xenon. The impurity of other elements in both cases was less than 0.02%.

The measurements were performed in solid ^{84}Kr and ^{136}Xe at temperature 94.0 ± 0.5 K in the absence of an external magnetic field. Three pairs of Helmholtz coils compensated the stray magnetic field from the accelerator and the elements of the muon guide as well as the earth's magnetic field to 10^{-2} Oe.[10]

Figure 2 shows the spectrum of the temporal distribution of the $\mu^- \to e^-$-decay electrons in the case when the target chamber was filled with ^{84}Kr. The function

$$N(t) = N_1 e^{-t/\tau_1} + N_2 e^{-t/\tau_2} + N_3 e^{-t/\tau_3} + B$$

was fit to the experimental data. Here τ_i is the lifetime of a negative muon in the 1*S* state, the indices 1, 2, and 3 refer to ^{84}Kr (^{136}Xe), aluminum (used for the target chamber), and carbon (formed in the counters C_2 and C_3 and the windows in the vacuum jacket of the cryostat), respectively, and B is the background formed by random coincidences.

The data were analyzed by the least-squares method. The muon lifetimes in aluminum and carbon were determined according to the data from Ref. 2: $\tau(\mathrm{Al}) = 864.0$

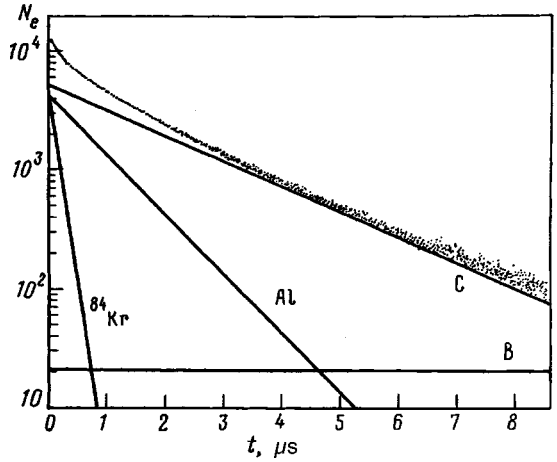

FIG. 2. Spectrum of the temporal distribution of $\mu^- \to e^-$-decay electrons. The target chamber is filled with solid ^{84}Kr. The straight lines show the contributions of the individual components to the spectrum.

± 2.0 ns and $\tau(\mathrm{C}) = 2026.3 \pm 1.5$ ns. (In a test experiment with an empty chamber we obtained for $\tau(\mathrm{Al})$ and $\tau(\mathrm{C})$ values which were equal, to within the error limits, to those presented above.)

The following values were obtained as a result of the analysis: $\tau(^{84}\mathrm{Kr}) = 139.2 \pm 2.9$ ns and $\tau(^{136}\mathrm{Xe}) = 111.0 \pm 4.6$ ns. The ratio of the contributions of the components $(N_1 : N_2 : N_3)$ was approximately the same in the case of ^{84}Kr and ^{136}Xe filled targets and was of the order of 1:1:1. The value of B obtained by fitting the spectra was equal to the constant background of random coincidences, determined as the average value over the histogram channels up to the physical zero of the converter, and equalled $\sim 0.15\%$ of the total contribution of the components $N_1 + N_2 + N_3$.

Since a muon from the 1S state either decays or is captured by a nucleus, the muon lifetime measured in a μSR experiment is determined by the sum of the rates of these processes $\tau^{-1} + \Lambda_d + \Lambda_c$, where Λ_d is the rate of decay of a bound muon and λ_c is the rate of its capture by a nucleus. The decay of a bound muon is somewhat suppressed compared with the decay of a free muon,[14] the suppression factor being equal to 0.95 for krypton and 0.91 for xenon.[14,2]

Taking for the lifetime of a free negative muon the value for the lifetime of μ^+, equal to 2197.03 ± 0.04 ns,[15] and taking account of the suppression factors presented above, we have for the rates of capture of negative muons by nuclei: $\Lambda_c(^{84}\mathrm{Kr}) = 6.75 \pm 0.15\ \mu\mathrm{s}^{-1}$ and $\Lambda_c(^{136}\mathrm{Xe}) = 8.6 \pm 0.4\ \mu\mathrm{s}^{-1}$.

Theoretical calculations of the nuclear capture rate were performed in the impulse approximation.[1] The wave functions, excitation energies, and nuclear matrix elements were obtained in the random-phase approximation. Separable residual nuclear interactions with effective constants, the systematics of whose values were obtained by comparing the computed and experimentally obtained strength functions of $\sigma t^{\pm}$ transitions for a wide group of nuclei from ^{54}Fe up to ^{208}Pb, were used here. The so-called rate terms were not taken into account when calculating the amplitude of nuclear capture. The

TABLE I.

Isotope	Capture rate, μs^{-1}	
	$g_P/g_A=8$	$g_P/g_A=6$
^{78}Kr	8.9	9.2
^{80}Kr	8.2	8.5
^{82}Kr	7.5	7.8
^{84}Kr	7.0	7.2
^{86}Kr	6.4	6.6

binding energies of a muon in a muonic atom, on whose values the computed capture rate strongly depends, were determined using the approximate Pustovalov formulas,[16] which take into account the finite size of the nucleus. The wave function of the muon inside a nucleus was assumed to be constant. The value of this constant was obtained by interpolating the values calculated in Ref. 17. A more detailed description of the theoretical model is given in Ref. 7.

Theoretical calculations of the rate of nuclear capture of negative muons were performed for Kr isotopes with zero nuclear spin for two different values of the ratio g_P/g_A of the pseudoscalar and axial-vector interaction constants (see Table I).

As one can see from the table, a strong isotopic dependence of the rate of nuclear capture is expected. It is also obvious that the total rate of nuclear capture of muons is insensitive to the ratio g_P/g_A: A variation of g_P/g_A by 25% changes the capture rate by only 3%.

In Fig. 3 the experimental data for ^{84}Kr and ^{136}Xe are compared with the calculations. The theoretical data for ^{84}Kr are presented for $g_P/g_A=8$. The same figures show

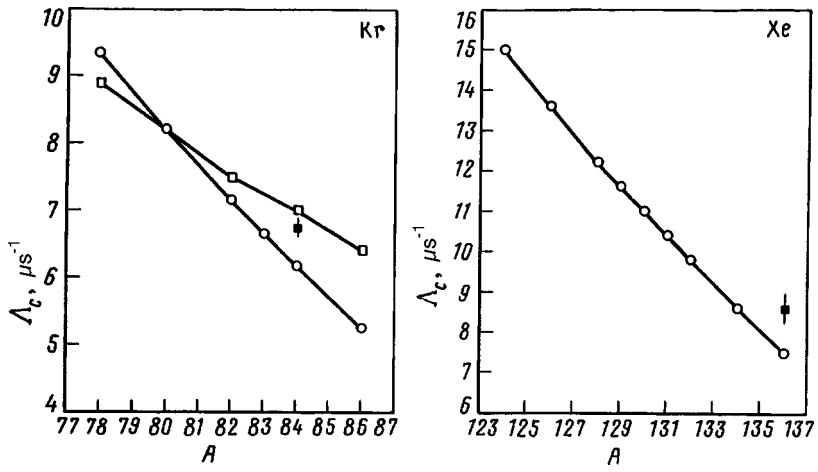

FIG. 3. Rate of nuclear capture of negative muons in Kr and Xe versus the mass number of the isotope: ○ — calculation using the Goulard–Primakoff formula; □, ■ — results of the present work (□ — calculation, ■ — experiment). The solid lines are drawn for clarity.

the computational results with the Goulard–Primakoff formula.[8] According to our calculations, the isotopic dependence of the rate of nuclear capture of muons is weaker than that obtained with the Goulard-Primakoff formula. In the case of ^{84}Kr the experimental value of Λ_c is closer to our calculations than to the calculations with the Golard–Primakoff formula, differing from the latter calculations by more than 3 standard deviations. The present measurement also completely confirms the presence of minima, as indicated in Ref. 2, in the dependence of the rate of nuclear capture of negative muons on Z near inert-gas atoms.

Measurements for other Kr and Xe isotopes and completion of the theoretical calculations for Xe will make it possible to perform a more detailed comparison of the theoretical and experimental results.

We are grateful to N. A. Rusakovich, V. B. Brudanin, and V. I. Komarov for their consideration of this work and for encouragement. We also thank I. L. Chaplygin for assisting in the preparation of the experiment.

This work was supported by the Russian Fund for Fundamental Research, Project 96-02-17582.

[a)]e-mail: tmamedov@nusun2.jinr.dubna.su

---

[1] V. V. Balashov, G. Ya. Korenman, and R. A. Éramzhyan, *Absorption of Mesons by Atomic Nuclei* [in Russian], Atomizdat, Moscow, 1978.
[2] T. Suzuki, D. F. Measday, and J. P. Roalsvig, Phys. Rev. C **35**, 2212 (1987).
[3] H. Primakoff, Rev. Mod. Phys. **31**, 802 (1959).
[4] N. C. Mukhopadhyay, Phys. Rep. C **30**, 1 (1977).
[5] G. G. Bunatyan, Yad. Fiz. **3**, 833 (1966) [Sov. J. Nucl. Phys. **3**, 613 (1966)].
[6] M. G. Urin and O. N. Vyazankin, Nucl. Phys. A **537**, 534 (1992).
[7] R. A. Eramzhyan, V. A. Kuz'min, and T. V. Tetereva, Preprint JINR, E4-96-478, Dubna, 1996.
[8] B. Goulard and H. Primakoff, Phys. Rev. C **10**, 2034 (1974).
[9] T. N. Mamedov, V. G. Grebinnik, K. I. Gritsaĭ *et al.*, JINR Reports, R15-96-498 [in Russian], Dubna, 1966.
[10] S. G. Barsov, A. L. Getalov, V. A. Gordeev *et al.*, Preprint No. 659 [in Russian], Leningrad Institute of Nuclear Physics, Leningrad, May 1981.
[11] V. A. Volchenkov, V. A. Gordeev, V. A. Eliseev *et al.*, Preprint No. 617 [in Russian], Leningrad Institute of Nuclear Physics, Leningrad, November 1980.
[12] *CAMAC. Time Code Converter 161.07* [in Russian], Leningrad Institute of Nuclear Physics, Leningrad, 1980.
[13] A. V. Selikov, JINR 13-81-844 [in Russian], Dubna, 1981.
[14] R. W. Huff, Ann. Phys. **16**, 288 (1961).
[15] Particle Data Group, ''Review of particle properties,'' Phys. Rev. D **50**, 1193 (1994).
[16] G. E. Pustovalov, Zh. Éksp. Teor. Fiz. **36**, 1806 (1959) [Sov. Phys. JETP **9**, 1288 (1959)].
[17] K. W. Ford and J. G. Wills, Nucl. Phys. **35**, 295 (1962).

Translated by M. E. Alferieff

Nonstatistical temperature fluctuations and displacement of equilibrium

V. I. Gervids[a)]
Moscow Engineering-Physics Institute (Technical University), 115409 Moscow, Russia

D. Kh. Morozov
Institute of Nuclear Fusion, Kurchatov Institute Russian Science Center, 123182 Moscow, Russia

(Submitted 21 January 1998)
Pis'ma Zh. Éksp. Teor. Fiz. **67**, No. 5, 308–312 (10 March 1998)

It is shown that an anomalously large displacement of equilibrium occurs in systems with rapidly oscillating temperature. The thermodynamic parameters of such a system differ substantially from the values corresponding to constant temperature. The dynamics of the distributions of hydrogen ions and impurity helium and carbon ions over ionization states in a hydrogen plasma and the dynamics of the intensity distribution of the line radiation of impurity carbon in a hydrogen plasma with oscillating temperature are calculated as an example. In systems with fluctuating temperature, the effect in question could be important in virtually all problems based on levelwise kinetics, for example, the energy balance and spectral diagnostics of turbulent plasma, the criterion of thermal stability, the dynamics of turbulent plasma and gas jets, the conditions for amplifier and oscillator operation in the active media of electric-discharge gas lasers, and so on.
 [S0021-3640(98)00405-8]

PACS numbers: 52.25.Kn, 52.25.Vy, 52.35.Ra

The peripheral tokamak plasma is, as a rule, strongly turbulent. The amplitude of the oscillations reaches several tens of percent. Under these conditions the electron temperature is also a rapidly oscillating function of time, which must affect the spectrum and the intensity of the radiation losses, the criteria of thermal stability, and number of other plasma characteristics. As is shown below, temperature fluctuations lead to a large change in the average values of a number of thermodynamic parameters — a displacement of equilibrium. Rough speaking, the qualitative explanation of the displacement of equilibrium effect under the conditions of temperature fluctuations consists of the following. Near equilibrium — both thermodynamic and, for example, coronal — the rates of threshold and nonthreshold processes balance. If the rates of the threshold processes are proportional to exponentials of the form $\langle \nu\sigma_{\rm thr}\rangle \propto \exp(-\Delta E/kT)$, where ΔE is the transition energy and T is the temperature, then the rates of nonthreshold processes can be described by relatively weak, most often power-law, functions of the temperature of the type $\langle \nu\sigma_{\rm nonthr}\rangle \propto T^{-\mu}$, $\mu \sim 1$. In most cases $\Delta E/kT \gg 1$, whence it is obvious that a rela-

tively small fluctuational increase in temperature leads to an order of magnitude increase in the rates of filling of the upper energy states, while their depopulation rate due to nonthreshold downward transitions remains virtually unchanged. As a result, the rate balance and, correspondingly, equilibrium appear with upper-state populations that are higher than under constant temperature conditions, as is observed in analytical and numerical calculations whose results are described below. The situation described is realized in its purest form in a coronal plasma with $T_e \leqslant 10^{-2}$ eV, for which the ratio $\Delta E_{\text{ion}}/kT \sim 5-10$, where ΔE_{ion} is the ionization energy of the most representative ion. It is assumed everywhere below that the particle velocity distribution is Maxwellian. This approach is used because of the fact that at the temperatures and densities characteristic for a peripheral plasma a Maxwellian distribution is established in a time 10^{-8}–10^{-7} s, which is at least two orders of magnitude shorter than the temperature oscillation times. The possible existence of non-Maxwellian particles in the system is not considered in the present letter.

We performed analytical calculations of the effect on the basis of a model of two (hydrogen) and also three (impurity helium) states by the methods of perturbation theory in the amplitude of the harmonic temperature oscillations of the form $T = T_0 + T_1 \times \sin \Omega t$, $T_1 \ll T_0$. The basic analytical results reduce to the following. The response of the populations of the states to temperature oscillations can be divided into two parts: constant and oscillatory. The oscillatory part of the response appears in an approximation linear in the amplitude of the oscillations, while the constant part, i. e. the displacement of equilibrium, is a particularly nonlinear effect. For a sufficiently small ratio of the period of the oscillations to the relaxation time of the system, the linear part of the response is proportional to this ratio and is small. The leading term in the displacement of equilibrium does not depend on this ratio and it does not vanish as the frequency of the oscillations approaches infinity. Thus, for sufficiently high frequencies the displacement of equilibrium is much larger than the amplitude of the population oscillations and becomes the main effect. The above-noted exponential temperature dependence of the rates of the threshold processes has the effect that the series expansion in terms of the amplitude of the oscillations becomes inapplicable even for very small amplitudes and the displacement of equilibrium is much larger than is predicted by perturbation theory.

Numerical calculations performed for carbon impurity on the basis of the nonstationary coronal model[1] simulate the experimentally observed spectrum of fluctuations in the peripheral plasma of the Macrotor tokamak[2]

$$T_e = T_0 \left(1 + a_0 \sum_k a_k \sin(2\pi \nu_k t + \varphi_k) \right).$$

Here each harmonic corresponds to a well-expressed peak in the experimental spectrum. Nine harmonics with frequencies from 5 to 90 kHz are included. The ratios of the amplitudes a_k were taken to be equal to the ratios of the heights of the experimental peaks; φ_k are random numbers uniformly distributed from $-\pi$ to π. As is well known, the level of fluctuations in the peripheral plasma of a tokamak can reach 20–80%, so that a_0 was set equal to 0.2, which corresponds to $\sqrt{\langle (\Delta T)^2 \rangle} = 0.3$.

The ionization and photorecombination rates were taken from Refs. 3 and 4, respectively. The total line radiation losses, normalized to the electron and impurity densities,

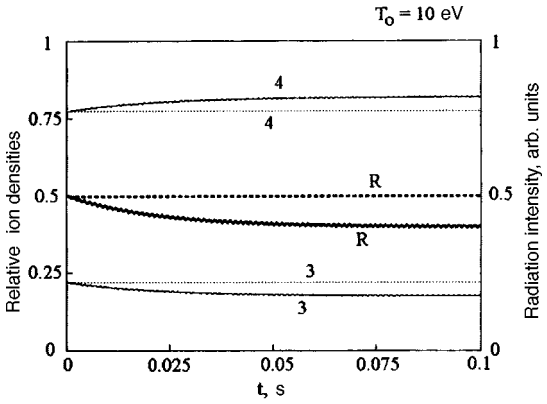

FIG. 1. Time-dependence of the relative densities of different carbon ions and line radiation intensity (in relative units) for average temperature $T_e = 10$ eV. The numbers on the curves are the ion charge. The curve for the line radiation intensity is marked with the letter R. The densities of ions with charges 0, 1, 2, 5, and 6 are so small that the corresponding curves are indistinguishable from the horizontal axis.

were calculated according to the ''coronal'' formulas of the type given in Ref. 5, using excitation cross sections given in Ref. 6 and oscillator strengths and transition energies in Refs. 7 and 8.

Figures 1 and 2 display the time dependences of the relative densities and line radiation intensities for an experimental spectra of oscillations approximated in the form given in Ref. 2 with $n_e = 10^{13}$ cm^{-3} (the electron density determines mainly the relaxation time). The radiation losses are normalized to the losses in the stationary case, where the temperature is constant and equal to the time averag of the oscillating temperature; in addition, this ratio is multiplied by 1/2 so that the corresponding curves would fit onto the same figure with relative densities. The relative ion densities corresponding to equilibrium (stationary limit) at constant temperature, equal to the average value of the oscillating temperature, were taken as the initial conditions. Figure 1 corresponds to the

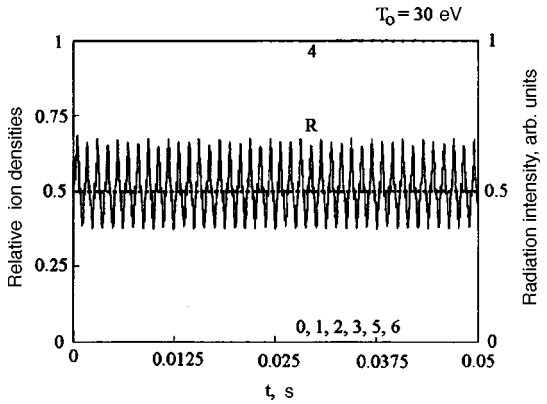

FIG. 2. Same as in Fig. 1 for an average temperature $T_e = 30$ eV. The relative density of the heliumlike ions is very close to 1.

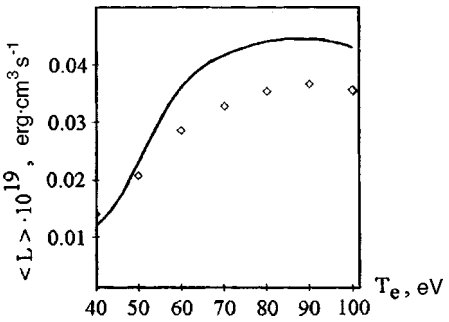

FIG. 3. Time-averaged carbon line radiation intensity near the second peak. Solid line — for a constant temperature; points — for an oscillating temperature with the same average value.

average temperature $T_e = 10$ eV. The most representative ions are ions with charges of 3 and 4. The relative densities of all other ions are so low that on the scale chosen they fall on the horizontal axis. It is clearly seen how the relative densities and the intensity of the radiation deviate from these values as result of temperature fluctuations.

The curves in Fig. 2 correspond to $T_e = 30$ eV. The most representative ions in this case are lithiumlike and heliumlike carbon ions, the average densities being 99.8% for the virtually nonradiating heliumlike ions and 0.13% for the lithiumlike ions responsible for the radiation. The quantities of all other ions are negligible. The oscillations of the radiation are due to the oscillations of the density of lithiumlike ions. In the present case an intermediate situation occurs: The relaxation time of the density of the most representative, heliumlike ion is long compared with the characteristic time of the temperature oscillations. The relaxation time of the density (together with the intensity of the line radiation also) of the most strongly radiating lithiumlike ion is comparable to the characteristic time of the temperature oscillations. As a result, the oscillations of the density of the C^{+3} ion (and together with it, the intensity of the line radiation) follow the temperature oscillations virtually adiabatically; in addition, as one can see from the figure, the absolute amplitude of the density oscillations is small, whereas the relative magnitude of the radiation intensity oscillations is by no means small. Our numerical calculations for higher temperatures (50–1000 eV) give results that are similar to those shown in Figs. 1 and 2.

We note that in all cases presented above the displacement of equilibrium is much larger than expected according to the perturbation theory, since at the amplitude chosen for the temperature oscillations the exponential ionization coefficients cannot be expanded in a series.

The time-averaged total radiation losses for carbon are presented in Fig. 3. The radiation losses for constant temperature, which are virtually identical to the results of earlier calculations,[9,10] are also shown for comparison. For T_e near 10 eV 30% temperature oscillations can lead to a factor of 1.5 increase in the radiation losses. At temperatures corresponding to the second radiation maximum (Fig. 3) the temperature derivative of the line radiation intensity, which determines the stability boundary of the radiation and the radiation-condensation modes, varies even more strongly.[11]

So, we see that nonthermal temperature fluctuations can substantially alter the equi-

librium (in the stationary limit) values of the time-averaged thermodynamic parameters of the system. Specifically, if the characteristic time of the temperature oscillations is much shorter than the relaxation time of the system, then in the stationary limit the displacement of the time-averaged parameters of the system is much larger than the amplitude of their oscillations. This effect was demonstrated analytically and numerically for the example of ionization equilibrium and radiation of impurities in a coronal plasma. The effect is important in virtually any system with nonstatistical temperature fluctuations.

[a)]e-mail: gervids@glasnet.ru

---

[1] Yu. I. Galushkin, V. I. Gervids, and V. I. Kogan, in *Proceedings of the 4th International Conference on Plasma Physics and Controlled Nuclear Fusion Research*, IAEA, Madison, Wis., 1971, Vol. 2, p. 407.
[2] P. Liewer, Nucl. Fusion **25**, 543 (1985).
[3] W. Lots, Astrophys. J., Suppl. **14**, 207 (1967).
[4] G. Knorr, Z. Naturforsch. A **13**, 941 (1958).
[5] D. Kh. Morozov, J. J. E. Herrera, and V. I. Gervids, in *Sixth International Workshop on Plasma Edge Theory in Fusion Devices*, Oxford, U.K., September 15–17, 1997.
[6] E. Hinnov, MATT-777, 1970.
[7] C. Moore, Atomic Energy Levels NSRD-NBS, **35**, 1971.
[8] M. W. Smith and W. L. Wiese, Astrophys. J., Suppl. Ser. **23**, 103 (1971).
[9] V. I. Gervids and V. I. Kogan, JETP Lett. **21**, 150 (1975).
[10] D. E. Post, R. V. Jensen, C. B. Tarter *et al.*, At. Data Nucl. Data Tables **20**, 397 (1977).
[11] B. Lipshultz, J. Nucl. Mater. **145–147**, 15 (1987).

Translated by M. E. Alferieff

Polarization of the high harmonics of radiation in a laser plasma

V. P. Silin

P. N. Lebedev Physical Institute, Russian Academy of Sciences, 117924 Moscow, Russia

(Submitted 14 January 1998; resubmitted 30 January 1998)
Pis'ma Zh. Éksp. Teor. Fiz. **67**, No. 5, 313–316 (10 March 1998)

The polarization of the high harmonics generated in plasmas by the bremsstrahlung of electrons oscillating under the influence of high-power plasma-heating electromagnetic radiation is described on the basis of a simple model of a cold plasma. It is shown that when the polarization of the heating radiation differs from plane polarization by a small but finite amount, the high harmonics are generated with almost perpendicular polarization, and the degree of circular polarization of the harmonics increases with the number of the harmonic. © *1998 American Institute of Physics.* [S0021-3640(98)00505-2]

PACS numbers: 52.50.Jm, 42.65.Ky

In recent years marked attention has been directed in both experimental (see, e.g., Refs. 2 and 3) and theoretical (see Ref. 4 and 5) investigations toward the generation of high odd-harmonic radiation in plasma owing to the bremsstrahlung of electrons oscillating in the pump field, a phenomenon predicted in 1964.[1] The specific reason for this is that the switch to short laser pulses made it possible to produce comparatively easily conditions under which the energy of electron oscillations in the field of the heating radiation is much higher than the random electron energy. In the present letter the qualitative properties of the generation of high harmonics of the plasma heating radiation that are due to the polarization of this radiation are determined theoretically for such conditions.

We shall assume that the radiation heating the plasma is elliptically polarized, so that $\mathbf{E}=(E_x,E_y,0)$, where $E_x=Ee_x\cos\omega t$ and $E_y=-Ee_y\sin\omega t$. Here $e_x^2+e_y^2=1$ and, for simplicity, it is assumed that $e_x\geqslant e_y\geqslant 0$. Correspondingly, the Stokes parameters characterizing the polarization[6] have the form $\xi_1=0$, $\xi_2=-2e_xe_y=A$, and $\xi_3=e_x^2-e_y^2\equiv\rho^2$, where A is the degree of circular polarization. An electron in such an electric field oscillates with velocity $\mathbf{u}_E=(u_{Ex},u_{Ey},0)$, where $u_{Ex}=v_Ee_x\sin\omega t$ and $u_{Ey}=v_Ee_y\times\cos\omega t$. Here $v_E=eE/m\omega$ characterizes the magnitude of the oscillatory velocity, e is the electron charge, and m is the electron mass. The frequency of the plasma heating radiation is assumed to be much higher than the effective electron–ion collision frequency in the high-power radiation field $(mv_E^2\gg\kappa_BT)$:[1,3,4,7] $\nu(E)=8\sqrt{2}\pi Ze^4n_e\Lambda m^{-2}|v_E|^{-3}$. Here $Z=\Sigma_ie_i^2n_i/e^2n_e$, e_i is the ion charge, n_e and n_i are the electron and ion number densities, and the summation extends over all types of ions.

In contrast to Ref. 1, we shall employ the simplified approach of Ref. 4, which is

based on the application of the Landau electron–ion collision integral neglecting low orders of the electron–ion mass ratio. The logarithmic accuracy of the Landau approach will require indicating below the field dependence of the Coulomb logarithm.

Following the approach of Ref. 1 and in accordance with Ref. 4, we multiply the kinetic equation and the electron velocity vector by the electron charge and integrate over velocity space, thereby obtaining for the collision-induced perturbation $\delta\mathbf{j}$ of the electric current density

$$\frac{\partial \delta\mathbf{j}}{\partial t} = -\frac{4\pi e^4 Z n_e \Lambda_e}{m^2}\int d\mathbf{v}\frac{\mathbf{v}}{v^3}F(\mathbf{v}-\mathbf{u}_E(t)) = -en_e\nu(E)\mathbf{u}_E(t)\left|\frac{v_E}{\sqrt{2}\mathbf{u}_E(t)}\right|^3. \tag{1}$$

Here the electron distribution function $F(\mathbf{u})=n_e\delta(\mathbf{u})$ was used, completely neglecting the disordered electron motion. The desired description of the generation of radiation harmonics is obtained by using the Fourier expansion (cf. Ref. 7)

$$\left|\frac{v_E}{\sqrt{2}\mathbf{u}_E(t)}\right|^3 = \frac{1}{(1-\rho^2\cos 2\omega t)^{3/2}} = A_0^{(3/2)}(\rho^2) + 2\sum_{l=1}^{\infty} A_l^{(3/2)}(\rho^2)\cos 2l\omega t. \tag{2}$$

Applying the Fourier expansion, well known in potential theory, to the solutions of the Laplace equation, according to Ref. 8 (Eq. 3.10.5 on p. 167 of the Russian edition) or Ref. 9 (Eq. (155) on Russian p. 271), we have

$$A_l^{(3/2)}(\rho^2) = \frac{1}{|A|^{3/2}}P^l_{1/2}\left(\frac{1}{|A|}\right)\frac{\Gamma(3/2-l)}{\Gamma(3/2)}, \tag{3}$$

where $\Gamma(z)$ is the Euler function and $P^l_\nu(z)$ are the generalized spherical functions or Legendre functions.

Substituting expression (2) into Eq. (1) gives immediately

$$\frac{\partial \delta j_x}{\partial t} = -e_x E\frac{\omega_{Le}^2}{4\pi}\sum_{l=0}^{\infty}\frac{\nu(E,l)}{\omega}\sin[(2l+1)\omega t][A_l^{(3/2)}-A_{l+1}^{(3/2)}], \tag{4}$$

$$\frac{\partial \delta j_y}{\partial t} = -e_y E\frac{\omega_{Le}^2}{4\pi}\sum_{l=0}^{\infty}\frac{\nu(E,l)}{\omega}\cos[(2l+1)\omega t][A_l^{(3/2)}+A_{l+1}^{(3/2)}], \tag{5}$$

where $\omega_{Le}=\sqrt{4\pi e^2 n_e/m}$ is the electronic plasma frequency. From Eqs. (4) and (5) it follows, specifically, that the harmonic radiation field, like that of the heating radiation, is completely elliptically polarized.

Let us examine the dependence of the collision frequency $\nu(E,l)$, which we have introduced heuristically, on the number $(2l+1)$ of the odd harmonic. Here it should be recalled that the Coulomb logarithm $\Lambda=\ln(r_{\max}/r_{\min})$ is determined by the ratio of the maximum and minimum impact parameters which delimit the region of applicability of the Landau logarithmic approximation. In a high-frequency field the maximum impact parameter is determined by the ratio of the electron velocity to the frequency (in our case the harmonic frequency). In the case of a weak field this was established in Refs. 10 and 11, where the velocity was the thermal velocity. In the high-field limit $r_{\max}\simeq|v_E|/(2l$

$+1)\omega$. The minimum impact parameter is determined by the larger of the two values $r_{\min,cl}=Ze^2/mv_E^2$ and $r_{\min,q}=\hbar/m|v_E|$. In a sufficiently strong heating field, such that $\hbar|v_E|>Ze^2$, the latter (quantum) case is realized. Therefore

$$\Lambda=\ln\frac{mv_E^2}{\hbar\omega(2l+1)},\quad |v_E|>\frac{Ze^2}{\hbar}\quad\text{or}\quad \Lambda=\ln\frac{m|v_E|^3}{Ze^2\omega(2l+1)},\quad |v_E|<\frac{Ze^2}{\hbar}. \tag{6}$$

The fact that the Coulomb logarithm decreases for large values of l may be one one of the reasons why the series (4) and (5) essentially terminate.

Let us now discuss the polarization properties of the high harmonics generated in the plasma, corresponding to the consequences of Eqs. (5) and (6). In the first place, we note that for $\rho^2=0$, when the radiation is circularly polarized in accordance with Ref. 1, there are no harmonics. As follows from the properties of the Legendre functions, the number of harmonics is increasingly greater the closer the polarization is to plane polarization. Therefore we shall assume that $e_y^2\ll e_x^2$ or, equivalently,

$$A^2\ll 1. \tag{7}$$

In this case, using the well-known asymptotic expansion of the Legendre functions (see, e.g., Ref. 9, Russian p. 204) we have

$$A_l^{(3/2)}(\rho^2)=\frac{2^{3/2}}{\pi A^2}\left\{1-\frac{l^2A^2}{4}\left[\ln\left(\frac{4}{l^2A^2}\right)-2C+1\right]\right\},$$

where $C=0.577\ldots$ is the Euler number. Then we obtain for the Fourier coefficients in Eqs. (4) and (5)

$$e_x[A_l^{(3/2)}-A_{l+1}^{(3/2)}]\simeq\frac{2^{1/2}}{\pi}l\left[\ln\left(\frac{4}{A^2l^2}\right)-2C\right], \tag{8}$$

$$e_y[A_l^{(3/2)}+A_{l+1}^{(3/2)}]\simeq\frac{2^{3/2}}{\pi|A|}. \tag{9}$$

Here the fact that $A\cong 2e_y$ has been taken into account. The asymptotic formulas (8) and (9) hold only when $A^2l^2\ll 1$. When the last condition is violated (but relation (8) holds) we have

$$A_l^{(3/2)}(\rho^2)\cong 2\sqrt{\frac{l}{\pi|A|^3}}\exp(-l|A|). \tag{10}$$

This means that if the Coulomb logarithm (6) does not terminate the Fourier series (4) and (5), then the number of harmonics terminates at $l\sim|A|^{-1}$.

A remarkable property of Eqs. (8) and (9) is that when the plasma heating radiation is polarized almost along the x axis, the field of the high harmonics which are generated is polarized almost along the y axis on account of the condition $A^2l^2\ll 1$. It is easy to conclude on the basis of Eqs. (4), (5), (8), and (9) that the degree of circular polarization $A^{(l)}$ of the high $(2l+1)$-th harmonic increases with the harmonic number as

$$|A^{(l)}| = l|A| \left[\ln\left(\frac{4}{A^2 l^2}\right) - 2C \right]. \tag{11}$$

The degree of maximum plane polarization $L^{(l)} = \sqrt{1-|A^{(l)}|^2}$ decreases accordingly. The polarization property established here for the high harmonics contrasts sharply with the oft-repeated result of Ref. 1 that in the case of plane-polarized heating radiation the high harmonics have exactly the same plane polarization. The obvious contradiction arising with such a comparison is due to the fact that the polarization law established in the present letter was derived in complete neglect of the thermal motion of the electrons. In this connection it should be noted that in Ref. 7 it is shown that the thermal motion in the case of a strong radiation field ($v_E^2 \gg v_T^2 = \kappa_B T/m$) can be neglected only if

$$1-\rho^4 = A^2 \gg v_T^2/v_E^2 .$$

However, if the degree $|A|$ of circular polarization is so small that the opposite inequality holds, then, according to Ref. 1, when the thermal motion is taken into account expression (8) is replaced by $l\ \ln(|v_E|/v_T l)$, while instead of Eq. (9) we have $\sim A(v_E^2/v_T^2)$, which gives the plane-polarized radiation limit ($A=0$) of Ref. 1 (cf. also Ref. 4).

We note here that according to Eqs. (4) and (5) the polarization anomaly also occurs for the fundamental harmonic, determining the inverse bremsstrahlung absorption of the plasma. The anomalous y component is absorbed more efficiently, as a result of which the degree of circular polarization A of the heating radiation decreases. The law describing such behavior under the condition (7), as follows from Eqs. (4) and (5) using Eqs. (8) and (9), has the form $(A^2/64)[\ln(64/A^2)+1] - (1/4)\ln|v_E/v_T| = \text{const}$.

Finally, it should be noted that the results of the present analysis in the case of quite intense radiation can be carried over to the model of bremsstrahlung of an atomic electron in a high field. This is easy to see by comparing the plasma model of Ref. 1 with atomic model of Ref. 12 of the generation of high harmonics.

In summary, in this paper the polarization of high harmonics in a plane almost perpendicular to the pump polarization has been described theoretically in a simple model of a cold plasma, corresponding to the case where the electron thermal energy is much less than the energy of the electron oscillations in the field of nearly plane-polarized heating radiation. The law of variation of the degree of circular polarization with increasing harmonic number was established. It was shown for the fundamental harmonic that the polarization exhibits nonlinear variation upon absorption of the plasma-heating radiation. This phenomenon is similar to one established in Ref. 7, viz., the polarization anomaly of the low-frequency conductivity of a plasma heated by inverse bremsstrahlung absorption.

This work was supported by the Council on Grants of the President of the Russian Federation and on Government Support of the Leading Scientific Schools (Project 96-15-96750), by the Russian Fund for Fundamental Research (Project 96-02-17002), and as part of the Russian–Italian joint Project ''New coherent sources of ultrashort pulses,'' set up in compliance with Law No. 212/92 of the Italian government.

[1] V. P. Silin, Zh. Éksp. Teor. Fiz. **47**, 2254 (1964) [Sov. Phys. JETP **20**, 1510 (1965)].
[2] S. M. Gladkov and N. I. Koroteev, Usp. Fiz. Nauk **160**, 105 (1990) [Sov. Phys. Usp. **33**, 554 (1990)].
[3] F. Giammanco, P. Ceccherini, C. Tagliavini *et al.*, Laser Phys. **7**, 22 (1997).

[4] G. Ferrante, S. A. Uryupin, M. Zarcone, and P. I. Porshnev, J. Opt. Soc. Am. B **14**, 1716 (1997).
[5] F. Giammanco and N. Spinelli (eds.), *Plasma Collective Effects in Atomic Physics*, Edizioni ETS, Pisa, 1996.
[6] L. D. Landau and E. M. Lifshitz, *The Classical Theory of Fields*, 4th English ed., Pergamon Press, New York, 1975 [Russian original, Nauka, Moscow, 1973].
[7] V. P. Silin, Zh. Eksp. Teor. Fiz. **111**, 478 (1997) [JETP **84**, 262 (1997)].
[8] A. Erdélyi (ed.), *Higher Transcendental Functions* (Bateman Manuscript Project), McGraw-Hill, New York, 1953, Vol. 1 [Russian translation, Nauka, Moscow, 1965].
[9] E. W. Hobson, *The Theory of Spherical and Ellipsoidal Harmonics*, Cambridge University Press, Cambridge, 1931 [Russian translation, Izd. Inostr. Lit., Moscow, 1960].
[10] H. A. Kramers, Philos. Mag. **46**, 836 (1923).
[11] V. L. Ginzburg, *The Propagation of Electromagnetic Waves in Plasmas*, 2nd ed., Pergamon Press, New York, 1970 [cited Russian original, 1st ed., Gostekhizdat, Moscow, 1960].
[12] R. V. Parapetyan and V. B. Fedorov, Kratk. Soobshch. Fiz., No. 7, 8, p. 76 (1995).

Translated by M. E. Alferieff

Fractal clusters and self-propagating high-temperature synthesis in thin Al/Ge films

V. G. Myagkov and L. E. Bykova
L. V. Kirenskiĭ Institute of Physics, Siberian Branch of the Russian Academy of Sciences, 660036 Krasnoyarsk, Russia

(Submitted 12 January 1998)
Pis'ma Zh. Éksp. Teor. Fiz. **67**, No. 5, 317–321 (10 March 1998)

Fractal clusters in amorphous thin films are examples of growth models. The main models are the Witten–Sander model and its modifications. It is believed that fractal patterns are formed in the course of the crystallization of an amorphous phase. It is shown that self-propagating high-temperature synthesis can be initiated in an Al/Ge film system and fractal patterns are formed in the reaction products. It is conjectured that the transition of an amorphous phase to a crystalline phase does not play a substantial role in the appearance of such patterns, while the formation of fractal clusters is determined by self-propagating high-temperature synthesis. © *1998 American Institute of Physics.* [S0021-3640(98)00605-7]

PACS numbers: 81.20.Ev, 81.20.Ka, 81.15.Tv, 61.43.Hv

Fractal clusters often arise in amorphous films after thermal influences have acted.[1–9] It is believed that the amorphous structure plays an important role in the formation of fractal patterns, where fractal clusters form during a phase transition from an amorphous to a crystalline phase. The most closely studied system in which fractal clusters form is Al–Ge. Two research groups are investigating the formation of fractal patterns in this system. The first group[3,4] is studying the formation of fractal clusters in Ge/Au and Al/Ge bilayer film systems obtained by annealing. The second group[5–9] obtains film samples by simultaneous deposition from two sources. The structure of such films consists of aluminum microcrystallites embedded in an amorphous matrix. After the samples are heated, clusters with a dense branching morphology (DBM) with fractal dimension $d_f=2$ form. Clusters with a DBM, which occur widely in real systems, have been observed during the crystallization of Al–Ge thin films.[9] For all samples, clusters form in the temperature range 470–500 K. Different growth models have been proposed to explain the nucleation of clusters with fractal morphology in the Al–Ge system. The first group is developing a random nucleation model. The second group is employing in its investigations a combined model consisting of the Eden model and a diffusion-limited aggregation (Witten–Sander) model. Both groups believe that diffusion between aluminum and germanium proceeds in the solid phase.

A large number of materials and compounds has been obtained by self-propagating high-temperature synthesis (SHS) based on powders. The compounds $GeAl_2$ and Ge_5Al_2

have also been synthesized by this method. This reaction is weakly exothermic and therefore requires preheating.[10]

The present letter is devoted to SHS in Al/Ge thin films. It is concluded that SHS, which occurs between layers of aluminum and germanium particles, is the governing process leading to the formation of fractal patterns in bilayer films and in films with a dispersed structure. The specific nature and kinetics of SHS in bilayer thin films are described in Ref. 11, where it is shown that the autowave mechanism of SHS in thin films is similar to the process of explosive crystallization. If a bilayer film system is placed in a uniform temperature field, then above the initiation temperature T_0 a nucleus of reaction products forms on the film surface and propagates along the surface of the sample by a self-maintaining mechanism. Since the formation enthalpy of the reaction products is much higher than the latent heat of the amorphous-to-crystalline phase transition, the temperature at the SHS front is much higher than the temperature of the front in the case of explosive crystallization.

A method of preparing Al/Ge film condensates and a method of initiating SHS in them are described in Ref. 11. Film samples were obtained by successive deposition of a layer of germanium followed by a layer of aluminum on glass or mica substrates 5×10 mm in size and 0.2 mm thick. To crystallize the germanium layer after it is deposited, some samples were annealed for 10 min at 450 °C. This temperature is higher than the crystallization temperature of germanium.[12] Next, a layer of aluminum was deposited on top at a temperature of 50 °C. Al/Ge samples with different layer thicknesses but with a total film thickness of 100–250 nm were used in the experiments.

The samples obtained were placed in a tungsten heater and heated at a rate higher than 1 K/s up to the temperature T_0 at which a reaction started (Fig. 1b). The initiation temperature was in the range 430–500 K. Near the temperature T_0 the velocity V_f of the front was of the order of $(0.2–0.3)\times 10^{-2}$ m/s and increased strongly with temperature. The temperature T_0 did not depend on the ratio of the layer thicknesses and the total film thickness, but it did depend on the heating rate and the condensate deposition conditions. The SHS process on Al/Ge film samples is similar to the SHS process observed earlier on Al/Ni, Al/Co, and Al/Fe films.[11] After the SHS wave, a second front passed along the reacted sample. The process started at the film edges and propagated toward film center. The velocity of the second front at temperature T_0 was of the order of 0.1 mm/s and increased rapidly with decreasing temperature. In Ref. 11 the temperature of the SHS front was estimated to be higher than the melting temperature of aluminum $T_M(\mathrm{Al}) = 943$ K. For different powder-based systems the SHS temperature does not fall below 1300 K.[10] For this reason, it is surmised that the temperature of the SHS front in the Al/Ge system should also be higher than $T_M(\mathrm{Al})$. Hence it follows that a liquid region, consisting of aluminum and reaction products, exists on the surface of the film. A schematic explanation of this region is given in Fig. 1c.

The surface of the sample is divided conventionally into three parts with different microstructure: the initial part of the sample, the heating zone, and the region of reaction products. Figure 1a shows the microstructure of all three regions. The initial part of the sample has the uniform microstructure of an ordinary aluminum film. Pores 2–8 μm in size appear in the heating zone. Analysis shows that these pores appear in the germanium film and become filled with aluminum (Fig. 1). The microstructure of the reacted samples is diverse and very sensitive to the experimental conditions. For slow heating rates η

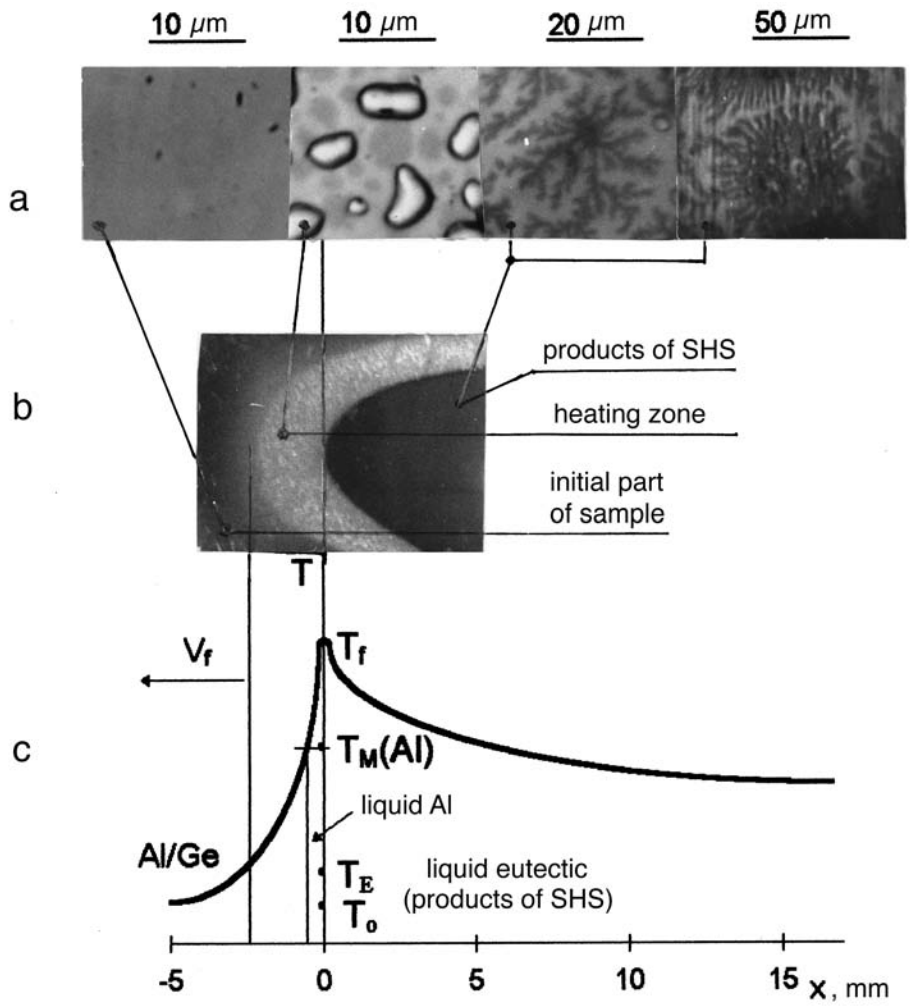

FIG. 1. SHS in an Al(100 nm)/Ge(120 nm) thin-film system. a) Microstructures of the initial sample, the heating zone, and the products of SHS. Only fractal and DBM clusters are shown in the microstructures of the reaction products. b) Photograph of the SHS wave dividing the sample into the initial part, the heating zone, and the reaction products. c) Schematic representation of the temperature front of SHS, elucidating the appearance of a liquid region after passage of the combustion wave.

$\sim$1 K/s up to the initiation temperature and slow cooling the same fractal clusters as those obtained by the first group[4] and the same cluster DBM as that obtained by the second group arise.[6–9] For high rates of heating $\eta \gg 1$ K/s the fractal patterns vanish and a labyrinthine structure appears. The condition of heat removal into the substrate also plays an important role in the formation of the film microstructure. Thus, the samples on whose substrate a germanium layer followed by an aluminum layer were deposited show a uniform microstructure similar to that of the initial film. The experiments show that the crystalline or amorphous state of the germanium film does not influence the kinetics and

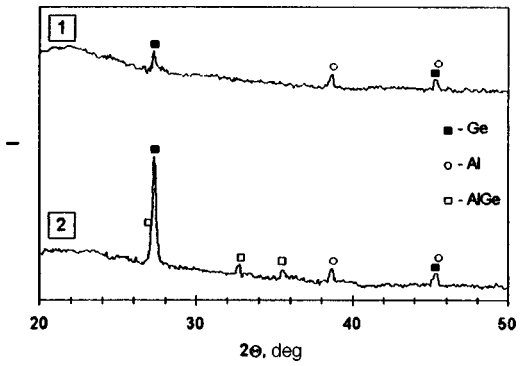

FIG. 2. Diffraction patterns of Al(100 nm)/Ge(120 nm) thin-film samples before (*1*) and after (*2*) passage of a SHS wave.

basic parameters of SHS (initiation temperature, front velocity, microstructure of the reaction products).

This is all based on the following mechanism of SHS in Al/Ge thin films. The temperature of the SHS front is higher than T_M(Al). The temperature of the reaction products is higher than the temperature T_E of the eutectic (Fig. 1c). The formation of pores in the heating zone greatly increases the active contact area between Al and Ge. Intense interlayer diffusion occurs on the SHS front when the temperature of the front is higher than the melting temperature of Al, $T_f > T_M(\mathrm{Al}) = 933$ K. The temperature of the reaction products is also higher than that of the eutectic $T_E = 698$ K. After passage of the SHS wave and after thermal relaxation at a temperature equal to T_E, eutectic crystallization occurs, which gives rise to a second front.[13] This suggests that fractal patterns form from a liquid phase. This does not correspond to the results of Refs. 3–9, where a solid-phase mechanism of fractal cluster formation is studied. The system Al–Ge is a simple eutectic system with a complicated regular microstructure.[13] The initiation temperature of SHS in Al/Ge films in our experiments is equal to the temperature at which fractal clusters appear both in bilayer Ge/Al films[4] and in films obtained by simultaneous deposition.[5–9] This suggests that the fractal clusters studied in these works arise after SHS.

The phase composition before and after the SHS reaction was determined by x-ray crystallographic analysis. Figure 2 shows the diffraction pattern of the initial Al(100 nm)/Ge(120 nm) film with a crystalline layer of germanium and the diffraction pattern of the reacted sample. The diffraction patterns show that the initial Al and Ge layers were polycrystalline. After SHS strong diffraction reflections from germanium and aluminum, corresponding to an increase in grain size, appear and new reflections, which can be interpreted as the appearance of a metastable AlGe phase in the reaction products, arise.[14] The results obtained for films differ from the data obtained for powders,[10] and they confirm the conclusion drawn in the present work that phase separation is observed after eutectic solidification.

On this basis, the initiation of SHS and the formation of fractal patterns in the reaction products should also be expected to occur in other film systems where fractals have been observed.[1,2]

This work pursues two objectives. The first one is to show that SHS can play a determining role in the formation of fractal patterns. The second one is to study the mechanisms leading to the formation of fractal clusters and to improve the understanding of the micromechanisms of SHS.

[1] B. X. Liu, L. J. Huang, K. Tao *et al.*, Phys. Rev. Lett. **59**, 745 (1987).
[2] W. T. Elam, S. A. Wolf, J. Sprague *et al.*, Phys. Rev. Lett. **54**, 701 (1985).
[3] J. G. Hou and Z. Q. Wu, Phys. Rev. B **42**, 3271 (1990).
[4] B. Q. Li, B. Zheng, and Z. Q. Wu, Phys. Rev. B **47**, 3638 (1993).
[5] S. Alexander, R. Bruinsma, R. Hilfer *et al.*, Phys. Rev. Lett. **60**, 1514 (1988).
[6] G. Deutscher and Y. Lereah, Phys. Rev. Lett. **60**, 1510 (1988).
[7] Y. Lereah, G. Deutscher, and E. Grunbaum, Phys. Rev. A **44**, 8316 (1991).
[8] Y. Lereah, I. Zarudi, E. Grunbaum *et al.*, Phys. Rev. E **49**, 649 (1994).
[9] E. Ben-Jacob, G. Deutscher, P. Garik *et al.*, Phys. Rev. Lett. **57**, 1903 (1986).
[10] A. G. Merzhanov, in *Physical Chemistry* [in Russian], edited by Kolotyrkin, Khimiya, Moscow, 1983, pp. 6–45.
[11] B. G. Myagkov and L. E. Bykova, Dokl. Akad. Nauk SSSR **354**, 777 (1997).
[12] V. A. Shklovskiĭ and V. M. Kuz'menko, Usp. Fiz. Nauk **157,** 311 (1989) [Sov. Phys. Usp. **32**, 163 (1989)].
[13] A. I. Somov and M. A. Tikhonovskiĭ, *Eutectic Compositions* [in Russian], Metallurgiya, Moscow, 1975.
[14] *ICDPS-Diffraction Data Cards and Alphabetical and Grouped Numerical Index of X-Ray Diffraction Data*, International Center for Diffraction Data, Philadelphia, 1990.

Translated by M. E. Alferieff

Magnetic ordering of Dy in NiFe–Dy bilayer films

I. S. Édel'man,[a] A. E. Khudyakov, V. N. Zabluda, V. V. Markov, and O. B. Romanova

L. V. Kirenskiĭ Institute of Physics, Siberian Branch of the Russian Academy of Sciences, 660036 Krasnoyarsk, Russia

(Submitted 14 January 1998)
Pis'ma Zh. Éksp. Teor. Fiz. **67**, No. 5, 322–325 (10 March 1998)

The first results of measurements of the temperature and spectral dependences of the circular magnetic dichroism in NiFe–Dy bilayer films are reported. These results show that even at room temperature Dy in such systems is ordered ferromagnetically to a large depth (~600 Å).
 [S0021-3640(98)00705-1]

PACS numbers: 75.70.Cn, 78.66.Bz

In the last few years much attention has been devoted to the problems of the magnetic ordering of layered systems, including layers of rare-earth metals (REMs). Many authors note that in very thin layers of REMs spin polarization or magnetic ordering exists as a result of the interaction with layers of transition metals (TMs). In Ref. 1 it is asserted that in Fe/REM multilayer films with layer thicknesses of 40 Å and 10–30 Å respectively, the REM layers are ordered at room temperature either ferromagnetically (Pr, Nd) or antiferromagnetically (Dy, Tb). Similar conjectures were made in Ref. 2 in order to explain the magnetic properties of thin Fe films coated with a 14 Å thick layer of Tb. In Ref. 3 it was observed directly that at room temperature Dy makes an appreciable contribution to the total magnetization in Fe/Dy multilayers with a 12 Å thick Dy layer.

While studying the temperature and spectral dependences of the circular magnetic dichroism (CMD) in bilayer NiFe–Dy films, we discovered that right up to Dy layer thicknesses ~600 Å the contribution of Dy to the CMD of a bilayer film at room temperature corresponds in magnitude to the CMD in a single-layer Dy film of the same thickness but measured at a temperature below the temperature of the transition of Dy into a ferromagnetic state ($T_c = 85$ K).

We report in the present letter the results of an investigation of the CMD of NiFe–Dy bilayer films as a function of the thickness of the Dy layers.

The samples were prepared by thermal deposition in an ultrahigh vacuum; vacuum-melted $Ni_{80}Fe_{20}$ and DiM1-grade Dy were deposited at a rate of 0.05 Å/s and 2 Å/s, respectively, on a glass substrate (optical quality, polished, and 0.8 mm thick) at temperature 250 °C. Three samples were obtained in a single cycle by means of special shutters: Dy, NiFe, and Dy–NiFe, or NiFe–Dy. The layer thicknesses were ~50 Å for NiFe and 50 to 900 Å for Dy.

To measure the CMD the polarization state of the light was modulated by the method described in Ref. 4 in the spectral interval from 350 to 650 nm, in the temperature

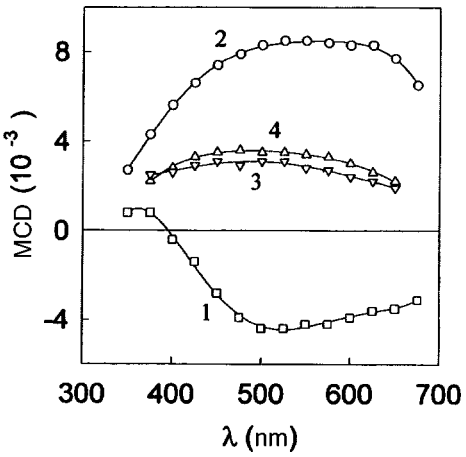

FIG. 1. Dispersion curves of CMD for the samples: *1*) Dy, $d=805$ Å, $T=80$ K; *2*) NiFe, $d=53$ Å, $T=300$ K; *3,4*) NiFe–Dy, $d_{\mathrm{NiFe}}=53$ Å, $d_{\mathrm{Dy}}=805$ Å, $t=80$ K and 300 K, respectively, in a field $H=3.5$ kOe.

interval from 300 to 80 K, and in a 3.5 kOe magnetic field applied in a direction perpendicular to the plane of the samples. Cooling was done in a flow-through cryostat in a nitrogen stream and the temperature was regulated with a PIT-3 precision isodromic temperature regulator.

Figure 1 show the spectral dependences of the CMD for single-layer Dy and NiFe films (curves *1* and *2*), obtained at $T=80$ K and $T=300$ K, respectively. We note that the CMD of these materials has never been measured before. One can see that for wavelengths $\lambda>400$ nm the CMD in Dy and NiFe has different signs and the curves pass through a maximum at ~ 525 nm for Dy and ~ 550 nm for NiFe. The CMD of Dy passes through zero at $\lambda\sim 400$ nm and then has the same sign as CMD in NiFe. As temperature increases, the CMD of Dy decreases for all wavelengths similarly to curve *1* in Fig. 2 for $\lambda=525$ nm. Curves *3* and *4* in Fig. 1 correspond to CMD in NiFe–Dy bilayer films at $T=80$ K and $T=300$ K, respectively. One can see that the dysprosium spectra at room temperature and at a temperature below T_c are virtually identical, and the magnitude of the CMD of the bilayer film is close to the sum of the CMD in unilayer Dy and NiFe films.

Figure 2 shows the temperature dependences of the CMD for NiFe, Dy, and NiFe–Dy bilayer films. The CMD of Dy (curve *1*) varies very strongly with temperature. Here one can see that the temperature variation of the CMD has a somewhat smoother form than the published temperature dependence of the magnetization of bulk Dy samples (see, for example, Ref. 5). This is apparently explained by the difference in the properties of a polycrystalline film and bulk Dy single crystals. As expected, the CMD in NiFe (curve *2*) remains approximately constant in this interval. Curve *3* shows the temperature variation of the CMD in two isolated Dy and NiFe films (~ 600 Å and ~ 50 Å thick, respectively) combined together. One can see that the CMD in this case depends on the temperature, while the CMD (curve *4*) for a bilayer film with Dy thickness ~ 600 Å and NiFe thickness ~ 50 Å remains constant as temperature varies. The 600 Å thick Dy layer (curve *4*) at room temperature makes a contribution to the CMD that is approxi-

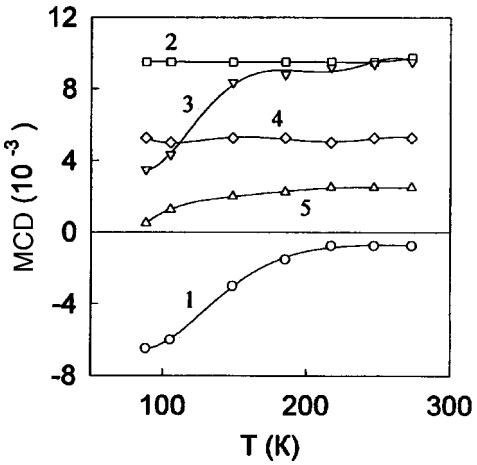

FIG. 2. Temperature dependences of CMD for the samples: *1*) Dy, $d=625$ Å; *2*) NiFe, $d=67$ Å; *3*) NiFe + Dy, $d_{NiFe}=67$ Å, $d_{Dy}=625$ Å; *4*) NiFe–Dy, $d_{NiFe}=67$ Å, $d_{Dy}=625$ Å; *5*) NiFe–Dy, $d_{NiFe}=45$ Å, $d_{Dy}=960$ Å; wavelength — 525 nm.

mately equal to the CMD of Dy at $T<T_c$. For the case when the Dy thickness in a bilayer film equals 900 Å, the picture is more complicated (curve *5*). The contribution of Dy to the CMD at high temperatures is higher than in the first case, and it increases with decreasing temperature. Comparing the curves *2*, *4*, and *5*, the Dy layer making a temperature-independent contribution to the CMD can be estimated to be roughly ~ 700 Å thick.

The behavior of the Dy–NiFe samples is similar to that described above.

One can offer different explanations of the observed spectral and temperature dependences of the CMD in bilayer films: formation of a new magnetically ordered compound as a result of atomic diffusion, ordering of Dy under the influence of NiFe, and an unusually strong effect of the interface. The effect of the interface can be immediately excluded on the basis of the temperature dependences presented. The formation of a new compound over the entire depth of the Dy layer is also unlikely — it is difficult to imagine a mechanism of uniform diffusion of NiFe to a depth exceeding 600 Å with a ~ 50 Å thick NiFe layer. Nevertheless, oxidation of the Dy in bilayer films to Dy_2O_3, which is not magnetooptically active, was performed to check the likelihood of this mechanism. Besides NiFe–Dy, Dy and NiFe films were also subjected to heat treatment at the same time. Heat treatment had virtually no effect on the CMD in the NiFe film, while the CMD in Dy decreased to the noise level (Dy is a chemically much more active metal than NiFe). The magnitude of the CMD of the bilayer film was restored to values characteristic for NiFe. If the small disordering at the interface is taken into account and estimated to be approximately 15 Å, then the curves for NiFe and oxidized NiFe–Dy become completely identical. From this it may be concluded that in a bilayer film substantial quantities of material are not transferred from the TM layer into the REM layer.

The ordering of the Dy layer could also be due to spin polarization of the conduction electrons,[6] which plays an important role, for example, in the formation of the magnetoresistance at magnetic metal–insulator–magnetic metal junctions.[7] However, atomic

microdiffusion cannot be rule out. It has virtually no effect on the properties of a TM layer, while in a REM layer it produces a low concentration of Fe and Ni atoms, which can influence the magnetic properties of this layer. For example, in Ref. 8 it was shown that small admixtures (0.03–0.06%) of iron change the paramagnetic Curie point of scandium by hundreds of degrees. Experiments designed to clarify the mechanism of Dy ordering are in progress.

[a)]e-mail: ise@iph.krasnoyarsk.su

[1]K. Mibu, N. Hosoito, and T. Shinijo, J. Magn. Magn. Mater. **126**, 343 (1993).
[2]B. Scholz, R. A. Braud, and W. Kenne, Phys. Rev. **50**, 2537 (1994).
[3]K. Yoden, N. Hosoito, K. Kawaguchi *et al.*, Jpn. J. Appl. Phys. **27**, 1680 (1988).
[4]S. N. Jasperson and S. E. Schnatterly, Rev. Sci. Instrum. **40**, 6761 (1969).
[5]K. P. Belov, *Rare Earth Magnets and Their Applications* [in Russian], Nauka, Moscow, 1980.
[6]M. Julliere, Phys. Lett. A **54**, 225 (1975).
[7]T. Miyazaki and N. Tezuka, J. Magn. Magn. Mater. **151**, 403 (1995).
[8]V. I. Chernikov, I. Pop, and O. P. Naumkin, *Problems of the Theory and Applications of the Rare Earth Metals* [in Russian], Nauka, Moscow, 1964.

Translated by M. E. Alferieff

On hydrogen localization in the β' phase of $VO_{0.2}$

S. I. Morozov

Physics and Power Engineering Institute State Science Center of the Russian Federation, Obninsk, Russia

(Submitted 15 January 1998)
Pis'ma Zh. Éksp. Teor. Fiz. **67**, No. 5, 326–328 (10 March 1998)

The results of an investigation of the dynamics of hydrogen atoms in the body-centered tetragonal lattice of the interstitial β' phase of vanadium–oxygen by the method of inelastic scattering of slow neutrons are reported. It is concluded on the basis of an analysis of the structure of the alloy investigated that hydrogen in the lattice is localized in tetrahedral interstices with the point symmetry of an almost ideal tetrahedron. © *1998 American Institute of Physics.* [S0021-3640(98)00805-6]

PACS numbers: 61.72.Ji, 61.72.Ss, 61.12.Ex, 63.20.Dj

From the standpoint of the dynamics of hydrogen in transition metals the system V–H is special. The position of localization of hydrogen in the vanadium lattice can change depending on the temperature or concentration,[1–3] applied external pressure,[4] or the presence of interstitial impurities.[5] However, the results obtained by different methods of investigation show a discrepancy in some cases. For example, according to the data obtained by the method of channeling of fast ions[5] the presence of oxygen in the vanadium lattice causes the hydrogen atoms to move from tetrahedral positions (TPs) into octahedral positions (OPs). At the same time, our investigations by the method of inelastic scattering of slow neutrons (INS) by $VO_{0.02}H_{0.02}$ samples at room temperature showed that, just as in $VH_{0.02}$, most hydrogen atoms are localized in TPs.[6]

The objective of the present work was to trace by the INS method the effect of oxygen at high oxygen concentrations, where an oxygen-ordered structure of the β' phase of V–O is formed, on the dynamics and position of hydrogen localization in the host lattice. To this end, samples of the alloys $VO_{0.2}$ and $VO_{0.2}H_{0.05}$ were prepared and measurements of the INS spectra were performed on a DIN2-PI spectrometer.[7]

The $VO_{0.2}$ sample was prepared by remelting appropriate quantities of pure vanadium and V_2O_5. The alloy with this composition possesses the structure of an oxygen-ordered tetragonal body-centered β' phase (see Ref. 8). The sample was divided into two parts, one of which was saturated with hydrogen from the gas phase up to the ratio H/V $= 0.05$. The measurements were performed on samples with and without hydrogen at room temperature and incident neutron energy $E_0 = 8$ meV. Processes with annihilation of phonons were detected in the range of scattering angles 70°–135°. A partial spectrum of the vibrational frequencies of hydrogen atoms in the range 3–140 meV was obtained in the incoherent approximation from the difference of the INS spectra of $VO_{0.2}H_{0.05}$ and $VO_{0.2}$. The result is displayed in Fig. 1.

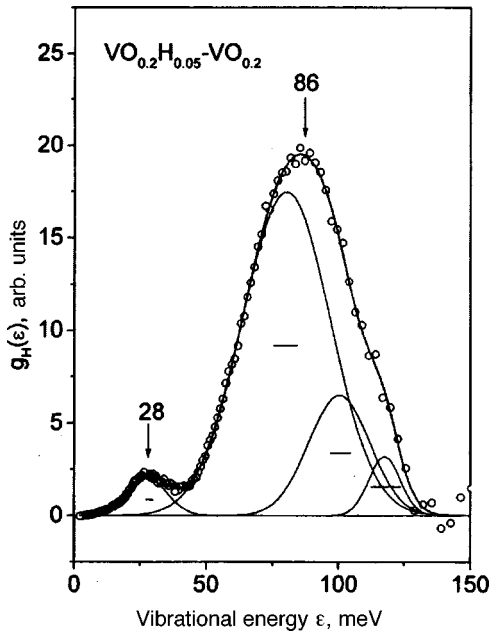

FIG. 1. Vibrational spectrum of hydrogen atoms in the interstitial β' phase of $VO_{0.2}H_{0.05}$. The peaks shown by the fine lines were extracted from the spectrum by fitting Gaussian curves to the experimental data. The thick solid line shows the total result of the description. The positions of the features marked by arrows are given in meV. The horizontal bars show the half-width of the resolution function of the spectrometer.

Since interstitial atoms interact mainly with the nearest-neighbor metal atoms, the structure of the local vibrations (LVs) should be directly related with the symmetry of the interstitial position occupied by the interstitial atom. As one can see from Fig. 1, the spectrum consists of a principal feature at $\varepsilon = 86$ meV and a small feature at $\varepsilon_1 = 28$ meV. The latter feature is due to the band modes of the hydrogen atoms in the $VO_{0.2}$ lattice. The fine lines in Fig. 1 show the peaks identified in the spectrum by a best fit of Gaussian curves to the experimental data.

The feature at $\varepsilon_4 \approx 120$ meV is probably due to the fact that some hydrogen atoms occupy TPs which are least distorted by the presence of oxygen atoms in the lattice. Indeed, the energy of the low-frequency mode of the vibrational spectrum of hydrogen in TPs of the α phase of VH_x is of the order of 120 meV.[1,2] Most hydrogen atoms (about 75%) in the $VO_{0.2}$ lattice occupy positions with a different symmetry. An estimate of the relative intensity of the $\varepsilon = 86$ meV feature in the INS spectrum of the alloy $VO_{0.2}H_{0.05}$ shows that this peak probably corresponds to a triply degenerate (or weakly split by $\varepsilon_2 \approx 80$ meV and $\varepsilon_3 \approx 100$ meV, see Fig. 1) vibrational level of the hydrogen atoms.

Such a structure is characteristic for the vibrational spectrum of light interstitial impurities in the fcc or ideal hcp lattice of the host atoms, where the T and O positions have T_d and O_h point symmetry, respectively, while such a low vibrational energy of the H atoms is usually interpreted as evidence of octahedral coordination of hydrogen.[9,10] However, the energy of the low-frequency mode of the vibrational spectrum of hydrogen in the OPs of the lattice of the β phase of V–H equals 56 meV,[1,3] which is 30 meV lower

than the energy of the observed feature. For this reason, the vibrational mode with $\varepsilon = 86$ meV cannot be attributed to hydrogen localized in OPs.

To explain the results obtained it is necessary to examine more closely the structure of the interstitial β' phase of the V–O system. This phase consists of an oxygen-ordered body-centered tetragonal (BCT) superstructure $4V_{16}O_3$ ($c/a = 1.1$), in which the metal-atom sublattice consists of $4\times4\times2$ BCT cells (space group $I4/mmm$). This interstitial phase has been investigated in detail in Ref. 8. The character of the regular displacements of the vanadium atoms in the 16(m) positions in the $4V_{16}O_3$ superstructure, caused by the ordered arrangement of the oxygen atoms, is such that octahedral interstices with O_h symmetry (or weak tetragonal distortion) which are available to hydrogen do not form in it. At the same time, because the vanadium atoms are displaced along the z axis by $\delta \approx 0.54$ Å some tetrahedral voids in this lattice, specifically, the 16(n) positions (see Ref. 11) with $x = 1/8$ and $z = 1/8 + \delta/2$, are appreciably larger in size than the TPs in pure vanadium and they possess the symmetry of an almost ideal tetrahedron. If they are occupied by light interstitial atoms, the spectrum of local vibrations should be either degenerate or weakly split. Therefore we arrive at the conclusion that the character of the local displacements of the vanadium atoms changes at a transition from the α to the β phase of V–O. Ordering of oxygen in the β' phase results in regular displacements of a definite fraction of vanadium atoms. In the process, interstices with T_d local symmetry, which are most favorable for hydrogen atoms, are formed near the oxygen atoms. This result could also be important for interpreting the results of investigations of the vibrational spectrum of hydrogen in other ternary systems, for example, Ta–N–H and V–N–H, where the energy of the triply degenerate localized vibrations of the hydrogen atoms is $\varepsilon \approx 110$ meV.[12]

This work was supported by the Russian Fund for Fundamental Research, Project 95-02-04675-a, and the Russian State Program ''Topical Problems in Condensed Matter Physics'' in the subfield ''Neutron Investigations of Matter.''

[1] D. Klauder, V. Lottner, and H. Sheuer, Solid State Commun. **32**, 617 (1979).
[2] A. Magerl, J. J. Rush, and J. M. Rowe, Phys. Rev. B **33**, 2093 (1986).
[3] R. Hempelmann, D. Richter, and D. L. Price, Phys. Rev. Lett. **58**, 1016 (1987).
[4] E. Yagi, T. Kobayashi, Sh. Nakamura *et al.*, Phys. Rev. B **33**, 5121 (1986).
[5] K. Ozawa, S. Yamaguchi, Y. Fujino *et al.*, Nucl. Instrum. Methods **149**, 405 (1978).
[6] S. I. Morozov, V. V. Kazarnikov, N. G. Primakov *et al.*, in *Abstracts the National Conference on the Application of X-Rays, Synchrotron Radiation, Neutrons, and Electrons for Investigations of Materials, Dubna, 1997* [in Russian], JINR, Dubna, 1997, p. 341.
[7] V. A. Parfenov, P. S. Klemyshev, I. G. Morozov, and A. F. Pavlov, in Neutron Inelastic Scattering, Vol. 1, IAEA, Vienna, 1978, p. 81.
[8] K. Hiraga and M. Hirabayashi, J. Phys. Soc. Jpn. **34**, 965 (1973).
[9] S. I. Morozov, V. V. Sumin, A. V. Belushkin, and I. Natkanets, Fiz. Tverd. Tela (Leningrad) **27**, 2751 (1985) [Sov. Phys. Solid State **27**, 1652 (1985)].
[10] S. A. Danilkin, V. V. Sumin, and V. P. Minaev, Fiz. Tverd. Tela (Leningrad) **28**, 2843 (1986) [Sov. Phys. Solid State **28**, 1592 (1986)].
[11] N. F. M. Henry and K. Lonsdale (eds.), *International Tables for X-Ray Crystallography*, Vol. 1, Kynoch Press, Birmingham, England, 1952.
[12] S. I. Morozov, Physica B **234–236**, 32 (1997).

Translated by M. E. Alferieff

New line of thermodynamic phase transitions on the $x-T$ diagram of a dilute Heisenberg system with short-range interactions $Li_{0.5}Fe_{2.5-x}Ga_xO_4$

N. N. Efimova
Kharkov State University, 310077 Kharkov, Ukraine

(Submitted 19 January 1998)
Pis'ma Zh. Éksp. Teor. Fiz. **67**, No. 5, 329–333 (10 March 1998)

It is established on the basis of an investigation of the temperature dependences of the saturation magnetization $\sigma_S(T)$ and the magnetic contribution to the specific heat $C_m(T)$ that in the reentrant region of the $x-T$ diagram ($0.9 \leqslant x \leqslant 1.5$) of dilute iron spinels $Li_{0.5}Fe_{2.5-x}Ga_xO_4$ there exists between the line of Curie points $T_C(x)$ and the line of freezing temperatures $T_f(x)$ another line of first-order phase transitions $T_1(x)$ to a noncollinear ferrimagnetic phase: $T_C(x) \leqslant T_1(x) \leqslant T_f(x)$.
 [S0021-3640(98)00905-0]

PACS numbers: 75.40.Cx, 75.30.Et, 75.50.Lk, 64.70.Kb

According to current concepts, the $x-T$ phase diagram of Heisenberg systems with competing exchange contains two types of disordered states, specifically, a spin glass (SG) state and a mixed (FSG) state which precedes the SG in terms of concentration and where two types of long-range order coexist below the freezing temperature T_f — longitudinal ferro-, ferri-, or antiferromagnetic (FM, AFM), and transverse spin-glass.[1–3] As was shown by Gabay and Toulouse (G–T),[4] in this case the magnetic states replace one another in the following sequence as temperature is lowered: PM $\rightarrow$ FM $\rightarrow$ $M_1 \rightarrow$ M_2, where PM is the paramagnetic phase. The transformation FM $\rightarrow M_1$ is associated with freezing of the transverse spin components S_{xy}, and the transition $M_1 \rightarrow M_2$ appears in the form of a spontaneous breaking of the replica symmetry. For $H \neq 0$ this is recorded experimentally as the Almeida–Thouless (A–T) line $T_f(H)$.[1,2] The formation of the noncollinear state M_1 (freezing of S_{xy}) has also been observed by different experimental methods, but the line of the transition FM $\rightarrow$ M_1 $T_f(H)$ G–T has been observed only for a few objects.[1,2] Thus, for Heisenberg systems with long-range interactions the ''experimental'' transition FM $\rightarrow$ FSG corresponds to the theoretical transition $M_1 \rightarrow M_2$.

In Heisenberg systems with short-range interactions the transition FM $\rightarrow$ FSG has still not been given a theoretical explanation and a wide range of questions concerning the nature of the FSG states and the mechanisms leading to their formation is the subject of discussions.[1,2,5–9] As an example, in Ref. 5 an exchange mechanism, which gives rise to long-range transverse SG order, is proposed for dilute ferrimagnetic spinels. According to Ref. 5, a nonuniform FM state should precede the FSG state in terms of concentration ($T = 0$ K) or temperature ($T > T_f$) — a collinear in the macroscopic sense structure with local regions of noncollinearity (RLN) containing frustrated bonds. An effective long-

range interaction of the dipole type arises between the RLNs. This is what allows for the establishment of long-range interactions between S_{xy}. Later, in Ref. 8 the same mechanism of interaction of S_{xy} was obtained in a study of several models of Heisenberg systems. In Ref. 6 a scheme of transformations in terms of temperature, formally similar to the G–T scheme, was obtained by a numerical method: PM $\rightarrow$ FM $\rightarrow$ N $\rightarrow$ FSG. However, the transition into the noncollinear FM phase N is a second-order phase transition (PT-2) with respect to the noncollinearity parameter, while the formation of an FSG state as $T\rightarrow 0$ K occurs via a set of local first-order phase transitions (PT-1) due to '' melting'' of frustrated spins.

At the same time, Monte Carlo computer simulations consistently give negative results as to the possibility of existence of both thermodynamic (of the type FM$\rightarrow$ N) and spin-glass transitions in the region 0 K $<T<T_C$.[1,2,7] However, that finding contradicts the existing experimental data. Experimentally, both lines T_f, corresponding to the transitions PM $\rightarrow$ SG and FM $\rightarrow$ FSG, are clearly registered according to the same phenomenological indicators as in classical SGs.[1,2,10] The transition in a field occurs along the A–T line $T_f(H)$. This discrepancy could be due to the existence of anisotropy in real systems, as a result of which the Ising-type transition PM $\rightarrow$ SG at $T_f>0$ K also occurs.[11]

The objective of the present work was to study the mechanisms leading to the formation of the FSG states in dilute slightly-anisotropic two-sublattice spinels $Li_{0.5}Fe_{2.5-x}Ga_xO_4$. The lines of Curie points $T_C(x)$ and $T_f(x)$for the transitions FM $\rightarrow$ FSG ($0.9\leqslant x<1.5$) and PM $\rightarrow$ SG ($x>1.5$) were determined earlier,[10] so that attention is focused mainly on the analysis of the sequence and character of magnetic transformations in the region $T_f<T<T_C$. Of great interest is the question of the existence of a thermodynamic PT here. In this connection, the program of investigations included properties such as the temperature dependences of the spontaneous magnetization $\sigma_S(T)$ and the magnetic contribution to the specific heat $C_m(T)$. These quantities were determined using the same methods and experimental apparatus as in Refs. 9, 10, and 12. The polycrystalline samples were produce and certified by methods similar to those used earlier.[9]

Figure 1 shows the functions $\sigma_S(T)$ for samples with $x=1.45$ (*1*) and 1.40 (*2*), as determined by the kink-point method[13] using the dependences $\sigma_{FC}(T)$ in weak fields — $H<500$ Oe. As an illustration, Figure 1 shows a similar curve (*3*) for $x=1.45$ in the field $H=100$ Oe. One can see that for both Ga^{3+} concentrations a sharp decrease of σ_S is observed with decreasing temperature below some $T_1(x)>T_f(x)$ and the value of T_1 clearly increases with x. As $T\rightarrow 0$ K, the decrease in magnetization, starting at temperatures much higher than T_f, is observed both in the absence of a field ($x=1.35$, neutron-diffraction investigations) and in strong fields ($x\geqslant 1.2$), which destroy the FSG state and are higher than the technical saturation field.[10,14] This behavior of $\sigma_S(T)$ or $\sigma_H(T)$ can be caused only by the formation of a noncollinear FM structure — either macroscopic (H) or in the form of RLNs. The characteristic behavior of the temperature dependences $\sigma_S(T)$ (Fig. 1) suggests that both processes are realized: The plateau for $T_1<T<T_C$ is due to RLNs while the sharp decrease in $\sigma_S(T)$ for $T_f<T<T_1$ could reflect the existence of a PT-1.

To determine whether or not a PT-1 exists at temperatures $T_f<T<T_C$ the specific heat was investigated — the temperature dependences $C_m(T)$ for $H=0$. The result for

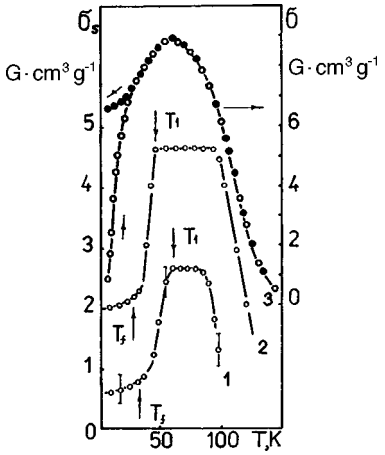

FIG. 1. Temperature dependences of the spontaneous magnetization $\sigma_S(T)$ for samples with $x=1.45$ (*1*) and 1.40 (*2*); (*3*) — temperature dependences of magnetizations $\sigma_{ZFC}(T)$ — ○ and $\sigma_{FC}(T)$ — ● for a sample with $x=1.45$ in the field $H=100$ Oe. *ZFC* — preliminary cooling of the sample from 300 to 4.2 K with $H=0$, *FC* — with $H=100$ Oe.

samples with $x=1.45$ and 1.2 are presented in Fig. 2. The typical SG behavior is observed at low temperatures: $C_m \sim T$ at temperatures $T<T_f$. For $x=1.45$ there is a clear anomaly at $T\sim 100$ K, characteristic for PT-2 at T_C. For $x=1.2$ the temperature interval is bounded by 60 K, since according to the preceding discussion the value of T_1 should be less than 60 K, while $T_C=325$ K. In the intermediate region $T_f<T<T_C$ the curves $C_m(T)$ are very irregular, especially for $x=1.2$. This irregularity (the existence of several diffuse maxima) can be explained on the basis of the model of Ref. 5, which assumes the existence of RLNs at temperatures $T_f<T<T_C$. This is discussed in detail in Refs. 15 and 16.

The most interesting result is the anomaly observed at $T\approx 60$ K for $x=1.45$. Its form — a very sharp spike below 1 K — is typical for a PT-1.[17] This correlates quite well with the behavior of $\sigma_S(T)$ (Fig. 1), if T_1 is taken as the temperature of the PT-1 (see above).

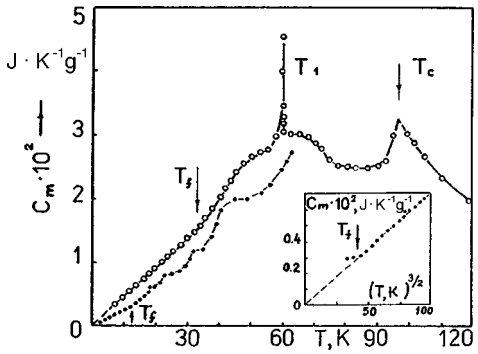

FIG. 2. Temperature dependences of the magnetic part of the specific heat $C_m(T)$ with $H=0$ for samples with $x=1.45$ (○) and 1.2 (●). Inset: $C_m(T^{3/2})$ for a sample with $x=1.2$.

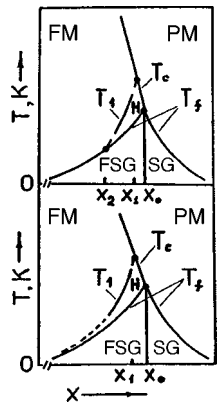

FIG. 3. Schematic form of the $x-T$ diagrams of Li–Ga spinels taking account of the line $T_1(x)$ of first-order phase transitions between macroscopic collinear (FM) and noncollinear (N) ferrimagnetic states.

One other fact merits attention. The temperature at which the PT-1 is observed (Fig. 2) equals, to within the experimental accuracy, the temperature corresponding to the maximum on the curves of the low-field magnetization $\sigma_H(T)$ (Fig. 1). Below the temperature of the maximum not only σ_{ZFC} but also σ_{FC} decrease rapidly and the typical SG irreversibility ($\sigma_{ZFC}(T) \neq \sigma_{FC}(T)$) is observed only for $T \leqslant T_f(H)$, and $\sigma_{FC}(T)$ decreases comparatively weakly as $T \to 0$ K.

It can be concluded on the basis of the results presented in Figs. 1 and 2 that for samples with $x = 1.45$ and 1.40 a thermodynamic PT-1 of the order–order type exists at temperature $T_1(x)$ in the temperature range $T_f < T < T_C$. Therefore the following transformations as functions of temperature occur in this concentration range of the $x-T$ diagram with decreasing temperature: PM$\to$ collinear FM ($T \leqslant T_C$)$\to$ nonuniform FM (presence of RLN) $\to$ noncollinear FM (phase N)$\to$ FSG. PT-2 and PT-1 thermodynamic transitions occur at $T = T_C(x)$ and $T = T_1(x)$, respectively, while a spin-glass transition occurs at $T = T_f(x)$. Judging from the data in Fig. 1, the magnitude of the effect at T_1 (jump in σ_S) decreases for $x > 1.4$. This is also observed for $x < 1.4$. Specifically, for the sample with $x = 1.3$ the question of the existence of a PT-1 in the region $T_f < T < T_C$ can probably be solved only by investigating $C_m(T)$, since weak jump-like changes in σ_S are virtually impossible to observe by the kink method.

The results obtained for $x = 1.45$ and 1.40 attest to the fact that besides the lines $T_C(x)$ and $T_f(x)$[9] one other line of first-order phase transitions — $T_1(x)$ should be present in the phase diagram of Li–Ga spinels. The form of such a phase diagram is shown schematically in Fig. 3. It is obvious that the line $T_1(x)$ intersects $T_C(x)$ in the concentration interval $1.45 < x < x_0$, since for $x > x_0 = 1.5$ the long-range FM order is absent for all $T \geqslant 4.2$ K.[10] This signifies that, besides a multicritical point $x = x_0$, the phase diagram also contains a tricritical point $x_1 < x_0$, where PM and FM phases and the noncollinear phase N coexist. At lower Ga^{3+} concentrations, $0.9 \leqslant x \leqslant 1.3$, two possibilities exist. In the first place, the PT-1 line $T_1(x)$ can intersect the line $T_f(x)$ at the next tricritical point x_2, where the phases FSG, FM, and N coexist (Fig. 3a). Another possible variant is an asymptotic approach of the line $T_1(x)$ to $T_f(x)$ with decreasing x and both lines simultaneously approaching $T = 0$ K asymptotically, which is predicted for $T_f(x)$.[1,2]

In this situation the above-described scheme of magnetic transformations in terms of temperature is realized in the entire concentration range of the FSG states, and the phase diagram corresponds to Fig. 3b. Considering the preliminary data, it cannot be ruled out that for the concentration interval $x=0.9-1.2$ a PT-1 can indeed exist either near T_f or directly at $T=T_f$, as was observed for the highly anisotropic Li–Ga spinel with $x=0.9$ and Co^{2+} additions (~ 1.7 mole %).[9] The point is that for samples with $x=0.9-1.2$ a change in the behavior of $C_m(T)$ is observed in the temperature interval $T \geqslant T_f$: The dependence $C_m \sim T$ is replaced by the spin-wave law $C_m \sim T^{2/3}$ (Fig. 2, inset ($x=1.2$)). The temperature extent of the spin-wave section is wider for $0.9 \leqslant x < 1.2$ than for $x=1.2$.[15]

Both phase diagrams in Fig. 3 can be explained in principle by invoking the exchange mechanism.[5,8] However, it is entirely possible that the form of the $x-T$ diagram is determined not only by exchange but also by anisotropy. In the first place, as we have said, in Heisenberg systems with short-range interactions the exchange mechanism of formation of the SG states can be realized only in the presence of anisotropy.[1,2,11] In the second place, anisotropy can play a substantial role in the formation of noncollinear FM structures (for ferrimagnets see, for example, Refs. 18 and 19), determining their specific type, regions of existence in terms of temperature and the field H, and finally the character of the PT at T_1, which in sum also determines the line $T_1(x)$.

In conclusion, it should be noted that the results obtained in the present work for the particular case of Li–Ga spinels apparently reflect some general trends characteristic of Heisenberg systems with short-range interactions. In this connection it is of fundamental importance to determine more accurately the form of the $x-T$ phase diagrams, including for SG systems distinguished by anisotropy. Such investigations for Li–Ga spinels are in progress.

I am extremely grateful to N. V. Tkachenko, V. A. Pervakov, and A. G. Anders for providing assistance and support in conducting the experimental investigations.

[1] K. Binder and A. P. Yuang, Rev. Mod. Phys. **58**, 801 (1986).
[2] I. Ya. Korenblit and E. F. Shender, Usp. Fiz. Nauk **157,** 267 (1989) [Sov. Phys. Usp. **32**, 139 (1989)].
[3] D. Chowdhury, T. M. Harders, A. Mookerjee *et al.*, Solid State Commun. **57**, 603 (1986).
[4] M. Gabay and G. Toulouse, Phys. Rev. Lett. **47**, 201 (1981).
[5] J. Villain, Z. Phys. B **33**, 31 (1979).
[6] W. M. Saslow and G. N. Parker, Phys. Rev. Lett. **56**, 1074 (1986).
[7] J. R. Thomson, Hong Guo, D. H. Ryan *et al.*, Phys. Rev. B **45**, 3129 (1992).
[8] G. N. Parker and W. M. Saslow, Phys. Rev. B **38**, 11718, 11733 (1988).
[9] N. N. Efimova, Yu. A. Popkov, and S. R. Kufterina, JETP Lett. **64**, 450 (1996).
[10] N. N. Efimova, Yu. A. Popkov, and N. V. Tkachenko, Zh. Éksp. Teor. Fiz. **90,** 1413 (1986) [Sov. Phys. JETP **63**, 827 (1986)]; *ibid.* **97**, 1208 (1990) [**70**, 678 (1990)]; Fiz. Nizk. Temp. **14,** 981 (1988) [Sov. J. Low Temp. Phys. **14**, 539 (1988)]; *ibid.* **15,** 1055 (1989) [**15**, 584 (1989)]; *ibid.* **16,** 1565 (1990) [**16**, 881 (1990)].
[11] B. W. Morris, S. G. Colborne, M. A. Moore *et al.*, J. Phys. C **19**, 1157 (1986).
[12] N. N. Efimova, V. A. Pervakov, V. I. Ovcharenko *et al.*, Fiz. Tverd. Tela **35,** 2838 (1993) (St. Petersburg) [Phys. Solid State **35**, 1405 (1993)].
[13] W. Abdul-Razag, J. S. Kouvel, and A. Clans, Phys. Rev. B **30**, 6480 (1984).
[14] N. N. Efimova, Yu. A Popkov, and G. A. Takzeĭ, Fiz. Tverd. Tela (St. Petersburg) **36,** 490 (1994) [Phys. Solid State **36**, 271 (1994)].
[15] N. N. Efimova, Zh. Éksp. Teor. Fiz. **113**, 1339 (1998) (in press).

[16] N. N. Efimova, Yu. A. Popkov, S. R. Kufterina *et al.*, Fiz. Nizk. Temp. **20,** 546 (1994) [Low Temp. Phys. **20**, 431 (1994)].
[17] W. V. Johnston, H. Wiedersich, and G. W. Lindberg, J. Chem. Phys. **51**, 3739 (1969).
[18] De. M. F. Bertant, CR Acad. Sci. **250,** 85 (1960); **252,** 76, 252 (1961).
[19] B. Boucher, R. Buhl, and M. Perrin, Phys. Chem. Sol. **31,** 2251 (1970).

Translated by M. E. Alferieff

Near-IR laser inelastic electronic light scattering spectroscopy on transitions between ground and excited states of acceptor centers in GaAs and InP crystals

B. Kh. Baĭramov,[a] B. P. Zakharchenya, and V. V. Toporov
A. F. Ioffe Physicotechnical Institute, Russian Academy of Sciences, 194021 St. Petersburg, Russia

(Submitted 21 January 1998)
Pis'ma Zh. Éksp. Teor. Fiz. **67**, No. 5, 334–339 (10 March 1998)

We report the development of a method for recording the low-temperature ($T=6$ K) near-IR inelastic light scattering spectra and the observation of electronic scattering on the transitions $1s_{3/2}(\Gamma_8) \rightarrow 2s_{3/2}(\Gamma_8)$ between the ground and excited states of different shallow acceptor centers in a n-type semi-insulating crystal si-GaAs ($n=1.0\times10^8$ cm^{-3}) and in a doped p-InP crystal ($p=3.6\times10^{17}$ cm^{-3}). Moreover, a new line, associated with the transition $1s_{3/2}(\Gamma_8) \rightarrow 2p_{3/2}(\Gamma_8)$ and due to a dielectric local mode, recorded for the first time in the spectra of narrow-gap semiconductors, was found in the residual-frequency band in the p-InP spectrum between TO(Γ) and LO (Γ) phonons. © *1998 American Institute of Physics.* [S0021-3640(98)01005-6]

PACS numbers: 78.35.+c, 71.55.Eq

In semiconductor crystals the presence of dopants with density higher than $\sim1\times10^{18}$ atoms/cm^3 and masses different from the masses of the host atoms results in the formation of local vibrational modes whose frequencies differ from those of normal lattice vibrations. Such local modes have been investigated quite intensively according to the lattice IR-absorption spectra. However, such spectra are sensitive only to dopants which are much lighter than the host elements (for example, carbon in GaAs).[1,2] At the same time, the spectrum of lattice vibrations in polar crystals can be quite strongly perturbed near impurity centers on account of the electron–phonon interaction, and so-called dielectric local modes (DLMs) can form under favorable conditions. Their appearance is due completely to the resonance interaction of an impurity electron and an optical phonon, when the energy difference for intracenter transitions between the ground and excited states with different parity (for transitions of the type $1s-2p$) is close to the energy of a longitudinal optical phonon.[3–7] Such spatially localized bound states have nothing in common with the conventional mechanism leading to the appearance of the above-mentioned local vibrational modes.

As is well known, valuable information about impurity states in semiconductors can be obtained by laser inelastic electronic light scattering spectroscopy, which makes it possible to investigate the range of quite low concentrations. Although a great deal of

attention has always been devoted to these investigations in doped materials and their different steps are reflected in many reviews and monographs,[5,8–11] a number of questions have still not been adequately studied. For example, previous investigations of inelastic light scattering by an electron–hole gas and by free electrons and their collective electron–phonon excitations (plasmon-phonon bound states) were mainly limited to measurements performed in the region of strong absorption of the experimental crystals. The energies of the exciting photons was $\hbar\omega_i \geqslant E_0$ and close to resonances with the fundamental absorption edge E_0 or the gap $E_0+\Delta_0$, where Δ_0 is the spin–orbit interaction energy. The excitation conditions are also chosen so as to be in resonance with high-lying energy levels near the critical points of the combined density of states (of the type E_1) or with different excitonic size-quantization levels in low-dimensional structures. Such excitation conditions provide, as a rule, a substantial resonance increase of the scattering intensity and, one would think, should make it much easier to detect the weak light fluxes of inelastic electronic scattering of light. However, effects due to spatial dispersion arise in such a resonance method of excitation. Additional contributions to the electronic scattering of light, which are associated with interband and intraband transitions, appear. Aside from this, a hot-luminescence background appears even in low-temperature measurements on doped samples. These circumstances greatly complicate the problem of obtaining inelastic electronic light scattering spectra at low frequencies, which is the most interesting region. Moreover, as a result of the additional generation of nonequilibrium carriers, they do not make it possible to establish quantitative laws. Problems of this type can be partially overcome by means of nonresonance excitation.

The development of a method for recording quasielastic electronic light scattering spectra in the near-IR region of the spectrum with $\hbar\omega_i \leqslant E_0$ was reported earlier.[9] Investigations performed on doped n-type semiconductors GaAs and InP with a nonparabolic dispersion law of the bands made it possible to study the basic laws of the fluctuations of the electron gas, such as fluctuations of the number, charge, and spin densities of the current carriers as well as fluctuations of the electron momentum and energy.[12] Different mechanisms of manifestation of electron–electron and electron–phonon interactions were distinguished. They were manifested in quasielastic light scattering, both in the collisionless regime for specially not doped ($n<1\times10^{15}$ cm^{-3}) and lightly doped ($n\sim1\times10^{16}$ cm^{-3}) samples and under conditions of frequent collisions in heavily doped samples with $n>1\times10^{16}$ cm^{-3} and on up to 1×10^{19} cm^{-3} (Ref. 10).

In the present letter we report a further elaboration of the method presented in Ref. 9 for recording the inelastic electronic light scattering spectra in the near-IR region of the spectrum. The experimental data obtained attest to the observation of electronic light scattering due to $1s_{3/2}(\Gamma_8)\rightarrow 2s_{3/2}(\Gamma_8)$ transitions between the ground and lowest excited states of different shallow acceptor centers in the spectra of nominally undoped semi-insulating n-type si-GaAs and doped p-InP crystals. Moreover, a new band associated with the transition $1s_{3/2}(\Gamma_8)\rightarrow 2p_{3/2}(\Gamma_8)$ and due to a DLM recorded in the spectra of such narrow-gap semiconductors was found in the spectra of p-InP crystals in the residual-frequency band between the transverse TO(Γ) and longitudinal LO(Γ) optical phonons.

Dielectric local modes were discovered previously in III–V semiconductor crystals with a zinc-blende lattice and studied in detail in the inelastic light scattering spectra of wide-gap semiconductors n-GaP doped with different donor impurities.[5–7,13] For p-type

crystals with a complicated valence band structure it was noted that quasielastic light scattering by spin density fluctuations arises even in zeroth-order in the **k**–**p** method of perturbation theory, which neglects the corrections to wave functions that contain the nonparabolicity of the spectrum.[11] For this reason, in these materials quasielastic light scattering by free holes is characterized by more complicated features and is much stronger than any form of quasielastic electron scattering of light in n-type materials.[11,12,14] This situation also makes it difficult to observe experimentally the inelastic hole light scattering spectra due to transitions between the ground and excited states of the same parity ($1s-2s$ type transitions) of shallow acceptor centers. The detection of DLM spectra due to transitions of the type $1s-2p$ and hole light scattering spectra due to transitions of the type $1s-2s$ in narrow-gap materials is of great interest, because then it would be possible to determine the corrections to the eigenenergies of an impurity center, which fall outside the framework of the effective-mass approximation.

Our experiments were performed on well-characterized samples. Undoped ultrapure semi-insulating n-type si-GaAs samples with free carrier density $n=1.0\times10^8$ cm^{-3} at $T=300$ K were investigated. Doped p-GaAs:C samples with $p=1.5\times10^{17}$ cm^{-3} (at $T=300$ K) and p-GaAs:Zn with $p=3.0\times10^{17}$ cm^{-3} ($T=300$ K) were also investigated. Furthermore, doped samples of p-InP with $p=3.6\times10^{17}$ cm^{-3} and mobility $\mu=150$ cm^2/V·s ($T=300$ K) and no identified impurity content were investigated. All samples were grown by the Czochralski method. For the si-GaAs sample the concentration of neutral EL2 defects, determined according to the near-IR absorption spectra, was equal to 3.0×10^{15} cm^{-3}. In doped samples the free charge-carrier densities were determined from Hall effect measurements as well as by independent measurements of the spectra of quasielastic light scattering by free carriers and inelastic light scattering by bound states of longitudinal optical phonons and plasma oscillations. Homogeneous samples of high optical quality were cut out along the crystallographic directions $[100]\parallel x$ axis, $[011]\parallel y$ axis, and $[0\bar{1}1]\parallel z$ axis for si-GaAs and in the directions $[\bar{1}11]\parallel x'$ axis, $[1\bar{1}0]\parallel y'$ axis, and $[11\bar{2}]\parallel z'$ axis for all other samples. Their shape was that of a parallelepiped with dimensions $\sim0.5\times2.5\times3$ mm.

The spectra in the transmission region of the experimental samples were excited with a highly stable neodymium-doped yttrium aluminum garnet laser with wavelength 1064.4 nm. Scattering by an angle of 90° for parallel $[z(yy)x]$ and crossed $[(x'(y'z')z']$ polarizations of the incident (first index in parentheses) and scattered (second index in parentheses) light was investigated; the first index in front of (after) the parentheses indicates the direction of the incident (scattered) light. The spectral composition of the scattered light was analyzed with a high-transmission ($f=1:3$) double diffraction spectrometer. The spectral resolution was equal to 2 cm^{-1}. All measurements were performed at lattice temperature $T=6$ K and at quite low power densities of the exciting radiation $P=8-10$ W·cm^{-2}, which do not cause local heating of the samples.

It is interesting to note that under the conditions of our experiment the frequency factor R^2 of resonance intensification of the scattering, where $R\approx E_g^2/[E_g^2-(\hbar\omega_i)^2]$, was equal to 5.9 for GaAs with $E_g=1.519$ eV and 9.2 for InP with $E_g=1.424$ eV. Compared with interband excitation in the visible region of the spectrum (where $\hbar\omega_i\geqslant E_0$), such an intensification likewise partially compensated the unavoidable losses in connection with the detection of light scattering spectra in the near-IR region.

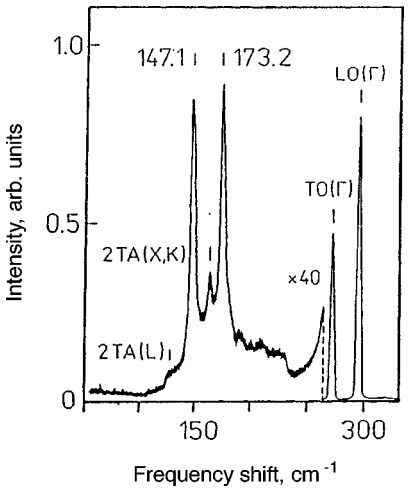

FIG. 1. Fragment of an inelastic light scattering spectrum for *si*-GaAs with $n=1.0\times10^{8}$ cm^{-3}. The spectrum was obtained at $T=6$ K in the scattering geometry $z(yy)x$.

Figure 1 shows the inelastic light scattering spectrum for *si*-GaAs. Here, the quite intense lines at 271.3 and 294.5 cm^{-1} are due to scattering of light by TO(Γ) and LO(Γ) phonons, respectively.

Sharp and strong lines are clearly seen at 147.2 and 173.3 cm^{-1} against the background of comparatively weak lines corresponding to overtone lattice scattering, of which the strongest line corresponds to scattering with participation of two acoustic 2TA(X,K) phonons. Their absolute intensity drops rapidly with increasing temperature, and they completely vanish in the spectra obtained at $T=60$–70 K. The frequencies of these lines agree well with our data, which were obtained under similar conditions but in the spectra of the two other doped samples *p*-GaAs:C with $p=1.5\times10^{17}$ cm^{-3} and *p*-GaAs:Zn with $p=3.0\times10^{17}$ cm^{-3}. It is important to note that the frequencies which we observed also agree well with the data of Ref. 2, where a similar line was observed at 148 and 174 cm^{-1} and also in the spectra of two different samples doped with carbon and zinc, respectively. The appearance of such lines, associated with acceptor transitions in *n*-type *si*-GaAs indicates optical charge transfer on the acceptor centers. At low temperatures the low density of residual acceptor impurities in such a sample was completely compensated by shallow donors and deep donor EL2 centers. Photoexcited electrons and holes are generated when IR radiation is absorbed. Such electrons can be trapped by ionized acceptor centers, and neutralization of the latter can thus occur. As a result, these lines can be attributed to electronic scattering due to intracenter transitions between the ground and lowest excited states of two different shallow acceptor centers — transitions of the type $1s_{3/2}(\Gamma_8)\rightarrow 2s_{3/2}(\Gamma_8)$ for impurity carbon and zinc atoms, respectively.

An entirely different picture was observed for *p*-InP crystals. Figure 2 shows a typical fragment of a spectrum of such scattering for a zinc-doped *p*-InP sample with $p=3.6\times10^{17}$ cm^{-3}.

The most intense and narrow line at 305.9 cm^{-1} corresponds to TO(Γ) phonons.[10] The wider line at 348 cm^{-1} is due to scattering of light by high-frequency bound state

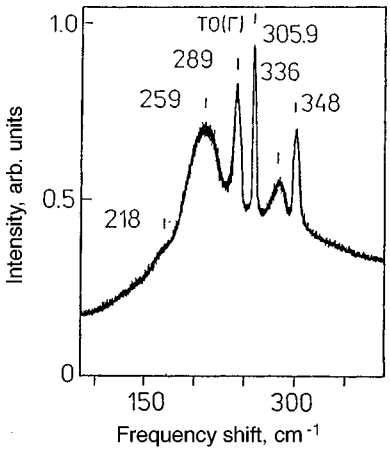

FIG. 2. Fragment of near-IR inelastic light scattering spectrum for p-InP:Zn with $p=3.6\times10^{17}$ cm^{-3}. The spectrum was obtained at $T=6$ K in the scattering geometry $x'(y'z')z'$.

L_+, formed by LO(Γ) phonons and optical plasmons of the two-component hole plasma of the gas of free light and heavy holes. Such states are formed as a result of a resonance interaction of the macroscopic longitudinal electric fields of these oscillations. Such bound states in InP crystals were studied earlier in the inelastic light scattering and IR reflection spectra but in n-type samples.[10] In the present case, despite the short relaxation times of free holes, $\tau\leqslant 20$ fs, for which the effective plasma dampings of the holes reach values $\Gamma\geqslant 200$ cm^{-1}, it is surprising to observe a quite narrow line of the plasmon–phonon bound state with almost purely phonon damping, while the low-frequency mode L_- is not observed. This behavior was predicted earlier theoretically for a strongly damped plasma with large carrier effective masses, when the mechanism of the deformation potential and the electrooptic effect make the main contribution to light scattering.[14]

It should be noted that lines corresponding to TO(Γ) phonons and the L_+ mode are present in the room-temperature spectra also. At the same time, the new structures observed at 218, 259, 289, and 336 cm^{-1} in the rest of this spectrum appear only with decreasing temperature. This indicates that they are of electronic (hole) origin.

We attribute the quite wide and intense band at 259 cm^{-1} (32.11 meV) to a transition $1s_{3/2}(\Gamma_8)\rightarrow 2s_{3/2}(\Gamma_8)$ between the ground and excited states of the Zn impurity. As already noted above, such transitions between levels with the same parity are active in the light scattering process. The energy shift found for this transition agrees well with the value 32.8 meV determined from data on selective photoluminescence of donor-acceptor pairs in InP at $T=4.2$ K.[15] A sharp shoulder at 218 cm^{-1} (27.02 meV) arises from the low-frequency side of this band. It can be attributed to the transition $1s_{3/2}(\Gamma_8)$ $\rightarrow 2s_{3/2}(\Gamma_8)$ between the carbon impurity levels.

The observation of a quite narrow and intense line at 289 cm^{-1} (35.83 meV) was completely unexpected. We also attribute this line to the transition $1s_{3/2}(\Gamma_8)$ $\rightarrow 2s_{3/2}(\Gamma_8)$ but this time between cadmium levels. We note that in Ref. 15 similar

transitions for C and Cd were determined as 27.5 and 36.1 meV, respectively; this likewise agrees well with our results.

A new fact is that the line observed at 336 cm^{-1} lies in the residual-frequency band between TO(Γ) and LO(Γ) phonons. For $\hbar\omega_i \leqslant E_0$ only one case with such a characteristic behavior is known. It is due to the formation of a DLM. It is noteworthy that the DLM is formed by the Zn acceptor center which we have already identified. But, as estimates show, the transition $1s_{3/2}(\Gamma_8) \rightarrow 2p_{3/2}(\Gamma_8)$ with energy 30.5 meV could contribute to the formation of such a DLM.[15] In addition, according to the selection rules, such a transition between levels with different parity is not active directly in the light scattering process. It should be noted that all the energies which we have measured for transitions between the ground and excited states for the characteristic levels of acceptor transitions have a direct bearing on the magnitude of the corrections to the computed values obtained in the effective-mass approximation with allowance for the potential of the central cell.

In conclusion, we note that the practical implementation of the possibility of measuring near-IR inelastic electronic light scattering spectra due to the transitions $1s_{3/2}(\Gamma_8) \rightarrow 2s_{3/2}(\Gamma_8)$ between the ground and lowest excited states of different shallow acceptor impurities an also the observation of DLMs associated with transitions of the type $1s_{3/2}(\Gamma_8) \rightarrow 2p_{3/2}(\Gamma_8)$ open up new possibilities for determining the corrections to the energy eigenvalues obtained in the effective-mass approximation as well as for developing new analytical methods for identifying the chemical type of the residual (background) impurities and dopants in semiconductor materials.

[a)]e-mail: bairamov@bahish.ioffe.rssi.ru

[1] E. E. Haller, in *Defect and Impurity Engineered Semiconductors and Devices*, edited by S. Ashok, J. Chevallier, I. Akasaki *et al.*, Mater. Res. Soc. Pittsburgh, 1995, p. 547.
[2] J. Wagner, Appl. Surf. Sci. **50**, 79 (1991).
[3] Sh. M. Kogan and R. A. Suris, Zh. Éksp. Teor. Fiz. **50**, 1279 (1966) [Sov. Phys. JETP **23**, 850 (1966)].
[4] I. B. Levinson and É. I. Rashba, Usp. Fiz. Nauk **111**, 683 (1973) [Sov. Phys. Usp. **16**, 892 (1974)].
[5] M. V. Klein, in *Light Scattering in Solids* [Russian translation], edited by M. Cardona, Mir, Moscow, 1979, p. 174.
[6] B. Kh. Baĭramov, G. Irmer, J. Monecke, and V. V. Toporov, JETP Lett. **41**, 428 (1985).
[7] J. Monecke, G. Irmer, B. H. Bairamov *et al.*, Phys. Status Solidi B **138**, 685 (1986); **142**, 237 (1987).
[8] E. Burnstein, M. Cardona, D. J. Lockwood *et al.*, in *NATO ASI, B: Physics*, Vol. 273, edited by D. J. Lockwood and J. Young, Plenum, New York, 1991.
[9] B. Kh. Baĭramov, V. A. Voĭtenko, and I. P. Ipatova, Usp. Fiz. Nauk **163**, 67 (1993) [Phys. Usp. **36**, 392 (1993)].
[10] B. H. Bairamov, V. A. Voitenko, and I. P. Ipatova, Phys. Rep. **229**, (1993).
[11] B. Kh. Baĭramov, V. A. Voĭtenko, I. P. Ipatova *et al.*, Fiz. Tekh. Poluprovodn. **28**, 913 (1994) [Semiconductors **28**, 531 (1994)].
[12] B. H. Bairamov, V. A. Voitenko, I. P. Ipatova *et al.*, Phys. Rev. B **50**, 14923 (1994).
[13] P. Galtier and G. Martinez, Phys. Rev. B **38**, 10542 (1988).
[14] B. H. Bairamov, V. V. Toporov, N. V. Agrinskaya *et al.*, Phys. Status Solidi B **146**, K161 (1988).
[15] P. J. Dean, D. J. Robbins, and S. G. Bishop, Solid State Commun. **32**, 379 (1979).

Translated by M. E. Alferieff

Undamped self-oscillations and dynamical chaos under conditions of impurity breakdown of a semiconductor in the fixed-current regime

Z. S. Kachlishvili and K. M. Jandieri
Department of Physics, Tbilisi State University, 380028 Tbilisi, Republic of Georgia

(Submitted 26 January 1998)
Pis'ma Zh. Éksp. Teor. Fiz. **67**, No. 5, 340–343 (10 March 1998)

It is shown theoretically that chaotic oscillations of the Hall field, the Hall constant, and the magnetoresistance appear in a compensated semiconductor under impurity breakdown conditions. It is shown that the transition to chaos occurs via the Feigenbaum scenario. © *1998 American Institute of Physics.* [S0021-3640(98)01105-0]

PACS numbers: 72.20.My, 61.72.−y

Recent experimental and theoretical investigations have shown that impurity electric breakdown opens up extensive possibilities for observing nonlinear behavior in semiconductor systems.[1–4] The character of the nonlinear dynamics depends on different external and internal parameters of the system. One of the most important such parameter is the magnetic field. For this reason it is of interest to determine the conditions that promote the appearance of undamped, including chaotic, oscillations in a semiconductor in the presence of a magnetic field.

Let us examine a *n*-type compensated semiconductor connected in series with a load resistance R and a dc battery with emf $\mathcal{E}$. A nonquantizing magnetic field H is applied perpendicular to the electric field. The problem is studied in the fixed-current regime (the fixed-field regime was investigated in Ref. 5).

A new approach is proposed for describing the nonlinear dynamics of hot electrons. The basic idea is to study the dielectric relaxation of the applied (E_x) and Hall (E_y) fields (both processes determine the dielectric relaxation of the total, warming field E). The corresponding mathematical model is given by the equations

$$\frac{dn}{dt} = -a(z)n^2 + b(z)n + d, \tag{1}$$

$$\frac{dE_x}{dt} = \frac{4\pi L}{\varepsilon SR}\left[\zeta - E_x - \frac{eSR}{L}(\mu_1(Z)E_x + \mu_2(z)E_y)\right], \tag{2}$$

$$\frac{dE_y}{dt} = \frac{4\pi e}{\varepsilon} n[\mu_2(z)E_x - \mu_1(z)E_y], \tag{3}$$

$$\frac{dZ}{dt} = -\frac{Z - Z_0(E)}{\tau_d}. \tag{4}$$

Here

$$a(z)=A_I(z)+B_T(z), \quad b(z)=-G-B_T N_d C+A_I N_d(1-C),$$

$$d=GN_d(1-C), \quad G=j\sigma+A_T, \quad \zeta=\mathcal{E}/L,$$

n is the free-electron density, A_I and B_T are the impact ionization and thermal recombination coefficients, and $j\sigma$ and A_T are the optical and thermal generation rates from donor levels, S is the transverse cross section of the sample, L is the length of the sample in the direction of E_x, ε is the permittivity of the sample, and μ_1 and μ_2 are the longitudinal and transverse mobilities.

The equation (1) describes generation-recombination processes from shallow donor levels with density N_d for degree of compensation $C=N_A/N_d$ (N_A is the density of compensating acceptors), while Eq. (4) describes the lag of the dimensionless electron temperature $Z=T_e/T$ (T is the lattice temperature) relative to a change in E, τ_d is the delay time, and the stationary value $Z=Z_0(E)$ for each value of E is determined from the energy balance equation.

It can be easily verified from Eqs. (2) and (3) for $L/SR \ll \sigma_1$, where $\sigma_1=en\mu_1$, that the characteristic relaxation times of E_x and E_y are of the same order of magnitude $\tau_1 \sim \varepsilon/4\pi\sigma_1$. When the reverse inequality holds, the relaxation of the Hall field is once again characterized by the time τ_1, while the relaxation of the applied field is characterized by the time $\tau_2 \sim \varepsilon SR/4\pi L \equiv \overline{C}R$, where $\overline{C}$ is the capacitance due to the accumulation of charge on the main contacts of the sample, and in addition $\tau_2 \ll \tau_1$, i.e., E_x relaxes much more quickly than E_y. We note that even in this case the lag time of the electron temperature (τ_d) is much shorter than the relaxation time of n, E_x, and E_y. For this reason it can be assumed to a high degree of accuracy that as E varies, the value $Z=Z_0(E)$ is established instantaneously, i. e. the equations (1)–(3) are sufficient for studying the dynamics of a system of hot electrons. Therefore a problem in three-dimensional phase space obtains.

Let us consider the case of strong magnetic fields $\omega_c^2\tau^2 \gg 1$, where ω_c is the cyclotron frequency and τ is the momentum relaxation time. Application of bifurcation theory on the basis of the Routh–Hurwitz condition gives a necessary and sufficient condition for the appearance of undamped self-oscillations in a semiconductor

$$\frac{A_I}{C}\frac{1}{E/E_B-1} > \frac{\beta}{H^2}\frac{(2+\alpha m)(1+\alpha m+1/\gamma^2)}{1/\gamma^2-(1+\alpha m+a/W\mu_1)}. \tag{5}$$

Here $\alpha=E\cdot Z_0'(E)/Z$, $m=Z\cdot\mu_1'(z)/\mu_1$, $\gamma=\mu_1/\mu_2$, $W=4\pi e/\varepsilon$, and $\beta=H^2W\mu_1$ (for $\omega_c^2\tau^2 \gg 1$ we have $\mu_1 \sim 1/H^2$, and β does not depend on H).

All values are taken at the breakdown point, except for the value of E in the denominator on the left-hand side of Eq. (5); E_B is the intensity of the breakdown field. Primes denote derivatives of the corresponding quantities.

As one can see from Eq. (5), the condition for the appearance of undamped oscillations is satisfied all the better, the closer E is to the breakdown point. A strong magnetic field and domination of the momentum scattering by impurity ions likewise make it easier to satisfy the condition (5).

Since for $\omega_c^2\tau^2 \gg 1$

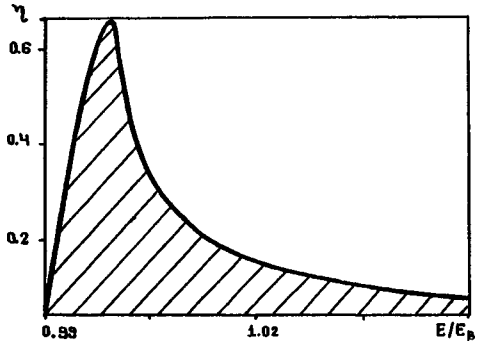

FIG. 1. Bifurcation diagram in the $(E/E_B, \eta)$ plane.

$$\gamma \approx \frac{32}{9\pi}\frac{1}{\omega_c\tau}, \quad \frac{1}{\omega_c\tau}, \quad \frac{32}{3\pi}\frac{1}{\omega_c\tau}$$

in the cases of momentum scattering by acoustic phonons, neutral impurity atoms, and ionized impurity atoms, respectively, the condition $\gamma \ll 1$ is quite realistic. In this case the condition (5) assumes the much simpler form

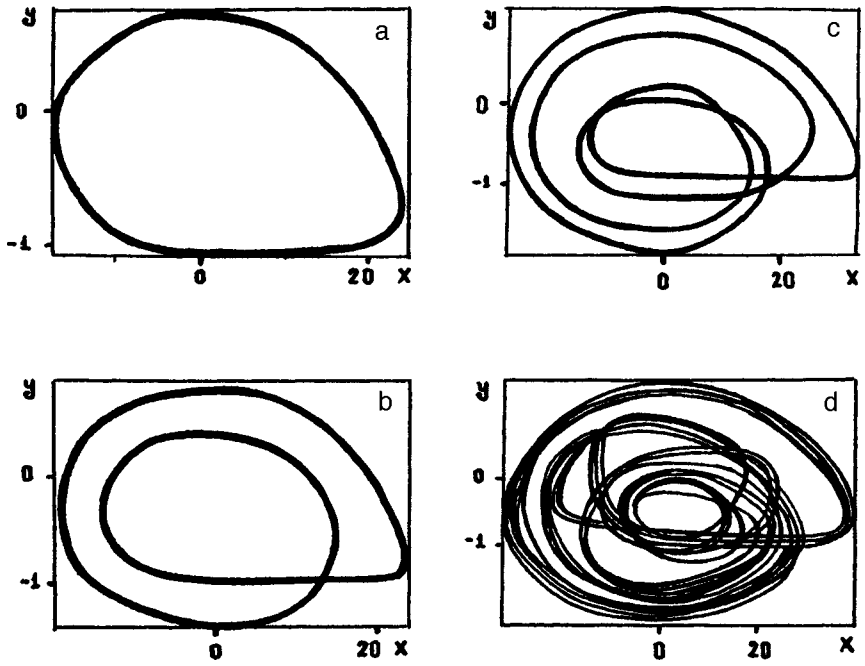

FIG. 2. Phase portraits of the system in the (x,y) plane for different values of η: a) 0.04, b) 0.034, c) 0.028, and d) 0.02.

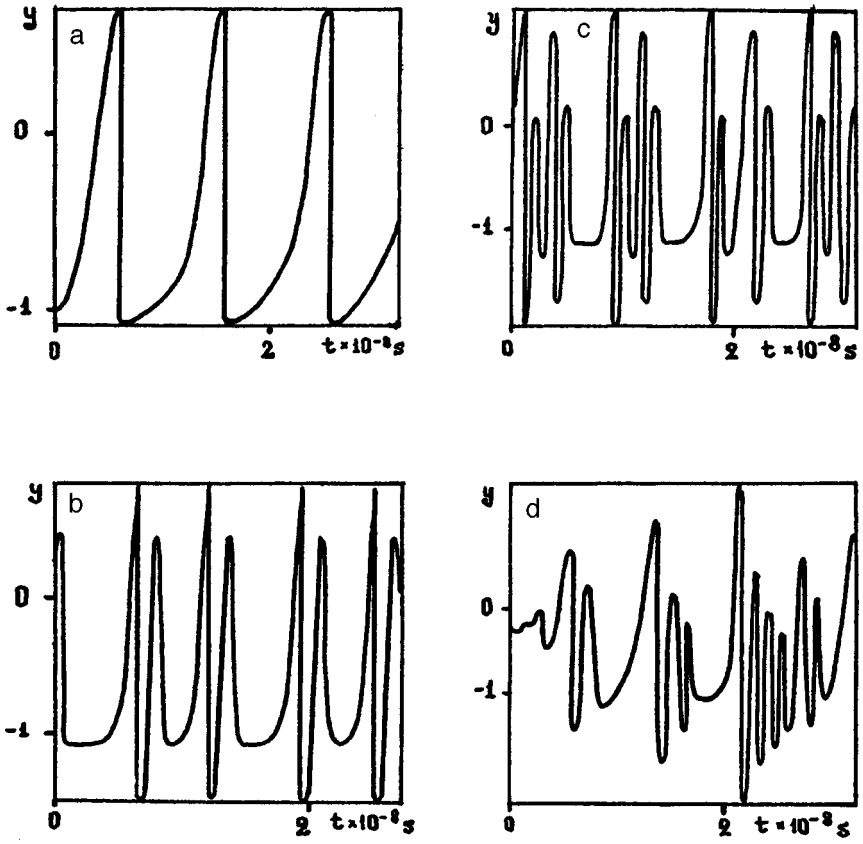

FIG. 3. Oscillations of y for the same values of η as in Fig. 2.

$$\frac{A_I}{C}\frac{1}{E/E_B-1}>\frac{\beta}{H^2}(2+\alpha m). \tag{6}$$

Figure 1 shows the bifurcation diagram in the plane $(E/E_B,\eta)$, where $\eta=E_x/(\zeta-E_x)$ plays the role of the bifurcation parameter. This diagram was obtained by numerical calculations for n-Ge with the following parameters: $N_d=10^{16}$ cm^{-3}, $C=0.95$, $H=5\times10^4$ G, and $G=10^3$ s^{-1}. The energy balance equation takes into account energy losses on acoustic phonons (the corresponding rate is given by the well-known Shockley formula) as well as losses to excitation and ionization of impurity ions.[6] The hatched region in the diagram corresponds to saddle–focus type points of equilibrium, i.e., to undamped self-oscillations in the system. Oscillations of the Hall field, magnetoresistance, and Hall constant were studied in this region. Varying the value of η from 0.04 down to 0.02 with fixed $E/E_B=1.009$ ($E_B=834.21$ V/cm), we obtain a transition to chaos via period doubling, as is characteristic of the Feigenbaum scenario. Figure 2 shows the corresponding phase portraits in the (x,y) plane, where $x=(E_x-E_x^*)/E_x^*$ and $y=(E_y-E_y^*)/E_y^*$ (E_x^* and E_y^* are the equilibrium values of E_x and E_y) for the same values of the nonbifurcational parameters as in Fig. 1, while Fig. 3 displays as an example the corresponding

temporal evolution of the Hall field.

In closing, I express my appreciation to I. P. Zvyagin for his interest in this work and for a discussion of the results.

[1] K. Yamada, N. Takara, H. Imada *et al.*, Solid-State Electron. **31**, 809 (1988).
[2] D. G. Seiler, C. L. Littler, R. J. Justice, and P. W. Milonni, Phys. Lett. A **108**, 462 (1985).
[3] Y. Abe, Solid-State Electron. **31**, 795 (1988).
[4] A. Brandl, T. Geisel, and W. Prettl, Europhys. Lett. **3**(4) (1990).
[5] K. M. Jandieri and Z. S. Kachlishvili, Pis'ma Zh. Tekh. Fiz. **23**, 16 (1997) [Tech. Phys. Lett. **23**, 643 (1997)].
[6] Z. S. Kachlishvili, Phys. Status Solidi B **48**, 65 (1971).

Translated by M. E. Alferieff

Electronic phase separation in a low-temperature tetragonal phase of lanthanum–strontium cuprates according to ^{139}La NQR data

G. B. Teĭtel'baum and E. L. Vavilova
Physicotechnical Institute, Russian Academy of Sciences, 420029 Kazan, Russia

B. Buechner
Universitaet zu Köln, D-50937 Köln, Germany

H. Luetgemeier[a)]
Forschungszentrum Jülich, D-52425 Jülich, Germany

(Submitted 19 November 1997; resubmitted 26 January 1998)
Pis'ma Zh. Éksp. Teor. Fiz. **67**, No. 5, 344–349 (10 March 1998)

A nonuniform electron density distribution is observed in $La_{1-x-y}Nd_ySr_xCuO_4$ and $La_{1-x-y}Eu_ySr_xCuO_4$, and long-lived magnetic fluctuations in these compounds are studied. The dynamics of the magnetic fluctuations depends strongly on the magnetic properties of the rare-earth ions, which stabilize the low-temperature tetragonal phase. © *1998 American Institute of Physics.*
[S0021-3640(98)01205-5]

PACS numbers: 75.60.Ch, 75.50.Ee, 72.80.Sk, 76.60.Gv

The question of the correlated spatial separation of charges and spins has been under animated discussion in recent years in connection with the observation of antiferromagnetic stripe domains (''stripes'') separated by domain walls.[1–3] These walls are regions where current carriers collect as a result of frustrated electronic phase separation.[4] Weighty experimental evidence supporting the idea that in lanthanum cuprates the stability of such a spatially modulated structure is due to a transition from a low-temperature orthorhombic (LTO) phase to a low-temperature tetragonal (LTT) phase. The point is that in this case the potential relief of the lattice possesses nonuniformities such that the current carriers pinned by them form linear chains.

Unfortunately, at present the separation of charges and spins has been reliably observed experimentally in only one high-T_c superconducting compound $La_{1.6-x}Nd_{0.4}Sr_xCuO_4$. This is largely due to the fact that neutron scattering is a direct method for performing such investigations, and in addition on single-crystal samples. However, despite the fact that an entire series of compounds in which the LTT phase is realized has been synthesized by replacing Nd with other rare-earth ions, it has been possible to grow single crystals of only one of them, the one investigated in Refs. 1 and 2.

For this reason, a complete physical picture of such charge and spin structures does not exist, despite the exceptional interest shown in the problem of electronic phase

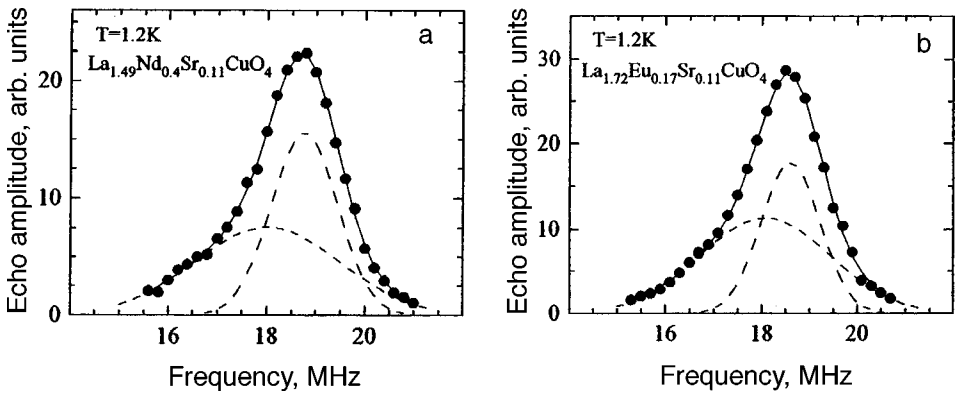

FIG. 1. ^{139}La NQR spectra of the transition $\pm 5/2 - \pm 7/2$ at temperature 1.2 K for the compounds $La_{1.48}Nd_{0.4}Sr_{0.12}CuO_4$ (a) and $La_{1.72}Eu_{0.17}Sr_{0.11}CuO_4$ (b). Solid lines — result fitting the line by a sum of two contributions with different frequencies (dashed lines).

separation. In light of the difficulties noted above, an effective method for studying charge and spin structures could be the application of local methods of investigation, first and foremost, nuclear quadrupole resonance (NQR), which does not require an external field, fixing a distinguished direction, and for which the difference between the polycrystalline and single-crystalline samples plays no role. Moreover, since the NQR frequency is determined by the gradient of the crystalline electric field, this method makes it possible to record directly nonuniformities in the charge distribution in electronic phase separation problems.[5–7]

The main problem of the present work was to make a NQR investigation of electronic phase separation in lanthanum–strontium compounds, where the appearance of a LTT phase was stabilized by doping with different rare-earth ions: magnetic Nd ions or nonmagnetic Eu ions.

1. Two series of samples $La_{2-x-y}Nd_ySr_xCuO_4$ and $La_{2-x-y}Eu_ySr_xCuO_4$ with different x and y were prepared by the standard technology.[8] The NQR measurements were performed on a standard pulsed spectrometer in the temperature range 1.2–25 K. The NQR spectra of ^{139}La nuclei were obtained by measuring the amplitudes of the echo accompanying a successive change in the frequency in a zero external magnetic field.

We begin our discussion of the results with the series $La_{1.88-y}Nd_ySr_{0.12}CuO_4$. Special attention is devoted here to the case when the neodymium content $y=0.4$, since antiferromagnetic (AF) antiphase domains separated by charged domain walls have been observed in this compound.[1,2] Our ^{139}La NQR measurements in this compound showed that at sufficiently low temperatures asymmetric lines (the first one is shown in Fig. 1a) are observed for the transitions $\pm 7/2 - \pm 5/2$ and $\pm 5/2 - \pm 3/2$ and their widths are proportional to the corresponding quadrupole frequencies. This shows that the broadening is due to a nonuniform distribution of quadrupole frequencies. It is entirely natural to represent the observed asymmetric signal as a superposition of two Gaussian lines which have different widths and NQR frequencies (see Fig. 1a). We attribute the presence of two contributions to the fact that the La nuclei can be located both near a localized hole, which distorts the crystalline field, and far away from it, which is reflected in the local

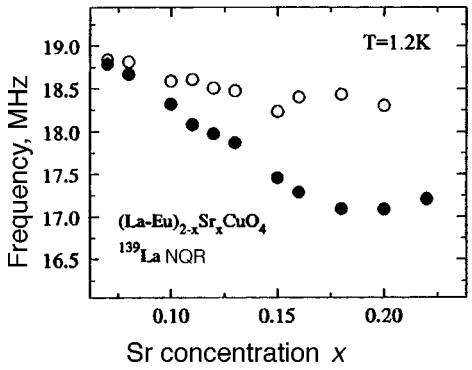

FIG. 2. ^{139}La NQR frequencies of the transition $\pm 5/2 - \pm 7/2$ versus Sr content (x) for two components of the spectrum of $La_{1.83-x}Eu_{0.17}Sr_xCuO_4$ at temperature 1.2 K.

variation of the properties of NQR. The extremal values of the frequencies make the main contribution to the observed signal. For this reason, in accordance with the well-known dependence of quadrupole resonance frequency of ^{139}La on the carrier density in lanthanum cuprates,[9–11] the component corresponding to the higher frequency can be referred to carrier-depleted regions (regions with developed AF correlations). The low-frequency component, however, can be referred to regions with high carrier density (charged domain walls). The signals referring to AF regions have a smaller width (1–1.5 MHz), while the width of the signals from domain walls, which differ by large nonuniformities of the electric field gradient, is of the order of 3.5 MHz.

A combined analysis of the NQR signals corresponding to the high-frequency (7/2–5/2) and low-frequency (5/2–3/2) transitions made it possible to determine the quadrupole splitting parameter ν_Q (it is related with the electric field gradient V_{zz} as $\nu_Q = eQV_{zz}/14$, where e is the electron charge, and Q is the quadrupole moment of the nucleus) and the asymmetry parameter η. For lanthanum nuclei located in regions with no holes we have $\nu_Q \simeq 6.28$ and $\eta \simeq 0.15$, while for nuclei located in regions with holes $-\nu_Q \simeq 6.112$ and $\eta \simeq 0.3$.

Let us now discuss the series $La_{1.83-x}Eu_{0.17}Sr_xCuO_4$ with different strontium content x (it is known[8] that with respect to its effect on the transition to the LTT phase the substitution $y = 0.17$ for Eu is equivalent to $y = 0.40$ for Nd). The LTT phase arising at some temperatures $T(x) < T_{\max} = 130$ K completely or partially suppresses superconductivity.[8] Specifically, for our Eu concentration the superconducting transition edge is displaced into the region of high values $x = x_c = 0.16$ (the critical temperatures of samples with $x = 0.16$, 0.18, 0.20, and 0.22 were equal to 22.6, 29, 25.6, and 22 K). The transition to the LTT phase, starting at $x \simeq 0.07$, is reflected in the behavior of all three possible NQR lines. For example, starting with strontium concentration $x = 0.07$, the lines corresponding to the high-frequency transitions $\pm 7/2 - \pm 5/2$, just as in the case of La–Nd compounds, have an asymmetric shape, which evolves with increasing x, right up to $x = x_c = 0.16$. The corresponding signal can be represented as a superposition of two lines: a wider (low-frequency) line and a narrower (high-frequency) line (Fig. 1b). The magnitude of the splitting appearing at $x = 0.07$ increases with the number of holes in the system (see Fig. 2), starting at $x = 0.07$ right up to $x = 0.16$, corresponding to a transition

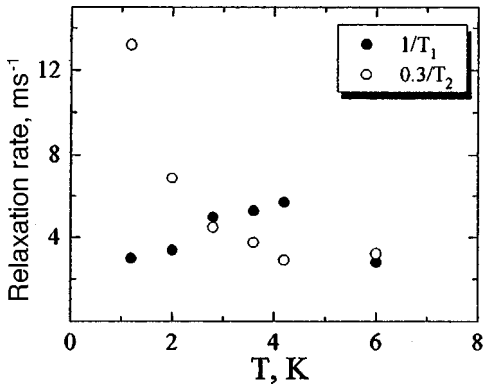

FIG. 3. Temperature dependence of the longitudinal (●) and transverse (○) relaxation rates of ^{139}La nuclei in $La_{1.48}Nd_{0.4}Sr_{0.12}CuO_4$.

to the superconducting state. We note that the relative intensity of these two components, which characterizes the fractions of the lightly doped (high-frequency) and heavily doped (low-frequency) phases, depends strongly on x. At first, the contribution of the high-frequency line increases with x, reaching a maximum at $x=0.12$, and then decreases, vanishing at a complete transition of the system to the superconducting state, occurring at $x=0.22$.

It can be assumed that the corresponding difference of electric field gradients is due to nonuniformities (modulation) of the electron density distribution in the system. Moreover, the fact that this distribution appears in the observed NQR line shows that it is stationary on a time scale of the order of the reciprocal of the frequency difference between the two components of the NQR spectrum.

These results support previous hypotheses[1–4] that similar stripe structures exist in undoped lanthanum–strontium compounds (which do not undergo a transition to the LTT phase but are located near this transition), the only difference being that the structures are mobile formations. According to Refs. 1–4, they could be one-dimensional hole clusters, separating regions with high hole density (it has not been ruled out that the regions also have AF order), and as shown in Ref. 12, their dynamics reduce to motion in a perpendicular field. We note that the velocity of the charged domain walls can be determined from the frequency of the magnetic fluctuations.

2. Let us now examine the relaxation of ^{139}La nuclei. We note first that in the Nd compound the characteristic rates are two orders of magnitude higher than in the Eu compound. This shows unequivocally that the magnetic moments of Nd play a role in this process (we observed acceleration of relaxation when the Nd content increased from 0 to 0.4). They determine the main relaxation channel which has the nonexponential character typical for relaxation via randomly distributed magnetic moments.[13] The temperature dependence of the effective relaxation times (Fig. 3), expressed for $T_1 \gg T_2$ in the form

$$1/T_{1,2}=(\gamma_n H_i^{\perp,\parallel})^2\{\tau/[1+(\omega_Q\tau)^2],\tau\},$$

makes it possible to estimate the lifetime of the fluctuations. Here $H_i^{\perp}$ and $H_i^{\parallel}$ are the average absolute values of the perpendicular and parallel components of the internal

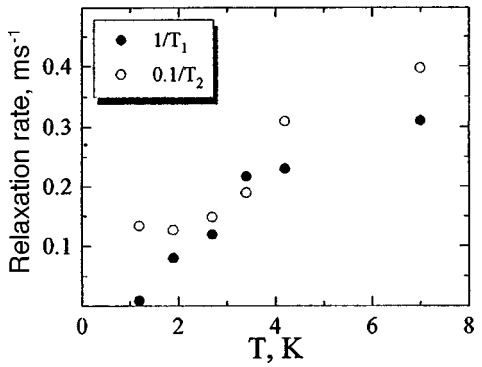

FIG. 4. Temperature dependence of the longitudinal (●) and transverse (○) relaxation rates of ^{139}La nuclei in $La_{1.72}Eu_{0.17}Sr_{0.11}CuO_4$.

fluctuation field produced by the Nd moments at the La nuclei, τ is the lifetime of the corresponding fluctuations, and γ_n is the gyromagnetic ratio for La nuclei. Our estimates of τ_{Nd} at the point $\omega_Q\tau_{Nd}=1$ (corresponding to max $1/T_1$) give $\tau_{Nd}\sim 0.8\times 10^{-8}$. Taking account of the measured relaxation rate, this means that Nd produces at the La nuclei a magnetic field of the order of 330 Oe. This value indicates that the field is of dipole origin.

We now turn to relaxation in La–Eu (Fig. 4). For a sufficiently low Sr content, both $1/T_1$ and $1/T_2$ are determined by nonexponential relaxation via local magnetic moments (coupled with holes) and have the same temperature dependence. Such a dependence, reducing to an almost x-independent slowing down of the longitudinal relaxation with decreasing temperature, remains for any value of x. However, as x increases, an additional channel appears in the transverse relaxation (under conditions with a developed LTT phase), and this channel dominates at low temperatures near $x=1/8$. The relaxation times associated with it are of the order of 1 ms. This critical contribution to relaxation is due to an increase in the antiferromagnetic correlation of magnetic moments of copper, which leads to freezing of the local moments on the one hand and to slowing down of critical fluctuations on the other. The fact that the critical AF fluctuations are manifested only in transverse relaxation suggests that they are related only with the component of the field that is longitudinal relative to the quantization axis. It has not been ruled out that it arises as a result of the so-called canting, i.e., the copper magnetic moments tilting out the plane as a result of the Dzyaloshinskiĭ–Moriya interaction owing to the inclinations of CuO_6 octahedra characteristic for the LTT phase. Estimates made taking into account the observed[14] decrease of the frequency of AF fluctuations to 10^{11} s^{-1} give for an average fluctuating magnetic field of 2800 Oe.

We call attention to the fact that acceleration of transverse relaxation indicates a substantial increase in the ferromagnetic correlation length ζ_{AF} in the La–Eu compound (this fact was also pointed out in Ref. 14). It has not been ruled out that under conditions when this quantity is greater than the distance between domain walls in-phase domains can appear in the system (in these domains the orientation of neighboring magnetic moments separated by the wall is the same; this is different from the situation in the La–Nd system, where, according to Refs. 1 and 2, they are antiparallel). In this case

domain motion is impeded[12,15] and suppression of superconductivity is more effective.

3. In summary, our analysis has shown that for both systems investigated a nonuniform distribution of charge density, which is of a stationary character on scales of the order of 10^{-5}–10^{-6} s, exists in the LTT phase. The characteristic lifetimes of the magnetic fluctuations for these compounds are substantially different. In the case of doping with Nd ions, the magnetic fluctuations slow down as a result of adjustment to the ordered magnetic moments of Nd and have a characteristic lifetime of 10^{-8} s. In the system doped with nonmagnetic Eu ions, however, the lifetime of the fluctuations, even the fluctuations undergoing critical slowing down, is much shorter (10^{-10}–10^{-11} s). Therefore it can be concluded that charge ordering is decoupled from spin ordering, and in addition the magnetic fluctuations depend on the properties of the ions stabilizing the LTT phase.

We acknowledge helpful discussions with N. N. Garif'yanov, V. E. Kataev, and M. Piper. This work was performed as part of the Joint Russian-German program ''Spectroscopy of High-T_c Superconductors'' and it is also support by Grant 95-02-05942 from the Russian Fund for Fundamental Research.

[a)]Deceased.

[1] J. M. Tranquada, B. J. Sternlieb, J. D. Axe *et al.*, Nature **375**, 561 (1995).
[2] J. M. Tranquada, J. D. Axe, N. Ichikawa *et al.*, Phys. Rev. B **54**, 7489 (1996).
[3] D. Poilblanc and T. M. Rice, Phys. Rev. B **39**, 9749 (1989); J. Zaanen and O. Gunnarson, Phys. Rev. B **40**, 7391 (1989).
[4] V. J. Emery, S. A. Kivelson, and H-Q. Lin, Phys. Rev. Lett. **64**, 475 (1990); V. J. Emery and S. A. Kivelson, Physica C **209**, 597 (1993).
[5] P. C. Hammel, A. P. Reyes, E. T. Ahrens *et al.*, in *Proceedings of the International Conference on Strongly Correlated Systems*, San Diego, Calif., 1993.
[6] G. B. Teitel'baum, B. Buechner, H. Luetgemeier *et al.*, J. Low Temp. Phys. **105**, 407 (1996).
[7] M. A. Teplov, Yu. A. Sakhratov, A. V. Dooglav *et al.*, JETP Lett. **65**, 821 (1997).
[8] B. Buechner, M. Braden, M. Cramm *et al.*, Physica C **185–189**, 903 (1991); B. Buechner, M. Cramm, M. Braden *et al.*, Europhys. Lett. **21**, 953 (1993).
[9] T. Kobayashi, S. Wada, Y. Kitaoka *et al.*, J. Phys. Soc. Jpn. **58**, 779 (1989).
[10] S. Ohshugi, Y. Kitaoka, H. Yamanaka *et al.*, J. Phys. Soc. Jpn. **63**, 2057 (1994).
[11] E. F. Kukovitsky, H. Luetgemeier, and G. B. Teitel'baum, Physica C **252**, 160 (1995).
[12] A. H. Castro Neto, http://xxx.lanl.gov/abs/cond-mat/9611146.
[13] M. R. McHenry, B. G. Silbernagel, and J. H. Wernick, Phys. Rev. B **5**, 2958 (1972).
[14] V. E. Kataev, B. Rameev, B. Buechner *et al.*, J. Low Temp. Phys. **105**, 449 (1996); Phys. Rev. B **55**, R3394 (1997).
[15] Yu. A. Krotov, D.-H. Lee, and A. V. Balatsky, Phys. Rev. B **56**, 8367 (1997).

Translated by M. E. Alferieff

d-Symmetry superconductivity as a consequence of valence-bond type correlations

A. A. Ovchinnikov, M. Ya. Ovchinnikova, and E. A. Plekhanov
Institute of Chemical Physics, Russian Academy of Sciences, 117977 Moscow, Russia

(Submitted 27 January 1998)
Pis'ma Zh. Éksp. Teor. Fiz. **67**, No. 5, 350–355 (10 March 1998)

It is shown that $d_{x^2-y^2}$ symmetry of superconducting order due to valence bond (VB) type correlations is possible. The VB correlations are compatible with antiferromagnetic (AF) spin order. For the two-dimensional Hubbard model with arbitrary doping, the variational method of local unitary transformations is used to construct explicitly a uniform state with VB structure. The *d*-channel attraction of holes is a consequence of the modulation of hops by the populations of centers accompanying VB formation, and the parameters of the modulation are determined variationally. The increase in the density of states at the Fermi level accompanying AF splitting of the band, which is absent in the paramagnetic state, is important for the gap width. The gap width and its ratio to T_c are of the order of $2\Delta \simeq 0.1t$ and $2\Delta/kT_c \simeq 4-4.5$ with $U/t \simeq 8$. The agreement between the phase diagram found and experiment is discussed. © *1998 American Institute of Physics.* [S0021-3640(98)01305-X]

PACS numbers: 74.20.−z, 74.25.Jb

In recent years high-resolution methods in photoemission spectroscopy,[1] neutron scattering, and others have greatly enriched knowledge of the electronic structure of high-T_c superconductors. The band approach, serving as a natural language for discussing these experiments, should include correlations and should take account of all types of correlations, which on the basis of analysis in the localized limit $U \to \infty$ or from the numerical calculations of finite clusters are expected to play a large role. All theoretical works seek answers to the most important questions — the possible correlation nature of attraction and the pairing mechanism and the role of antiferromagnetic (AF) correlations and valence bond (VB) formation type correlations (see Ref. 2 and the reviews Refs. 3–5).

In the present letter we investigate the same questions on the basis of a variational approach and an explicit representation of the correlated state for the purpose of determining the role of individual types of correlations, specifically, VB type. Hole attraction is often attributed to an interaction of the correlated (or modulated) hops type, as noted in Ref. 6. In contrast to Ref. 6 or analogous interactions in the $t-J$ model,[5] in the present letter the form and magnitude of interactions of this type are determined from the variational principle by solving the appropriate self-consistent problem.

The analysis is conducted in the basic classical model of strongly correlated systems — the two-dimensional model with Hamiltonian $H(U,t)$.

The resonating valence bond (RVB) states introduced by Anderson[7] signified that the configurations of the system consist of singlet components of two particles which are localized on the sites forming the bond. Later,[8–10] variational functions — itinerant analogs of states with a regular periodic VB structure and uniform VB states[10] — were constructed for the Hubbard model and their properties were investigated. In these solutions, in contrast to RVB, the formation of a singlet pair is accompanied by a change (optimization) of the charge state of the sites forming the bond. Questions concerning superconducting (SC) order were not investigated. At the same time, in contrast to the nonunitary transformations of the type in Gutzwiller's ansatz,[11] the method of local unitary transformations proposed in Refs. 9 and 10 makes it possible to construct not only a correlated function but also an explicit expression for the effective Hamiltonian and therefore to study the possibility of SC order with $d_{x^2-y^2}$ symmetry. This symmetry can be regarded as proven for a number of cuprates (BiBaCaCuO, YBaCuO) on the basis of many experiments done by different methods. For this reason, and also on account of the fact that on-site repulsion suppresses s-symmetry SC order but does not influence d-type SC correlation, we shall study only the latter.

The wave function Ψ with VB-type correlations can be constructed from an uncorrelated state Φ by means of a unitary transformation

$$\Psi=\hat{W}(\alpha)\Phi, \quad \hat{W}(\alpha)=\exp(\alpha Z), \quad Z=\sum_{\langle nm\rangle} Z_{nm}. \tag{1}$$

The local anti-Hermitian operator Z_{nm}, referring to the $\langle nm\rangle$ bond of nearest-neighbor sites, equals

$$Z_{nm}=-\frac{1}{2}\sum_{\sigma} j_{nm\sigma}\Delta_{nm,-\sigma}, \tag{2}$$

$$j_{nm\sigma}=c^{\dagger}_{n\sigma}c_{m\sigma}-c^{\dagger}_{m\sigma}c_{n\sigma}, \quad \Delta_{nm,-\sigma}=n_{n-\sigma}-n_{m-\sigma}. \tag{3}$$

The operator Z_{nm} acts only on the singlet components with two particles in neighboring sites in the wave function Φ. For one dimer $\{a,b\}$ the operator $W_{ab}=\exp(Z_{ab})$ performs a rotation of the two-hole singlet components of the bond, and its action on the uncorrelated singlet function $\Phi(a,b)$ gives an exact singlet state of a dimer with the optimal parameter $\alpha=\alpha(U,t)$.

On account of the fact that the transformation in Eq. (1) is unitary the initial Hubbard Hamiltonian in the basis of correlated states Ψ is strictly equivalent to the transformed Hamiltonian

$$\tilde{H}(\alpha)=W^{\dagger}(\alpha)HW(\alpha) \tag{4}$$

in the basis of the functions Φ. The variational parameter α in $W(\alpha)$ serves as an order parameter for VB structures. Analyzing the new problem (4) by the mean-field method makes it possible to investigate states with VB-type correlations and arbitrary doping.

In contrast to previously studied periodic VB structures with nonoverlapping dimers,[9] in the case of a uniform VB state (1) the local operators Z_{nm} do not commute with one another. But, we can find an explicit expression for $\tilde{H}(\alpha)$ in terms of the Fermi operators up to terms $\sim\alpha^2$ inclusive.

$$\tilde{H}(\alpha)\approx H+\alpha[H,Z]+\frac{\alpha^2}{2}[[H,Z],Z]=H^{(0)}+\alpha H^{(1)}+\frac{\alpha^2}{2}H^{(2)} \tag{5}$$

and then find the self-consistent solution of the new problem by the mean-field method. The expression for $\tilde{H}(\alpha)$ will be given in Ref. 12.

To test the possibility of AF spin order and $d_{x^2-y^2}$-type superconducting order let us investigate the most general class of uncorrelated states of the BCS type with anomalous *d*-symmetry averages and with a double magnetic unit cell. For the function Φ of such a general form the average energy $\overline{H}(y_i)=\langle\Psi H\Psi\rangle=\langle\Phi\tilde{H}\Phi\rangle$ can be calculated exactly for the operator (5). It turns out to be a function of the following single-electron normal and anomalous averages over Φ:

$$\{y_i\}=\{r_0,r_1,r_{\sqrt{2}},r_2,r_{\sqrt{5}},r_3,d_0,d_{\sqrt{2}},d_2,w_1,w_2,w_{\sqrt{5}},w_3\}_i, \tag{6}$$

where

$$r_l=\frac{1}{2}\sum_\sigma\langle c^\dagger_{n\sigma}c_{n+l,\sigma}\rangle_\Phi;$$

$$d_l=\frac{1}{2}\sum_\sigma\frac{\sigma}{|\sigma|}(-1)^n\langle c^\dagger_{n\sigma}c_{n+l,\sigma}\rangle_\Phi; \tag{7}$$

$$w_l=\text{sign}(l_x^2-l_y^2)\langle c^\dagger_{n\uparrow}c^\dagger_{n+l,\downarrow}\rangle_\Phi=w_l^*.$$

On account of symmetry the quantities r_l, d_l, and w_l are real and depend only on $|l|$.

We shall discuss only the leading terms in the effective Hamiltonian $\tilde{H}$, which are responsible for SC pairing. Thus, in the term which is of first order in α in Eq. (5) the contribution to $\alpha H^{(1)}$ from an on-site interaction has the form

$$\alpha H_U^{(1)}=-\alpha\frac{U}{2}\sum_\sigma\sum_{\langle nm\rangle}[c^\dagger_{n\sigma}c_{m\sigma}(n_{n,-\sigma}+n_{m,-\sigma})-2c^\dagger_{n\sigma}c_{m\sigma}n_{n,-\sigma}n_{m,-\sigma}+\text{h.c.}]. \tag{8}$$

The first term in the summation in Eq. (8) describes the interaction of correlated hops, which was proposed by Hirsch[6] and others. It can describe only *s*-type superconductivity, which is strictly forbidden in our system by the on-site repulsion $\sim U$. Only the average of the second term in Eq. (8) contains a contribution, of interest to us, from the *d*-symmetry SC order parameter with a negative superconducting pairing constant. This contribution per site equals

$$\langle\Delta H^{\text{SC}}\rangle=k_{11}|w_1|^2,\quad k_{11}=-8\alpha U r_1<0. \tag{9}$$

Here we have written only the determining contribution. In reality, all contributions to $\langle\overline{H}\rangle$ with anomalous averages w_i were collected together. This decreases the absolute

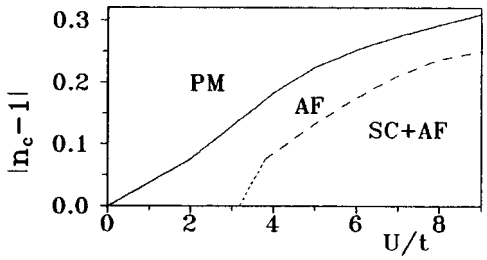

FIG. 1. Phase diagram for solutions with VB correlations in the plane of interaction force versus doping. Solid curve — critical degree of doping at which antiferromagnetism vanishes. Dashed curve — boundary of existence of the anisotropic superconducting gap, calculated at temperature $kT=0.002t$; the initial part of the curve is drawn schematically because of the ultralow values of the gap widths and the poor convergence near T_c.

value of k_{11} but preserves the negative sign of the leading constant for both the AF+VB states and the paramagnetic (PM)+VB state, making possible the superconducting pairing.

The uncorrelated function Φ minimizing the energy $\overline{H}-\mu\overline{N}$ is an eigenfunction of the linearized Hamiltonian

$$H_L=\sum_\nu \frac{\partial\overline{H}}{\partial y_\nu}(\hat{y}_\nu-y_\nu)+\overline{H}(y_i). \tag{10}$$

Here $\hat{y}_i$ are two-fermion operators corresponding to the averages y_i.[12] The single-electron averages y_i in turn can be expressed in terms of the characteristics and populations of the single-particle eigenstates of the linear operator (10). This closes the self-consistency procedure. Subsequent minimization with respect to α gives the desired correlated variational state (1) and the optimal effective Hamiltonian (5) in the basis of uncorrelated states. Two types of self-consistent calculations which agree with one another were performed: 1) a complete calculation with all normal and anomalous averages, giving the SC gap $2\Delta_0(U,\delta,T)$ for the AF+VB+SC states and 2) calculation from equations which are linear in w_l of the SC transition temperature $T_c(U,\delta)$ against the background of AF+VB states. The dependences of Δ and T_c on the degree of doping $\delta=|n-1|$ were studied.

Comparing the energies for PM or AF mean-field solutions with or without correlations of the VB type showed that the main gain in energy is provided by the magnetic doubling of the lattice via spin alternation as well as by VB formation. Taking account of AF and VB correlations gives good agreement with the computational results for finite clusters. The value of the optimal parameter α characterizing VB formation varies in the range $0<\alpha<0.22$ for $0<U/t\leqslant 8$, which makes it possible to use the expansion (5) right up to $U/t\sim 8$. Correlations of the VB formation type are compatible with AF spin order. Taking them into account narrows the region of existence of AF order.

Figure 1 displays the phase diagram of the system in the U/t, $\delta=|n-1|$ plane (the interaction force is the degree of doping). The critical doping level $\delta_c=|n_c-1|$, at which AF order vanishes, is $\delta_c\sim 0.3$ for $U/t=8$. These values are lower than the corresponding

result $\delta_c \sim 0.45$ in the generalized Hartree–Fock method neglecting VB-type correlations, but they exceed the critical degree of doping $\delta_c \sim 0.05$, which destroys antiferromagnetism in real high-T_c superconductor crystals.

The contradiction indicated above can be interpreted in different ways. One interpretation is to assume that the large region of AF order is a consequence of neglecting in the initial Hubbard model interactions which destroy perfect nesting. At the same time, the existence of a hopping interaction t' of non-nearest neighbors in cuprates follows both from the details of the single-band mapping[13] of the three-band Emery model and from the empirical tight-binding models. However, for small t' the AF–PM boundary does not shift much.

One would think that the mean-field method (in the present case this method was applied to the effective Hamiltonian $\tilde{H}(\alpha)$) is not capable of describing AF correlation of spins with a large but finite correlation length. At the same time, in the slave-boson technique two phases of the spin arrangement are seen before the transition to the paramagnetic state — with short- or long-range AF order (so-called SRO phase).[14] In addition, the total boundary of the true PM state is very close to $\delta_c(U)$ in Fig. 1. There also exist independent arguments in favor of a large region of AF spin order of separate CuO_2 planes in contrast to the observed small region of bulk antiferromagnetism (see, for example, Refs. 15 and 16).

We shall now discuss superconductivity. A region where solutions with superconducting order have the lowest energies is indicated in the same U/t, δ diagram in Fig. 1. The region where d-type superconductivity exists lies completely inside the region of ''two-dimensional'' antiferromagnetism. Hole attraction is due to not exchange of long-wavelength AF spin excitations, as assumed in many works,[17] but rather the formation of valence bonds between neighboring sites. It occurs both for the AF+VB states and for energetically unfavorable PM+VB states: The leading constant k_{11} in Eq. (8) is negative for each of these types of states. Nonetheless, a quite wide region of doping, where d-superconductivity with a quite high transition temperature exists, is present only in the AF+VB state because of the difference in the density of states at the Fermi level.

Figure 2 displays curves of the superconducting transition temperature $T_c(\delta)$ (appearance of anomalous averages w_l against the background of the normal AF+VB or PM+VB states). The values of T_c equal the temperature at which the SC gap $2\Delta(T)$ and the anomalous averages in the complete calculation AF+VB+SC vanishes. The region of a sharp cutoff of T_c lies below the boundary $\delta_c(U/t)$ between the AF+VB and PM+VB states in Fig. 1. At the same time, the analogous curves $\log T_c(n)$ for the PM+VB states cut off sharply as $T_c \to 0$ even with very light doping. This is due to the fact that the density of single-electron states of the effective linearized problem for PM+VB states is high only in a very narrow region near the van Hove singularities at $k=(0,\pm\pi)$ and $(\pm\pi,0)$. Conversely, for AF+VB states the spin-alternation-induced splitting of the initial band into two subbands results in a substantial expansion of the region with a high density of states near $(0,\pi)$ and, in consequence, expansion of the region of high T_c and a large SC gap.

We note that the SC gap ratio $\xi = 2\Delta(0)/kT_c$ in the solutions obtained varies in range $s = 3.9$–4.5 for $U/t = 8$ instead of the BCS value of 3.5 with s symmetry of the order parameter. The values found for the ratio ξ are less than the values ξ

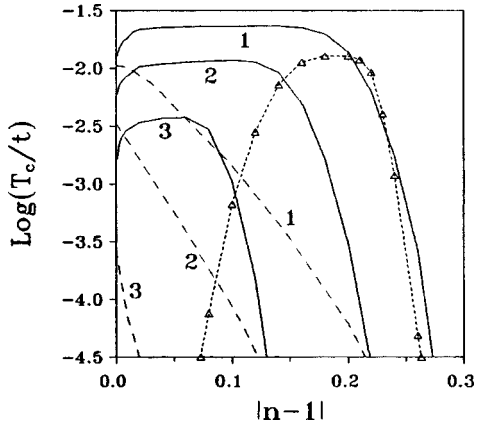

FIG. 2. Logarithm of the critical temperature T_c versus the degree of doping. The solid or dashed curves refer to AF or paramagnetic VB states. The curves *1*, *2*, and *3* are for $U/t=8$, 6, and 4, respectively. The dotted curve refers to the Hubbard model, supplemented by the interactions $V=0.1t$ and $t'=0.05$ (see text).

$=2\Delta(0)/kT_c\sim 10-12$ obtained in approximations of the type used in self-consistent spectral-function methods.[18] The experimentally observed ratio ξ is strongly anisotropic and depends on k_z, and the value pertaining to the *ab* plane of the cuprates varies in the range $\xi\sim 5-7$. For $U/t=8$ the maximum critical temperature equals $kT_c=0.023t$. The corresponding gap width equals $2\Delta(0)=0.107t$, which for the estimate[13] $t\sim 0.5$ eV equals $2\Delta(0)=53$ meV with $kT_c=133$ K.

An unexpected result of the calculation is the high values of T_c and the anisotropic gap width in a wide range of doping all the way down to very light levels. This contradicts the dependence $T_c(\delta)$ observed in cuprates with a maximum at the optimal doping level $\delta_{\rm opt}$ and a sharp dropoff of T_c on both sides of $\delta_{\rm opt}$.

In searching for the reasons for the differences in the behavior of the system we included an additional Coulomb-like interaction V between the nearest neighbors of the cells and a hopping interaction t' between the neighboring diagonal sites $\langle\langle nm\rangle\rangle$ with $|n-m|=\sqrt{2}$. The introduction of V changes somewhat the form of the curve $T_c(\delta)$ but it leads to a sharp drop in the value of T_c itself. It suppresses superconductivity as a result of an additional positive contribution to the superconducting order constant k_{11}. Conversely, the introduction of an interaction t' has virtually no effect on the maximum transition temperature with optimal doping but sharply changes the form of the curve $T_c(\delta)$. One can see from Fig. 2 that the changes in the curve $T_c(\delta)$ are very sensitive to both the magnitude and sign of t'. This can be explained as follows. For $t'>0$ and optimal doping the intersection of the lower Hubbard band E_k with the Fermi level occurs in the flattest section of the band: $E_k(\pi,0)-\mu=0$ for $\delta=\delta_{\rm opt}$. For $t'=0$ such an intersection does not occur. The fine details of the shape of the lower and upper Hubbard bands also affect other properties of the system, for example, spectroscopic, but their discussion falls outside the scope of the present letter.

In summary, we have shown for the example of a Hubbard model that the formation of valence bonds under the conditions of a high density of states of antiferromagnetically split bands indeed results in *d*-symmetry superconductivity.

This work was made possible by Russian Fund for Fundamental Research Grants 7-03-33727A and 96-15-97492. We thank V. Ya. Krivnov for helpful discussions.

[1] Z.-X. Shen and D. S. Dessau, Phys. Rep. **253**, 1 (1995).
[2] R. O. Zaĭtsev, JETP Lett. **55**, 135 (1992); **56**, 339 (1992).
[3] E. Dagotto, Rev. Mod. Phys. **66**, 763 (1994).
[4] D. J. Scalapino, Phys. Rep. **250**, 329 (1995).
[5] Yu. A. Izyumov, Usp. Fiz. Nauk **167**, 465 (1997).
[6] J. E. Hirsch, Phys. Rev. Lett. **54**, 1317 (1985).
[7] P. W. Anderson, Science **235**, 1196 (1987).
[8] I. I. Ukrainskii, Int. J. Quantum Chem. **52**, 413 (1994).
[9] A. A. Ovchinnikov and M. Ya. Ovchinnikova, Zh. Éksp. Teor. Fiz. **110**, 342 (1996) [JETP **83**, 184 (1996)].
[10] A. A. Ovchinnikov and M. Ya. Ovchinnikova, Zh. Éksp. Teor. Fiz. **112**, 1409 (1997) [JETP **85**, 767 (1997)].
[11] M. C. Gutzwiller, Phys. Rev. A **137**, 1726 (1965).
[12] A. A. Ovchinnikov and M. Ya. Ovchinnikova, Zh. Éksp. Teor. Fiz. [JETP], in press.
[13] J. H. Jefferson, H. Eskes and L. F. Feiner, Phys. Rev. B **45**, 7959 (1992).
[14] U. Trapper, D. Ihle, and H. Fenke, Phys. Rev. B **52**, R11553 (1995).
[15] N. Nasgaosa, Science **275**, 1078 (1997).
[16] S. C. Zhang, Science **275**, 1089 (1997).
[17] P. Montoux and D. Pines, Phys. Rev. B **50**, 16015 (1994).
[18] N. E. Brickers and S. R. White, Phys. Rev. B **43**, 8044 (1991).

Translated by M. E. Alferieff

Phase diagrams of $(d_{x^2-y^2}+id_{xy})$ superconductors on a square lattice

E. A. Shapoval[a)]

All-Russia Scientific-Research Institute of the Metrological Service, 117334 Moscow, Russia

(Submitted 24 December 1997; resubmitted 28 January 1998)
Pis'ma Zh. Éksp. Teor. Fiz. **67**, No. 5, 356–360 (10 March 1998)

A model of strongly coupled electrons on a square lattice with attraction of the electrons to nearest-neighbor and next-nearest neighbor lattice sites is studied. For this model, the phase diagrams containing $d_{x^2-y^2}$, d_{xy}, and $(d_{x^2-y^2}+id_{xy})$ states are constructed in the variables temperature versus chemical potential for different ratios of the corresponding potentials. © *1998 American Institute of Physics.* [S0021-3640(98)01405-4]

PACS numbers: 74.25.Dw

The question of the symmetry of the order parameter remains a central problem of high-T_c superconductivity. Special attention is given to a second phase transition, accompanied by breaking of the time-reversal symmetry and the appearance of an energy gap in the elementary excitation spectrum of d superconductors. This transition, which is due to grain boundaries, twinning boundaries, or magnetic impurities, has been studied in a number of works; see, for example, Refs. 1–4 and the references cited therein. A different approach — investigation of the possibility of such a transition in the volume of a pure superconductor — is studied in Refs. 5–9. Specifically, Ref. 9 examines a phase transition from an s to an $(s+id)$ state in a model with a cylindrical Fermi surface. The present letter examines a somewhat more complicated model of strongly coupled electrons on a square lattice with the dispersion relation

$$\xi(\mathbf{q})=-\frac{1}{2}(\cos q_x+\cos q_y), \tag{1}$$

expressing the electron energy as a function of the quasimomentum. The possibility of electrons hopping only to a neighboring lattice site is taken into account, energy is measured from the band center (where there is a van Hove singularity), and energy and length are measured in units of the half width of the band and the lattice constant, respectively.

We shall assume that only electrons occupying the same or nearest-neighbor and next-nearest neighbor lattice sites with the corresponding potentials $-u_0$, $-u_1$, and $-u_2$ interact with one another. Then the BCS potential has the form

$$U(\mathbf{q},\mathbf{q}')=u_0+2u_1[\cos(q_x-q_x')+\cos(q_y-q_y')]+2u_2[\cos(q_x+q_y-q_x'-q_y')$$

$$+\cos(q_x-q_y-q_x'+q_y')]. \tag{2}$$

Next, we assume that the Coulomb repulsion of the electrons occupying the same site is so large that the superconducting s state is not realized, at least at reasonable temperatures. Then, the part of the BCS potential that is responsible for singlet pairing in the $d_{x^2-y^2}$ and d_{xy} states equals

$$U(\mathbf{q},\mathbf{q}')=u_1\psi_{x^2-y^2}(\mathbf{q})\psi_{x^2-y^2}(\mathbf{q}')+u_2\psi_{xy}(\mathbf{q})\psi_{xy}(\mathbf{q}'), \tag{3}$$

where

$$\psi_{x^2-y^2}(\mathbf{q})=\cos\ q_x-\cos\ q_y, \quad \psi_{xy}(\mathbf{q})=4\ \sin\ q_x\ \sin\ q_y. \tag{4}$$

It is convenient to introduce a parametric description of the state of the electrons in terms of their energy ξ and the position of an isoenergy surface (specifically, the Fermi surface) θ:

$$\cos\ q_x=-\xi+(1-|\xi|)\cos\ \theta; \quad \cos\ q_y=-\xi-(1-|\xi|)\cos\ \theta. \tag{5}$$

If $\xi\leqslant 0$, then the parameter θ is identical to the doubled azimuthal angle ϕ of the wave vector $\mathbf{q}$ where $\phi=0,\ \pm\pi/4,\pm\pi/2,\ \ldots$.

In the new variables the integration over the electronic states of the Brillouin zone has the form

$$\int_{-\pi}^{\pi}\int_{-\pi}^{\pi}\frac{dq_x dq_y}{(2\pi)^2}f(q_x,q_y)=\int_{-1}^{1}d\xi\nu(\xi)\langle f(\xi,\theta)\rangle, \tag{6}$$

where the brackets signify averaging over the isoenergy surface

$$\langle f(\xi,\theta)\rangle=\frac{1}{\pi K(k)}\int_0^{\pi}\frac{f(\xi,\theta)d\theta}{\sqrt{1-k^2\cos^2\theta}}, \tag{7}$$

$K(k)$ is the complete elliptic integral of the first find, $k=(1-|\xi|)/(1+|\xi|)$, and the density of states

$$\nu(\xi)=\frac{4}{\pi^2(1+|\xi|)}K(k)=\frac{2}{\pi^2}K'(\xi). \tag{8}$$

In the new variables

$$\psi_{x^2-y^2}(\xi,\theta)=-2(1-|\xi|)\cos\ \theta; \quad \psi_{xy}(\xi,\theta)=2(1-\xi^2)\sin\ \theta\sqrt{1-k^2\cos^2\theta}. \tag{9}$$

Since by virtue of expression (3) the kernel of the integral equation determining the superconducting state is degenerate, the order parameter can be expanded in terms of the functions $\psi_{x^2-y^2}(\xi,\theta)$ and $\psi_{xy}(\xi,\theta)$. Since these functions are orthogonal to one another, we write immediately

$$\Delta(\xi,\theta)=\Delta_{x^2-y^2}\psi_{x^2-y^2}(\xi,\theta)\pm i\Delta_{xy}\psi_{xy}(\xi,\theta), \tag{10}$$

where $\Delta_{x^2-y^2}$ and Δ_{xy} are real. The assertion that in the mixed state the relative phase of the two components of the order parameter which are described by orthogonal functions equals $\pm\pi/2$ was proved in Ref. 10. It can be shown that in the case when three or more

states compete the system chooses from among them the pair of orthogonal states with relative phase $\pm\pi/2$ that is most favorable from the standpoint of the free energy.

Mixed states such that both components of the order parameter are different from zero are described by the system of equations

$$\frac{u_1}{2}\int_{-1}^{1}\nu(\xi)\left\langle\frac{\psi^2_{x^2-y^2}}{\epsilon(\xi,\mu,\theta)}\tanh\frac{\epsilon(\xi,\mu,\theta)}{2T}\right\rangle d\xi=1,$$

$$\frac{u_2}{2}\int_{-1}^{1}\nu(\xi)\left\langle\frac{\psi^2_{xy}}{\epsilon(\xi,\mu,\theta)}\tanh\frac{\epsilon(\xi,\mu,\theta)}{2T}\right\rangle d\xi=1, \tag{11}$$

where the energy of elementary excitations is

$$\epsilon(\xi,\mu,\theta)=\sqrt{(\xi-\mu)^2+\Delta^2_{x^2-y^2}\psi^2_{x^2-y^2}(\xi,\theta)+\Delta^2_{xy}\psi^2_{xy}(\xi,\theta)}. \tag{12}$$

Following Refs. 5 and 11, we do not introduce a cutoff parameter for the electron interaction energy (the analog of the Debye energy in the theory of ordinary superconductors), as is conventionally done in the BCS method. Here the logarithmic divergence is eliminated by the finite width of the conduction band. The results obtained below will change very little as a result of introducing this additional parameter, if the temperature and energy gap are measured not in units of the half width of the band but rather the cutoff parameter.

Pure $d_{x^2-y^2}$ and d_{xy} superconducting states, where only one component of the order parameter is different from zero, are determined by the first or second equation of the system (11), respectively. The boundaries of the mixed and pure phases are determined from this system when one of the components vanishes.

It turns out that this model behaves differently depending on the ratio of the attractive potentials u_1 and u_2. Figure 1 shows three of the corresponding regions (*A, B,* and *C*) of values of the potential (in units of the half width of the conduction band). The dots represent the specific values of these potentials used to construct the phase diagrams shown in Fig. 2.

Figure 2a shows a typical phase diagram of our model in the variables temperature T and chemical potential μ in the region *A* in the particular case when $u_1=0.18$ and $u_2=0.2$. This value of u_1 is generally accepted for, specifically, the compound $LaSrCuO_4$ on the basis of data on its superconducting transition temperature and width of the conduction.[5,8] Considering the rapid dropoff of the screened Coulomb repulsion and assuming a comparatively slow dropoff of the interaction responsible for the Cooper pairing, we conjecture that in some compounds u_2 can be greater than u_1. Figure 2 shows only half of the diagrams because the complete diagrams are symmetric with respect to $\mu=0$ by virtue of the symmetry of the problem relative to a change in the sign of the energy. The region *1* in these diagrams corresponds to the $d_{x^2-y^2}$ phase, the region *2* to the d_{xy} phase, the region *3* to the mixed ($d_{x^2-y^2}\pm id_{xy}$) phase, and the region *4* to the normal phase; the curves $T_{x^2-y^2}$ and T_{xy} are the temperatures of the transitions from the normal to the corresponding superconducting state and the dashed curves show their continuations in the absence of another interaction. As u_2 increases or u_1 decreases, the point of intersection of the curves shifts to the right and up, i.e., the corresponding chemical potential approaches zero, while the temperature at which the mixed state

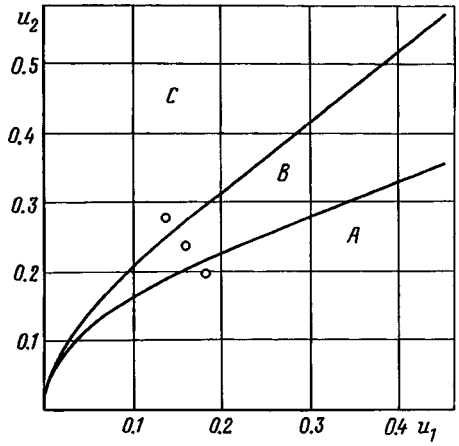

FIG. 1. Regions of the interaction potential with different behavior of the model studied.

$(d_{x^2-y^2} \pm i d_{xy})$ can appear increases. The opposite picture is observed when u_2 decreases or u_1 increases. The main feature of the region A in Fig. 1 is the absence of a phase transition to the mixed state for a half-filled band, when $\mu = 0$ while the temperature of the superconducting state has its maximum value.

The phase diagram of the model in the region B of values of the interaction potentials is illustrated in Fig. 2b for $u_1 = 0.16$ and $u_2 = 0.24$. The designations are the same as in Fig. 2a. The characteristic feature of this region is a phase transition to the mixed state $(d_{x^2-y^2} \pm i d_{xy})$ with chemical potential $\mu = 0$, i.e., with the maximum superconducting transition temperature for the model.

A typical phase diagram for the region C with $u_1 = 0.14$ and $u_2 = 0.28$ is shown in Fig. 2c. In this case, for $\mu = 0$, as the temperature decreases, the model makes a transition from the normal to the d_{xy} state before the obligatory for any positive u_1 transition to the mixed state.

It follows from this that the boundary of the regions A and B in Fig. 1 is determined by the equation $T^*(u_1, u_2) = 0$ with $\mu = 0$, where T^* is the temperature of the transition to the mixed state and the boundary of the regions B and C is determined by the equation $T_{x^2-y^2}(u_1) = T_{xy}(u_2)$.

Figure 3 shows the relative components of the order parameter $\Delta_{x^2-y^2}/\Delta_0$ and Δ_{xy}/Δ_0 versus the relative temperature T/T_c for $u_1 = 0.16$ and $u_2 = 0.24$ (i.e., in the region B) and chemical potential $\mu = 0$ (i.e., a half-filled band). Here $T_c = T_{x^2-y^2} = 0.0151$, while $\Delta_0 = 0.0158$ is the order parameter in the pure $d_{x^2-y^2}$ state with fixed u_1 and $T = 0$. The temperature of the transition to the mixed state is $T^* = 0.00729 = 0.484 T_c$. The dashed curve is the continuation of the temperature dependence of the relative order parameter in the absence of a transition to the mixed state. The dashed curve shows the temperature dependence of $\Delta_{x^2-y^2}$ in a pure $d_{x^2-y^2}$ state. The components of the order parameter behave similarly for other values of the chemical potential, and the corresponding temperatures of the superconducting transition and the transition to the mixed state can be determined from the phase diagrams in Fig. 2.

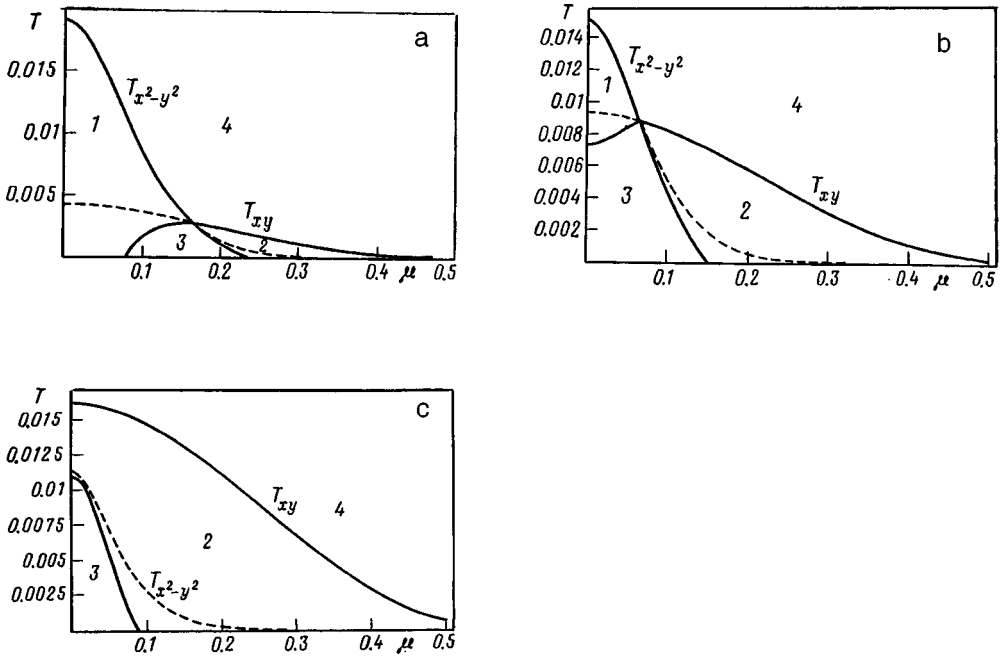

FIG. 2. Phase diagrams: a — in region A with $u_1=0.18$, $u_2=0.2$; b — in region B with $u_1=0.16$, $u_2=0.14$; c — in region C with $u_1=0.14$, $u_2=0.28$. Region *1* — $d_{x^2-y^2}$ phase, *2* — d_{xy} phase, *3* — mixed phase $d_{x^2-y^2}\pm id_{xy}$, *4* — normal state.

We call attention to the fact that in contrast to the transition from the d to the $(d\pm is)$ state which was studied in Ref. 9, in our case the $d_{x^2-y^2}$ component of the order parameter deviates slightly from its value in the absence of a transition to a mixed state. Nonetheless, such a transition is accompanied even here by rapid growth (as $\sqrt{T^*-T}$) of the gap in the elementary excitation spectrum. For this reason, to identify a transition it is necessary to investigate the angular dependence of the energy gap. It seems to us that because of the strong Coulomb repulsion the transition to the $(d_{x^2-y^2}\pm id_{xy})$ state is

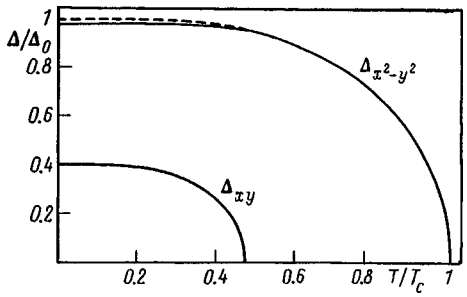

FIG. 3. Temperature dependence of the order parameter components for $u_1=0.18$, $u_2=0.2$, and $\mu=0$. The dashed curve shows the temperature dependence of $\Delta_{x^2-y^2}$ in a pure $d_{x^2-y^2}$ state.

more likely than a transition to the $(d \pm is)$ state. Specifically, it is entirely likely that the well-known result obtained by Ma *et al.*[12] — the jumplike change in the symmetry at $T^* \approx 0.8T_c$ — could pertain to the transition examined here.

This work is supported by the Scientific Council on the Topic ''Superconductivity'' of the State Science and Technology Program ''Topical Problems in Condensed Matter Physics'' and was performed at the P. N. Lebedev Center for Physical Studies as part of Project 96024.

[a)]e-mail: shap@mics.msu.su and/or shapoval@kapitza.ras.ru

[1] M. Sigrist, K. Kuboko, P. A. Lee *et al.*, Phys. Rev. B **53**, 2835 (1996).
[2] G. E. Volovik, JETP Lett. **66**, 522 (1997).
[3] R. B. Laughlin, preprint, http://xxx.lanl.gov/abs/cond-mat/9709004.
[4] A. V. Balatsky, preprint, http://xxx.lanl.gov/abs/cond-mat/9709287.
[5] C. O'Donovan and J. P. Cabotte, Phys. Rev. B **52**, 16208 (1995); Physica C **252**, 87 (1995).
[6] K. A. Musaelian, J. Betouras, A. V. Chubikov, and R. Joynt, Phys. Rev. B **53**, 3598 (1996).
[7] Yong Ren, Ji-Hai Xu, and C. S. Ting, Phys. Rev. B **53**, 2249 (1996).
[8] D. M. News, C. C. Tsuei, and P. C. Pattnaik, Phys. Rev. B **52**, 13611 (1995).
[9] E. A. Shapoval, JETP Lett. **64**, 625 (1996); Physica C **282-287**, 1655 (1997).
[10] E. V. Gorbarm V. M. Loktev, and V. S. Nikolaev, Sverkhprovodimost' (KIAE) **7**, 1 (1994).
[11] R. Micnas, J. Ranninger, and S. Robaszkiewicz, Rev. Mod. Phys. **62**, 113 (1990).
[12] J. Ma, C. Quitmann, R. J. Kelley *et al.*, Science **267**, 862 (1995).

Translated by M. E. Alferieff